GL-TR-89-0161

AD-A216 135

Seismic Pulse Broadening Associated With Fracture Damage Caused by Explosions in Crystalline Rock

Charles G. Sammis

University of Southern California
Department of Geological Sciences
Los Angeles, CA 90089

1989 August 30

Final Report
January 1986 - January 1989

DTIC
ELECTE
DEC 07 1989
S D
E

Approved for public release; distribution unlimited

GEOPHYSICS LABORATORY
AIR FORCE SYSTEMS COMMAND
UNITED STATES AIR FORCE
HANSCOM AIR FORCE, BASE, MASSACHUSETTS 01731-5000

Unclassified
SECURITY CLASSIFICATION OF THIS PAGE

REPORT DOCUMENTATION PAGE

Form Approved OMB No. 0704-0188

1a. REPORT SECURITY CLASSIFICATION: Unclassified	1b. RESTRICTIVE MARKINGS
2a. SECURITY CLASSIFICATION AUTHORITY	3. DISTRIBUTION/AVAILABILITY OF REPORT: Approved for public release; distribution unlimited.
2b. DECLASSIFICATION/DOWNGRADING SCHEDULE	
4. PERFORMING ORGANIZATION REPORT NUMBER(S)	5. MONITORING ORGANIZATION REPORT NUMBER(S): [illegible]-TR-89-0161
6a. NAME OF PERFORMING ORGANIZATION: University of Southern Calif. / 6b. OFFICE SYMBOL (If applicable)	7a. NAME OF MONITORING ORGANIZATION: Geophysics Laboratory
6c. ADDRESS (City, State, and ZIP Code): Department of Geological Sciences, Los Angeles, CA 90089-0740	7b. ADDRESS (City, State, and ZIP Code): Hanscom AFB, Massachusetts 01731-5000
8a. NAME OF FUNDING/SPONSORING ORGANIZATION: DARPA / 8b. OFFICE SYMBOL (If applicable): NMRO	9. PROCUREMENT INSTRUMENT IDENTIFICATION NUMBER: F19628-86-K-0003
8c. ADDRESS (City, State, and ZIP Code): 1400 Wilson Blvd., Arlington, VA 22209-2308	10. SOURCE OF FUNDING NUMBERS: PROGRAM ELEMENT NO. 61101E; PROJECT NO. 6A10; TASK NO DA; WORK UNIT ACCESSION NO. BD

11. TITLE (Include Security Classification): Seismic Pulse Broadening Associated With Fracture Damage Caused by Explosions in Crystallir Rock

12. PERSONAL AUTHOR(S): Charles G. Sammis

13a. TYPE OF REPORT	13b. TIME COVERED	14. DATE OF REPORT (Year, Month, Day)	15. PAGE COUNT
FINAL REPORT	FROM 1/86 TO 1/89	1989 August 30	98

16. SUPPLEMENTARY NOTATION

17. COSATI CODES			18. SUBJECT TERMS (Continue on reverse if necessary and identify by block number)
FIELD	GROUP	SUB-GROUP	damage mechanics, strain, pulse-broadening

19. ABSTRACT (Continue on reverse if necessary and identify by block number)

Recent analyses of the initiation, propagation, and linkage of fractures from pre-existing cracks have been used to formulate a damage mechanics for brittle solids loaded in compression. The model describes the accumulation of damage with strain. It has been used to construct damage initiation surfaces and failure surfaces which have been tested using previously published experimental data. It is shown that a damage mechanics rheology can produce seismic pulse-broadening observed in underground tests in granitic rock. It is proposed that the basic scaling relation between the size of the pre-existing cracks and the stress required to initiate damage may explain why models based on laboratory data and large scale laboratory simulations have failed to reproduce the pulse-broadening observed in the field.

20. DISTRIBUTION/AVAILABILITY OF ABSTRACT	21. ABSTRACT SECURITY CLASSIFICATION
☐ UNCLASSIFIED/UNLIMITED ☐ SAME AS RPT. ☐ DTIC USERS	Unclassified
22a. NAME OF RESPONSIBLE INDIVIDUAL: James Lewkowicz	22b. TELEPHONE (Include Area Code): (617) 377-3222 / 22c. OFFICE SYMBOL: GL/LWH

DD Form 1473, JUN 86 — Previous editions are obsolete. — SECURITY CLASSIFICATION OF THIS PAGE

Unclassified

SEISMIC PULSE BROADENING ASSOCIATED WITH FRACTURE DAMAGE CAUSED BY EXPLOSIONS IN CRYSTALLINE ROCK

Charles G. Sammis
Department of Geological Sciences
University of Southern California
Los Angeles, CA. 90089-0740

Accession For
NTIS GRA&I
DTIC TAB
Unannounced
Justification
By
Distribution/
Availability Codes
Dist | Avail and/or Special
A-1

INTRODUCTION

For the three U.S. underground tests in granite, the particle velocity was measured in the free field as a function of the distance from the shot point. In each case, numerical simulations using continuum mechanics with strength values measured in the laboratory have failed to predict the velocity pulse width to within a factor of about 5 (Rimer et al., 1987). Models which predict the observed pulse-width all require a large reduction in the post-shock strength to values well below those measured in the laboratory - even for heavily pre-fractured samples.

The physical mechanism responsible for the post-shock weakening has not been clear. Cherry and Rimer(1982) invoked an "effective stress" mechanism in which the free crack and pore space is eliminated during the initial compression. Fluids in the remaining saturated cracks are compressed to high pressures and support part of the confining stress, thereby reducing the failure stress behind the shock-front. However, Scholz (1982) has argued that dilatancy hardening is expected to override any weakening produced by the

effective stress effect.

Russian scientists (Zamyshlyayev et al., 1980) have also shown that post-shock weakening can produce the pulse-broadening observed in the Hard Hat explosion, but their proposed mechanism is quite different. They attribute weakening to the time dependent growth of cracks behind the shock front. They also assert that shear deformation behind the shock front produces a rotation of the blocks of rock between fractures and results in dilatancy. Based on their modeling, they conclude that post-shock weakening and dilatancy contribute equally to the observed pulse shape. The proposed weakening is shown in Figure 1 (from their paper).

Our explanation of weakening is, in principal, the same as that proposed by Zamyshlyayev et al. (1980), except that our model is based on the micromechanics of crack growth under compressive loading. As illustrated in Figure 2, we model the activation of preexisting cracks and joints (of length a) by the explosive pressure pulse. By formulating the rheology in terms of the basic physics of crack nucleation, growth, and interaction, the effects of variables such as porosity, water saturation, and the density and orientation of preexisting cracks and joints can be included in the model. This type of formulation is known as a "damage mechanics". The state of crack growth at any time is represented as a damage vector. As stress increases, damage accumulates, the elastic stiffness decreases, and the stress-strain relation becomes non-linear. At large values of the damage, the growing fractures interact, and damage accumulation is accelerated. A peak stress is achieved after which the strength decreases with additional strain.

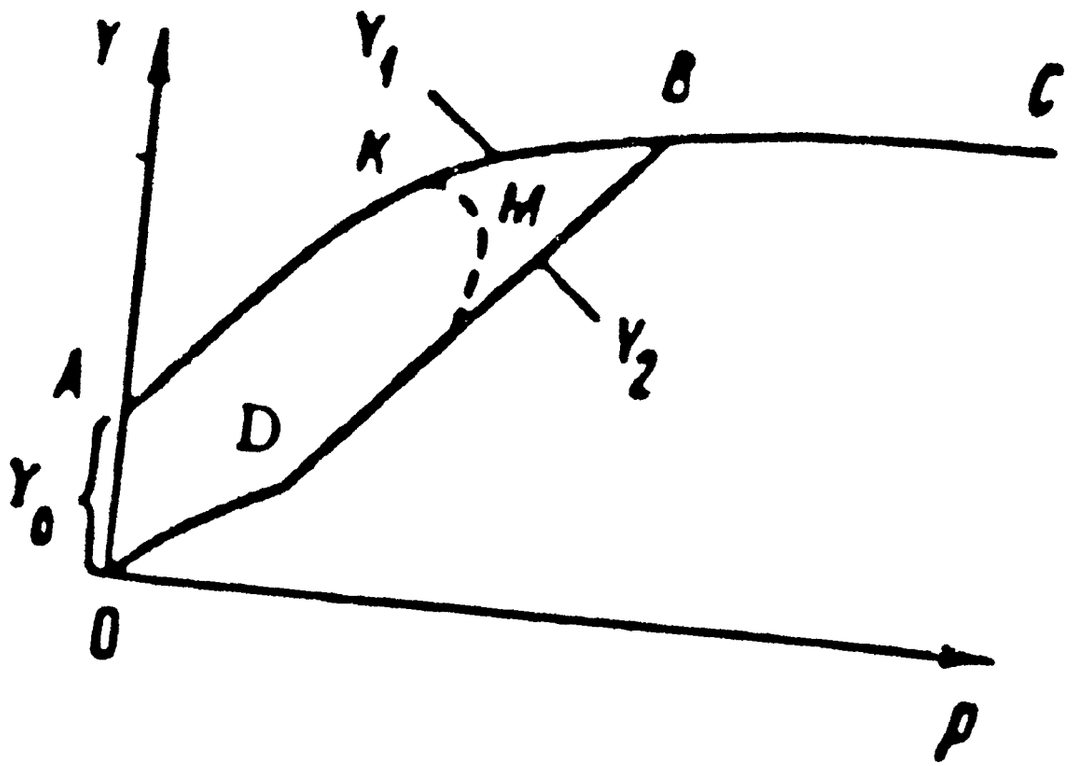

Figure 1. Post-shock weakening path from Zamyshlyayev et el. (1980). Y_1 is the strength of the undamaged rock and Y_2 is the strength of the damaged rock. The dashed path represents the strength reduction which accompanies crack growth.

In the following we review our damage mechanics model (Ashby and Sammis, 1989; appended) and show that it gives a good description of the failure surfaces of a wide variety of rocks with a very small number of adjustable parameters. We then use the damage mechanics to interpret a series of laboratory simulations in granite. Finally, we use a simple one-dimensional calculation to show how a damage mechanics rheology can produce significant pulse broadening.

DAMAGE MECHANICS

We now briefly review our damage mechanics formulation by outlining the key results. The details are given in the appended paper (Ashby and Sammis, 1989) which is in press in PAGEOPH.

Crack Initiation

Most brittle solids contain inhomogeneities: small holes or cracks, particles which are poorly bonded, or phases which have different moduli or strengths from those of the matrix. Any one of these can act as nuclei for new cracks when the solid is loaded.

The range of possible nuclei is wide, but the spectrum of their characteristics is probably bracketed by two extremes: the spherical hole and the sharp inclined crack. Both have been studied experimentally and both have been modeled, the first by Sammis and Ashby (1986) and the second by Nemat-Nasser and Horii (1982) and Ashby and Hallam (1986). In both cases, the criterion for crack initiation, under axisymmetric loading has the form

$$\sigma_1 = c_1 \sigma_3 - \sigma_0 \qquad (1)$$

where c_1 and σ_0 are material properties, σ_1 is the axial stress, and $\sigma_2=\sigma_3$ the radial stress (both positive when tensile, negative when compressive).

In this paper we consider the growth of crack-damage from initial, inclined cracks as in Figure 2. For this case (Nemat-Nasser and Horii, 1982; Ashby and Hallam, 1986) cracks initiate when

$$\sigma_1 = \frac{\left(1+\mu^2\right)^{1/2} + \mu}{\left(1+\mu^2\right)^{1/2} - \mu}\,\sigma_3 - \frac{\sqrt{3}}{\left(1+\mu^2\right)^{1/2} - \mu}\,\frac{K_{Ic}}{\sqrt{\pi a}} \qquad (2)$$

where μ is the coefficient of friction acting across the crack faces, K_{Ic} is the fracture toughness of the material through which the new crack propagates, and 2a is the length of the original inclined crack. Rocks, typically, show a coefficient of friction of about 0.6, in which case $C_1 = 3.1$ and $\sigma_0 = 3.1\, K_{Ic}/\sqrt{\pi a}$. Crack initiation from holes (Sammis and Ashby, 1986) gives similar values.

Equation (2) was shown by Ashby and Sammis (1989) to give an adequate description of triaxial data for a wide range of rock-types. It is used to describe the initiation of damage in the diagrams shown later. In each case, experimental data are fitted to eqn. (2) to give μ and a (using published data for K_{Ic}). Results of this analysis are summarized in Table 1. In the computations, it is convenient to normalize the equations by the quantity $K_{Ic}/\sqrt{\pi a}$, giving

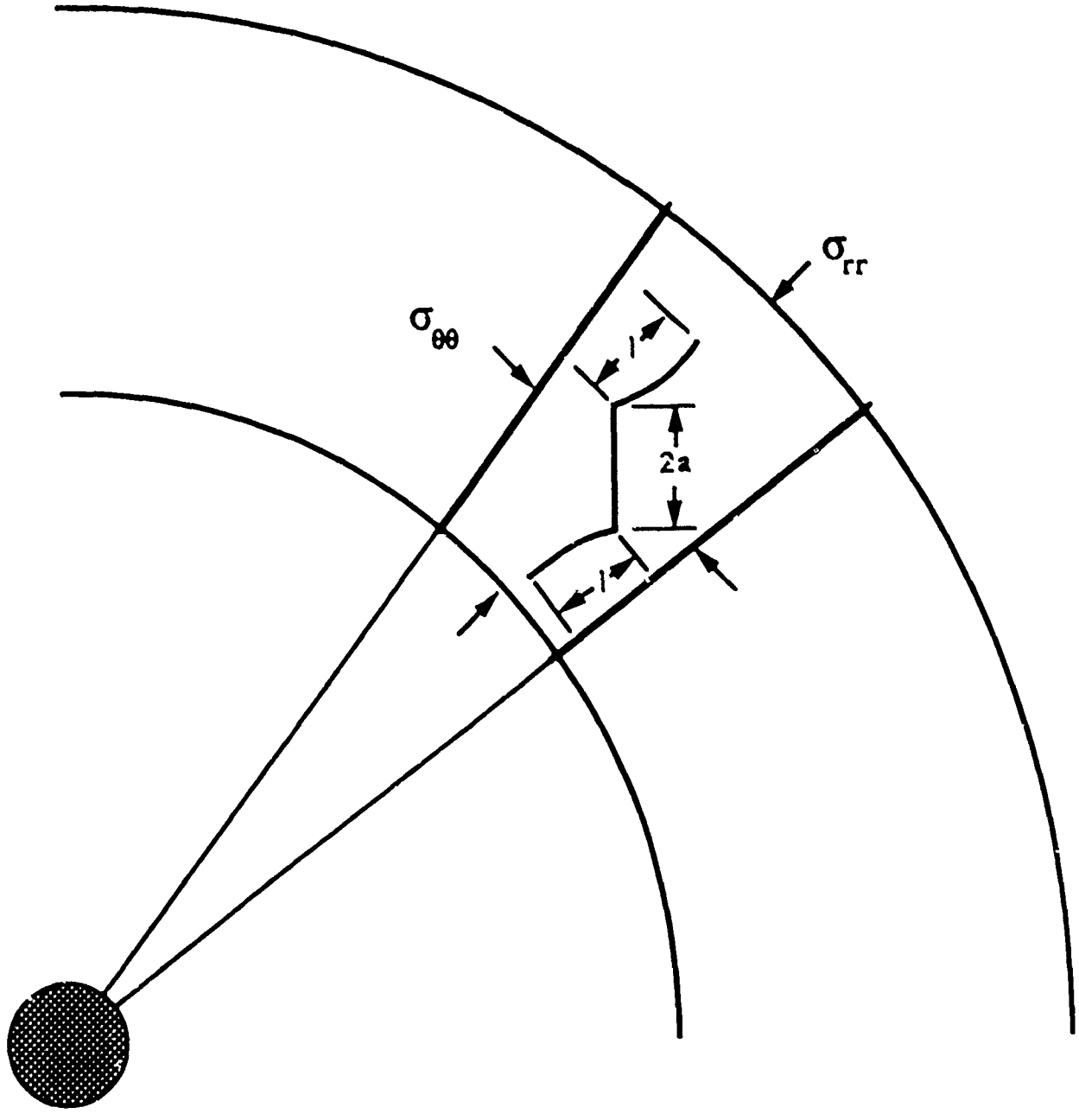

Figure 2. The out-of-plane extension of a pre-existing fracture in an explosion-generated stress field. The wing-cracks have grown to a length l.

$$S_1 = c_1 S_3 - S_0 \tag{3}$$

with

$$S_1 = \sigma_1 \sqrt{\pi a} / K_{Ic}$$
$$S_3 = \sigma_3 \sqrt{\pi a} / K_{Ic} \tag{4}$$
$$c_1 = \frac{\left(1+\mu^2\right)^{1/2} + \mu}{\left(1+\mu^2\right)^{1/2} - \mu}$$

$$S_0 = \frac{\sqrt{3}}{\left(1+\mu^2\right)^{1/2} - \mu}$$

Crack Growth and Interaction

Once initiated, the wing cracks (as we shall call the crack-like extensions of the original flaw) grow longer. During growth, the stress intensity K_I at the tip of each wing crack is equal to, or exceeds, the fracture toughness K_{Ic} of the solid. The condition for crack advance is simply

$$K_I \geq K_{Ic}$$

The difference between tension and compression is that growth in compression is stable: each increment of crack advance requires an increment of load, at least until the cracks start to interact strongly.

For the 3-D case in which the flaws and wing cracks are entirely contained within the material, Ashby and Sammis (1989) calculated K_I at the tip of the wing cracks to arrive at the following expression which relates the length of the wing cracks to the applied stresses

TABLE 1. MATERIAL PROPERTIES OF THE ROCKS AND FITTED MODEL PARAMETERS (Bracketted data are estimates).

MATERIAL(*)	K (GPa) (j)	E (GPa) (j)	Sy (MPa) (k)	Kic (MPam) (l)	2a (mm) (n)	Mu (n)	Do (n)	C3 (n)
ECLOGITE (a)	94	130	4000	(1.0)	0.6	0.6	0.08	2.0
DUNITE (b)	130	150	3500	(1.0)	1.0	0.6	0.04	2.0
APLITE (c)	58	-	2300	(1.0)	0.2	0.60	0.08	2.0
GABBRO (d)	60	92	2200	(1.0)	0.8	0.55	0.12	2.0
GRANITE (e)	58	70	2200	1.0	1.0	0.64	0.01	2.0
SANDSTONE (f)	130	130	1000	0.7	2.0	0.60	0.15	2.0
LIMESTONE (g)	70	77	700	0.6	0.05	0.55	0.15	2.0
MARBLE (h)	70	70	350	0.64	0.35	0.6	0.12	2.0
ROCKSALT (i)	37	37	65	0.23	0.5	0.55	0.20	2.0

(a) Eclogite; Shimada et al (1983).
(b) Dunite; Shimada et al (1983).
(c) Aplite; Brace et al (1966).
(d) Gabbro; Shimada et al (1983).
(e) Westerly Granite; Brace et al (1966), Mogi (1966) and Holcomb and Costin (1986).
(f) Medium-grained Buntsandstone; Gowd and Rummel (1980).
(g) Solenhofen Limestone; Heard (1960).
(h) Carrara Marble; Von Karman (1911) and Edmond and Paterson (1972).
(i) Rocksalt; Handin (1953) and Hunsche (1981).
(j) Bulk modulus K and Young's modulus E from Birch (1966).
(k) Derived from data plotted in figures 11 to 24.
(l) Atkinson and Meredith (1987). The lowest published value was chosen in each case.
(n) Obtained by fitting the data of Figs 11 to 24 to the equations of the text.
(*) We assume α = 0.7 and β = 0.45 for all materials.

$$S_1 = -\left(\frac{C_2\left(\left(\frac{D}{D_0}\right)^{1/3} - 1 + \frac{\beta}{\alpha}\right)^{3/2} - S_3\left[C_1\left(1 + \left(\frac{C_3 D_0^{2/3}}{1 - D^{2/3}}\right)\left(\left(\frac{D}{D_0}\right)^{1/3} - 1\right)^2\right) + C_4\left(\left(\frac{D}{D_0}\right)^{1/3} - 1\right)^2\right]}{1 + C_3 \frac{D_0^{2/3}}{(1 - D^{2/3})}\left(\left(\frac{D}{D_0}\right)^{1/3} - 1\right)^2} \right) \tag{5}$$

where S_1 and S_3 are defined by equation (4). The values of the constants are:

$$C_1 = \frac{\left(1 + \mu^2\right)^{1/2} + \mu}{\left(1 + \mu^2\right)^{1/2} - \mu} \tag{6}$$

$$C_2 = \pi \alpha \sqrt{\frac{3\alpha}{\beta}} \left(\left(1 + \mu^2\right)^{1/2} - \mu \right)^{-1}$$

$$C_3 = 2$$

$$C_4 = 2\alpha^2 \sqrt{\frac{3}{\beta}} \left(\left(1 + \mu^2\right)^{1/2} - \mu \right)^{-1}$$

$$\beta = 0.1$$

The preexisting damage, D_0, and the current damage, D, are defined

as

$$D_0 = \frac{4}{3}\pi(\alpha a)^3 N_v \qquad (7)$$

$$D = \frac{4}{3}\pi(l+\alpha a)^3 N_v$$

where l is the length of the growing wing-cracks and N_v is the number of initial cracks of length a per unit volume.

Figures 3 and 4 illustrate some features of the results. The axial stress at first rises as damage grows (Figure 3), passing through a peak which shifts to higher values of damage as the confining pressure increases. The damage surface, shown in Figure 4, is almost a cone meaning that, to a first approximation, the failure envelope is described by

$$\sigma_1 = C\sigma_3 - \sigma_C \qquad (8)$$

where C is a constant and σ_C is the unconfined compressive strength. The value of the model is that it gives a physical interpretation to C and σ_C, and relates them to the initial damage, the coefficient of friction, and the crack size.

Analysis of Data

The strength of many different rocks have been determined under triaxial loading conditions ($|\sigma 1| > |\sigma 2| = |\sigma 3|$, where all three principal stresses are compressive) . For a few, the initiation of

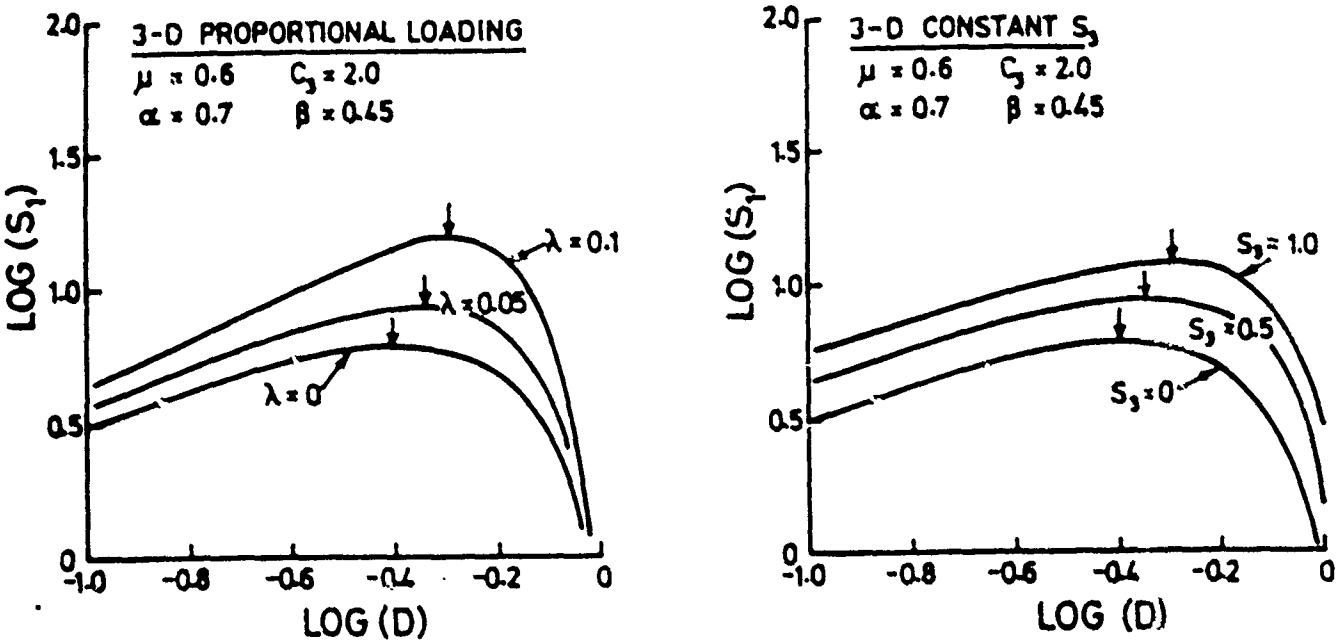

Figure 3. The dependence of axial stress on damage a predicted by equations (5) - (7). The peak stress is marked. We take this as the failure stress.

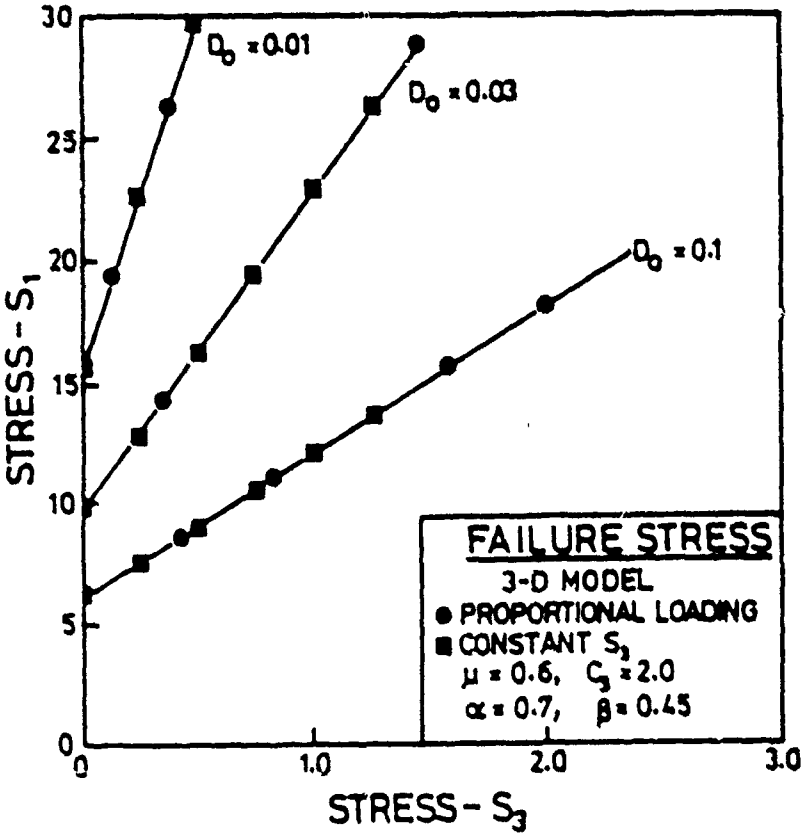

Figure 4. The peak value of axial stress plotted against the confining stress to show the failure surface. In this formulation, damage is a state variable.

microcracking has also been determined. Ashby and Sammis (1989) applied the damage mechanics model developed above to nine different rock types for which the most complete data sets exist : granite, aplite, dunite, eclogite, gabbro, sandstone, limestone, marble and rock salt. These rocks represent a wide range of composition and initial damage. Granite, aplite, dunite and eclogite are low porosity, crystalline, igneous rocks in which the initial damage is mostly in the form of low aspect cracks. Limestone and sandstone are porous sedimentary rocks in which the initial damage is mostly in the form of high aspect pores. Marble is a metamorphic rock with initial damage of a form intermediate between the previous two extremes. These rocks also span a wide range of yield strengths. The igneous rocks have yield strengths in excess of 2 GPa while the calcareous rocks (limestone and marble) yield at stresses below 1 GPa. Rock salt is at the low extreme with a yield strength below 100 MPa.

The damage mechanics model formulated above has three constants: μ , α, and β. They are not strictly adjustable because the theory makes predictions for their values. However because of approximations in the derivation, and the uncertainties in the aspect ratio of the starter flaws, we have treated β as adjustable, choosing the value 0.45 to give the best fit to the data.

For those materials where crack initiation data are available, the crack length 2a and the coefficient of friction μ are determined from the initiation surface using eqn. (2). K_{Ic} is also required. Although K_{Ic} may be estimated for most rocks (Atkinson and Meredith, 1987), the starter flaw size is not known in most cases

and must be treated as an adjustable parameter. The derivation of the fundamental equations gives $C_3 = 2$, and this gives a good description of the materials we have examined.

As an example, the triaxial data for damage initiation and failure in Westerly granite are presented on plots of σ_1 vs σ_3 in Figure 5. The theoretical fracture initiation surface (eqn. 2), surfaces of constant damage, and the failure surface (calculated from the maximum of eqn. (5) for each value of σ_3) are plotted on these graphs for comparison with the data.

As the confining pressure is increased, brittle fracture is made increasingly difficult. A critical pressure may be reached at which true plasticity replaces crack extension. This transition can be illustrated by plotting a yield (or creep) surface, defined by:

$$\sigma_y^2 = \frac{1}{2}\left[(\sigma_1 - \sigma_2)^2 + (\sigma_2 - \sigma_3)^2 + (\sigma_3 - \sigma_1)^2\right] \qquad (9)$$

The yield surface is plotted as a pair of heavy broken lines on the figure The yield strength, σ_y, can be derived from hardness, H, data since $\sigma_y = H/3$. Figure 5a shows theoretical surfaces for initiation, constant damage, and failure at low values of the confining stress. The fracture initiation data from Brace et al. (1966) were determined from the onset of non-linear behavior of the volume strain. Only data taken at the highest loading rate are plotted here in order to minimize effects of subcritical crack growth (which we do not model). The three initiation points from Holcomb and Costin (1986) were determined from the onset of acoustic emission (AE) in a previously

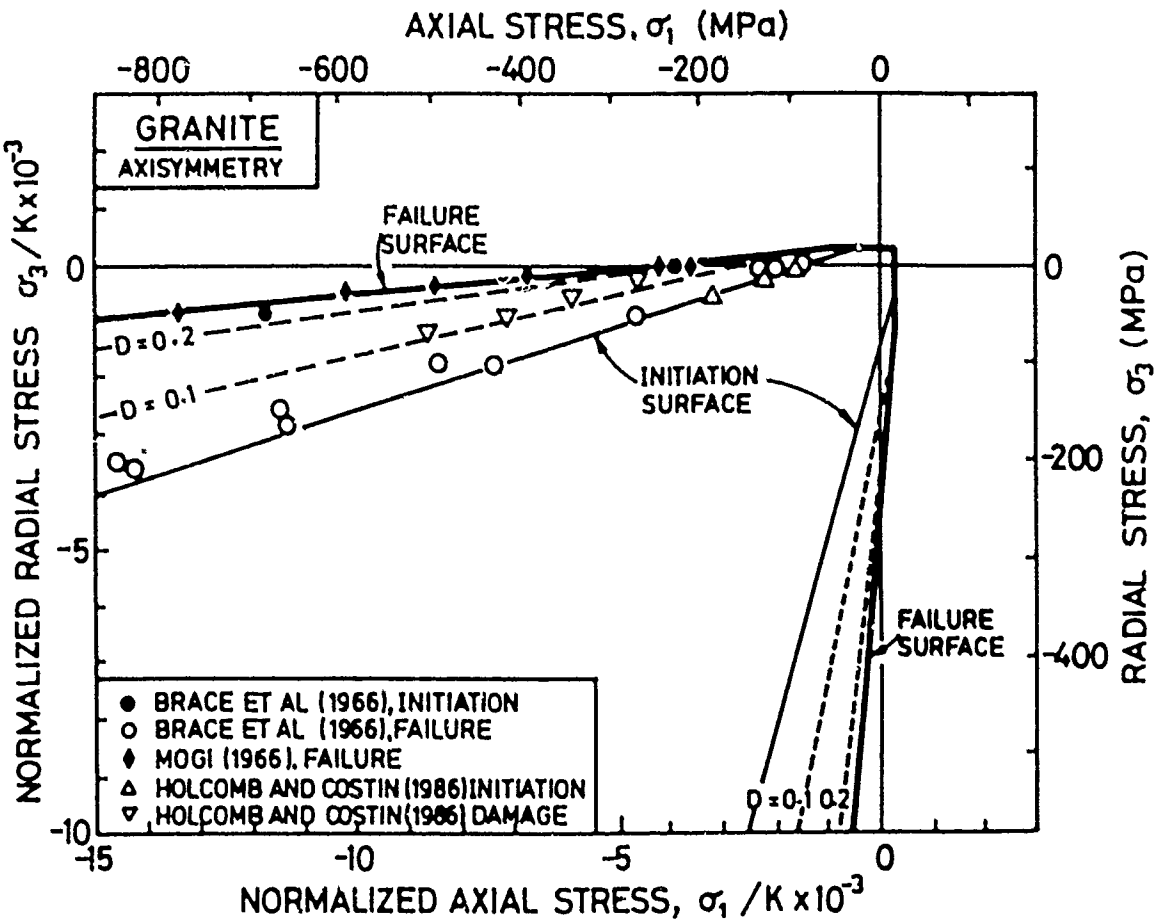

Figure 5a. Comparison between experimental and theoretical failure surfaces for granite at low and intermediate confining stress. Data and theory for microfracture initiation and surfaces of constant damage are also compared.

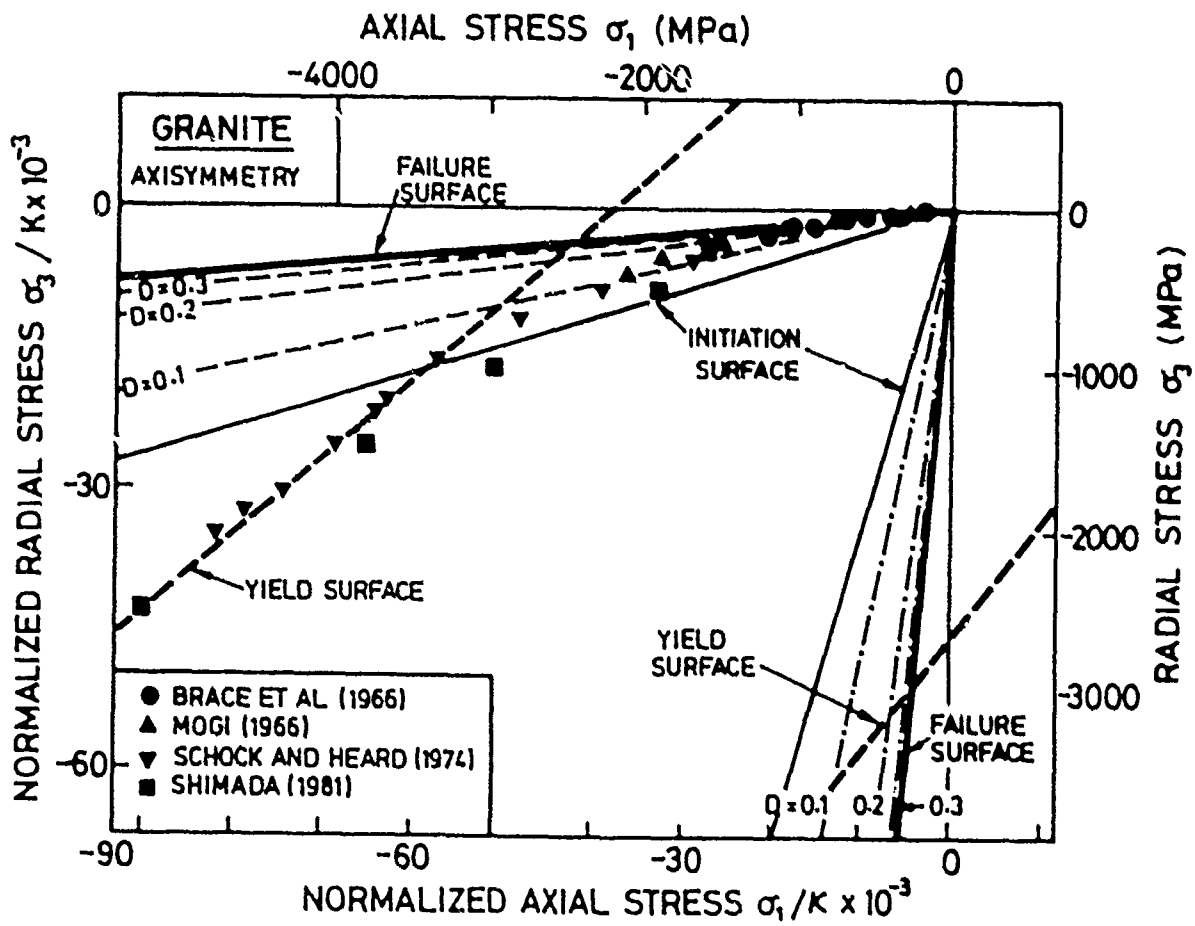

Figure 5b. Comparison between experimental and theoretical failure surfaces for granite exteded to the largest measured confining stress. The yield surface (equation 9) s also plotted as the heavy broken lines.

unstressed sample. Also shown is a surface of constant damage mapped by Holcomb and Costin (1986) using the AE Kaiser effect as a probe. The triaxial failure data are from Brace et al.. (1966) and Mogi (1966).

Figure 5b shows the failure surface extended out to large values of the confining stress where it intersects the yield surface. Data at low and intermediate confining pressures are from the same sources as in Figure 5a. Those at high confining pressures are from Schock and Heard (1974) for Westerly granite and from Shimada (1981) for Man-nari granite (grain size 1-3 mm, apparent porosity: 0.7%). It is evident that the failure surface has considerable curvature and deviates from our theoretical model at high confining pressures. Although Janach and Guex (1980) have modeled this curvature in terms of the formation of shear bubbles at the grain boundaries, Figure 5b supports the possibility that the curvature is due to a gradual transition to ductile behavior. Analogous curvature is evident in figures for limestone, marble, and NaCl (Ashby and Sammis, 1989) which are known to exhibit ductile behavior at moderate confining pressure, although the curvature in these rocks occurs over a more limited pressure range. The broader transition in granite may reflect its multimineralic composition for which the individual minerals have different brittle - ductile transition pressures. Note that the two granites show different transitional behavior at intermediate pressures, but that both approach the same ductile limit. Schock and Heard's observation that the stress- strain curve is linear to failure may be due to the convergence of the initiation and failure surfaces at very high confining pressures in

Figure 5b. The sudden release of energy and shear localization at failure do not preclude stress concentration by ductile processes in the weaker minerals.

APPLICATION TO LABORATORY SIMULATIONS IN GRANITE

The damage mechanics approach may be used to interpret the results of a recent set of laboratory simulations in granite which were designed to investigate the pulse-broadening observed in the field (Nagy and Florence, 1986). The results of these experiments are summarized in Table 2.

TABLE 2: LABORATORY SIMULATIONS

Sample Description	Pulse Shape
As received (dry)	Narrow
(wet)	Narrow
Thermally fractured (dry)	Narrow
(wet)	Narrow
Gas fractured (dry)	Narrow
(wet)	Slightly wider (2-3x)

The gas fractured samples were the most extensively fractured, and probably had the largest fractures since they were barely cohesive. Only these samples which contained water showed any pulse broadening. All other cases produced a narrow pulse in agreement with numerical predictions based on strength parameters measured in the laboratory.

We interpret the lack of pulse broadening in these simulations to be the consequence of a scaling effect which is inherent in the physics of crack growth. The stress necessary to nucleate and extend out-of-plane crack growth scales as the inverse square root of the initial flaw size. Since the maximum initial flaw size in the simulations is limited by the sample dimensions, the experimental results can be explained if these flaws are too short to be activated at the stress levels in the laboratory explosion.

Although quantitative verification of this explanation will require a full numerical simulation (which is in progress), the following approximate calculation illustrates the point. Consider the stress pulse at a distance of 204 m from the Piledriver explosion shown in Figure 6. This pulse was calculated by Rimer et al. (1987) using laboratory strength data for granite. At the stress peak, σ_{rr} = 334 MPa and $\sigma_{\theta\theta}$ = 135 MPa. Equations (5) and (6) were used to calculate the crack growth under this stress state and the results are shown in Figure 7a. For the dry case, it is expected that μ=0.6. For the saturated case, it is assumed that the water will hold the cracks open and $\mu \cong 0$. For either value of μ, the hoop stress is large enough that significant crack growth does not occur.

After the peak, the stresses fall to values of σ_{rr} = 33 MPa and $\sigma_{\theta\theta}$ = 2 MPa. Crack growth under these conditions is shown in Figure 7b. Note that in the dry case, cracks larger than about one meter show significant growth. Hence a model simulation using a sample with dimensions approximately equal to or smaller than one meter would not show weakening. For the wet case, cracks larger than about one centimeter show significant growth. Hence a meter size

sample might be expected to show some weakening effects if it were saturated. This is in agreement with the experimental observations summarized in Table 2.

SEISMIC PULSE BROADENING ASSOCIATED WITH FRACTURE DAMAGE

Equation (5) relates the current damage D to the state of stress. It can be used to generate a stress-strain curve if the elastic modulus is also known as a function of the damage. Sammis and Ashby (1986) show how the tangent moduli can be evaluated from the stress intensity factor to yield the following expressions for the radial modulus E_r and the axial modulus E_a :

$$E_r = E_0(1 - D) \tag{10}$$

$$E_a = E_0\left(1 - \frac{\pi^2}{\alpha c_3^2}\Gamma\right) \tag{11}$$

where

Stress-strain curves calculated using equations (5) and (10) - (12) have the general form shown in Figure 8c. As the rock is loaded, the microcracks extend out-of-plane as discussed above, that is, their length increases from L_0 to L_1 Crack growth and interaction produce a nonlinear stress-strain path. When the rock is unloaded, growth stops, and the crack length remains at L_1 during the unloading process. If the rock as a whole still behaves as an elastic body, then we have $\sigma_1 = E(L_1)\,\varepsilon$ for the unloading process.

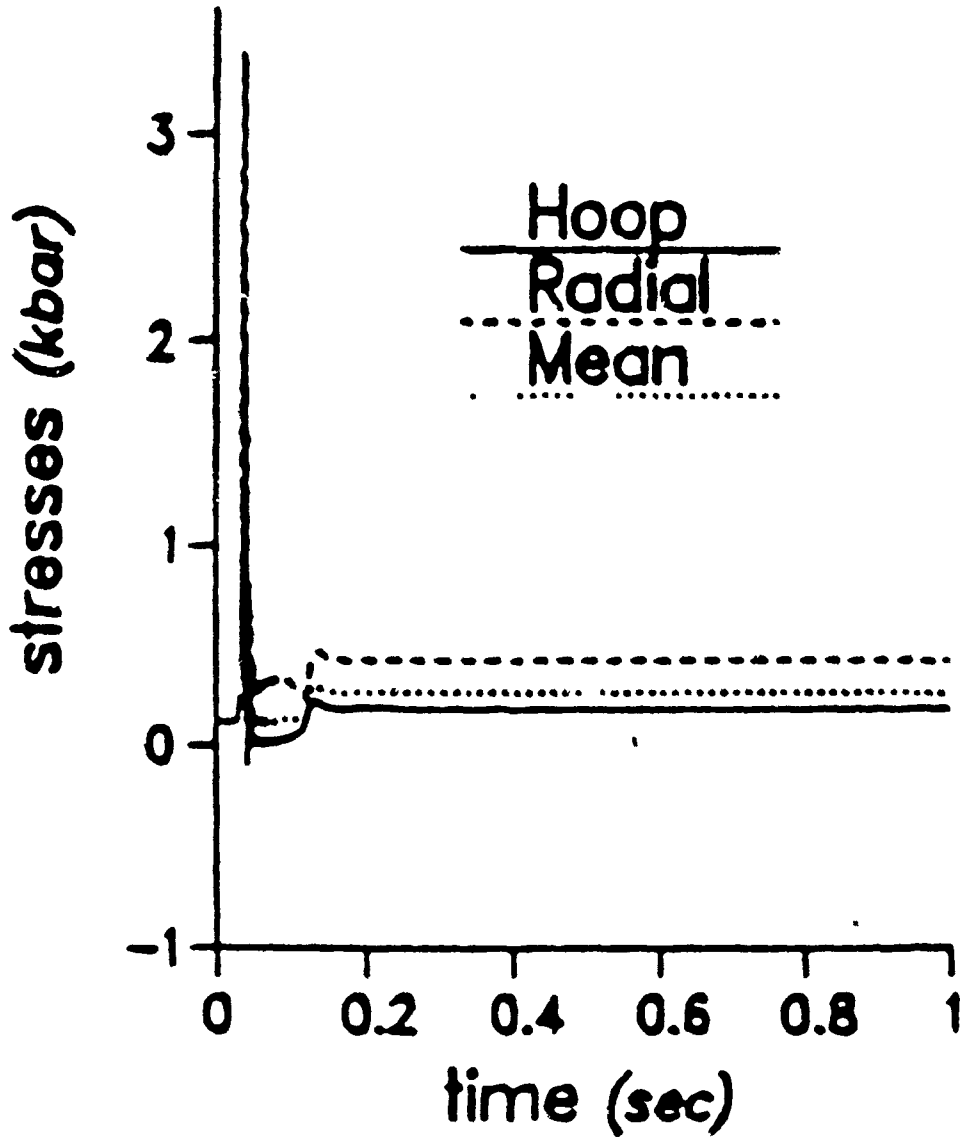

Figure 6. Stress pulse at a distance of 204 m. from the Piledriver explosion calculated by Rimer et al. (1987) using laboratory strength parameters for granite.

(a)

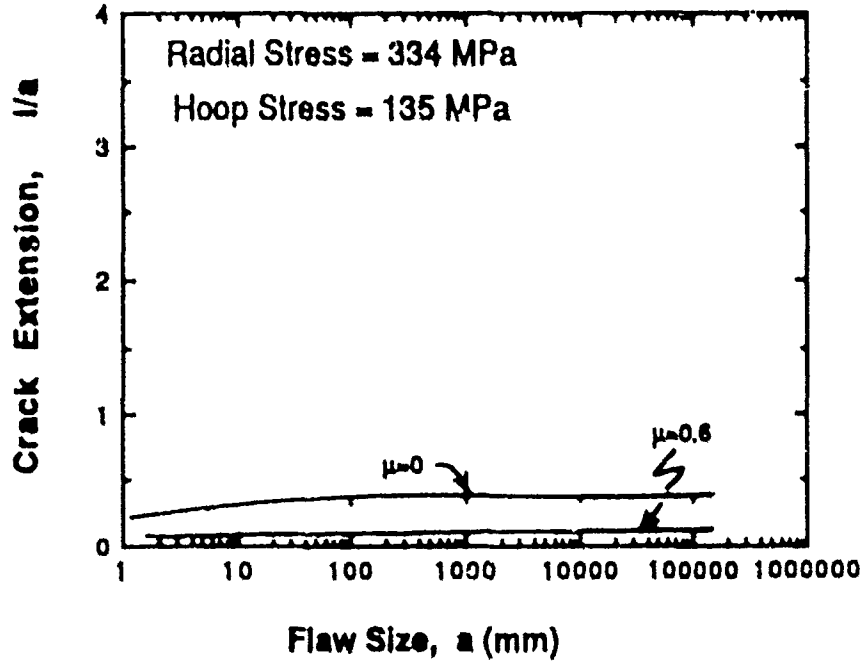

(b)

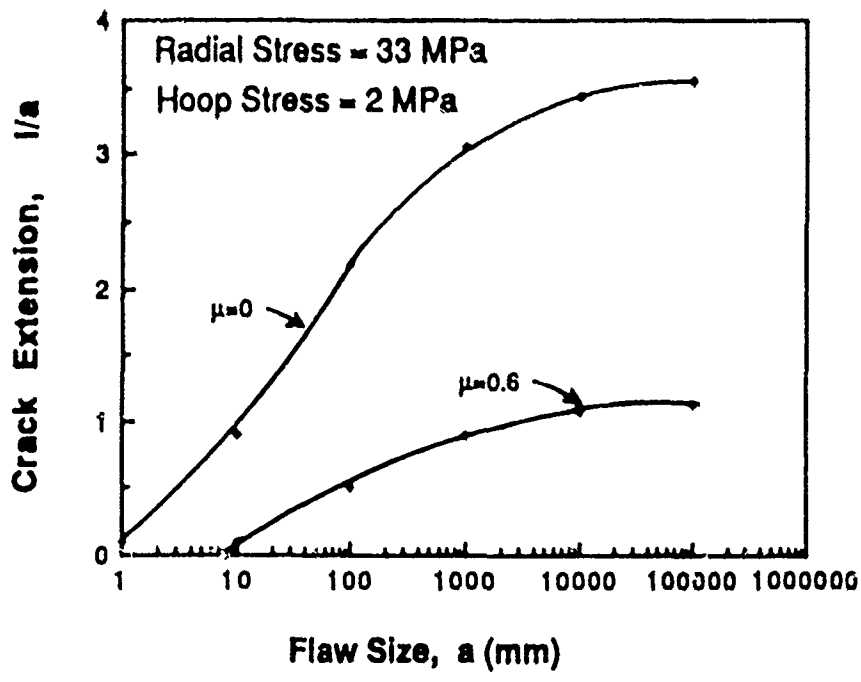

Figure 7. Crack extension as a function of the initial crack size. Case (a) is at the peak stress in Fig. 6 while case (b) is at a post-peak stress state.

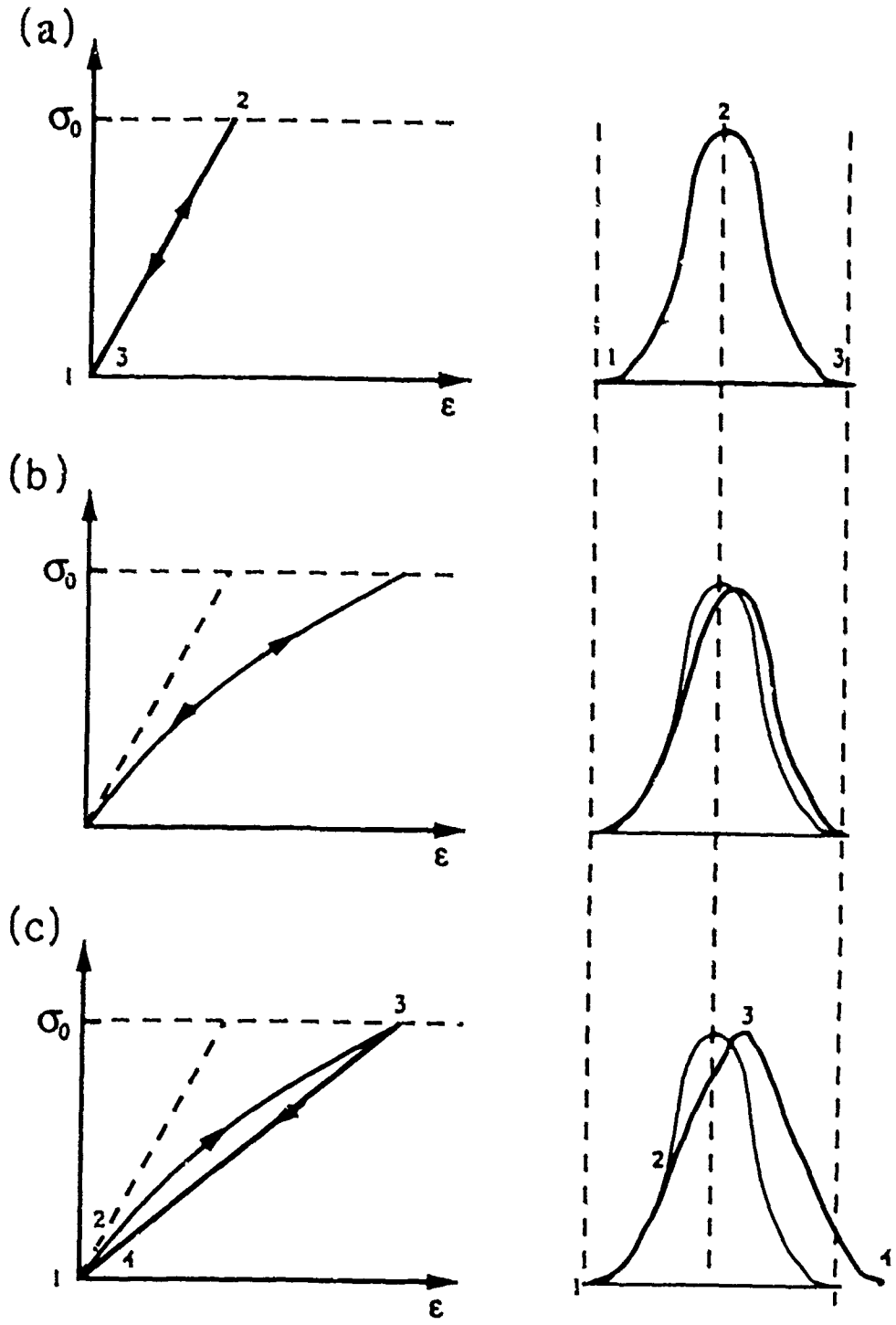

Figure 8. Stress strain curves and pulse-shape distortion for (a) the linear elastic case, (b) the non-linear elastic case, and (c) the damage mechanics case. Note that only the damage case produces pulse broadening.

Note that the unload is controlled by the secant modulus, not the tangent modulus which controls loading.

In order to investigate the effect of a damage-based rheology on the waveform, we assume a stress-strain curve which has the above behavior and is of the form:

$$\sigma = E_0\left(1 - e^{-\varepsilon/\varepsilon_0}\right) \qquad \text{for loading} \qquad (13)$$

$$\sigma = E_0\left(1 - e^{-\varepsilon/\varepsilon_0}\right)(\varepsilon/\varepsilon_1) \qquad \text{for unloading}$$

The basic equations which govern wave propagation in a damaged medium ar the equations of motion:

$$\rho \frac{\partial^2 u}{\partial t^2} = \frac{\partial \sigma}{\partial x} + f(x,t) \qquad (14)$$

The difference equations corresponding to eqns. (10) and (11) are:

$$u_n^{t+\Delta t} = 2u_n^t - u_n^{t-\Delta t} + \left(\eta^2 \Delta x\, \sigma_{n+1/2}^t - \sigma_{n-1/2}^t\right) + f_n^t \qquad (15)$$

$$\sigma_{n+1/2}^t = C\, \varepsilon_{n+1/2}^t$$

$$\varepsilon_{n+1/2}^t = \frac{\left(u_{n+1}^t - u_n^t\right)}{\Delta x}$$

$$\eta \equiv \sqrt{\frac{\mu}{\rho}}\left(\frac{\Delta t}{\Delta x}\right)$$

This formulation is a general one which includes the linear elastic case, the non-linear elastic case, and the damage case. The linear case was tested against the known analytic solution for the case where $\bar{r}(x, t)$ is a Gaussian function.

Waveforms calculated for the elastic, non-linear elastic, and damage cases are compared in Figure 8. For the elastic case, the shape of the response pulse is the same as that of the input force. As the input force increases for 0 to σ_0, the response increases from point 1 to point 2. As the input force decreases from σ_0 to 0, the response is from point 2 to 3. For the damage case, the response pulse can be divided into three segments. For the first segment, from point 1 to 2, the response is almost the same as the linear elastic case. The second segment, from point 2 to 3, deviates from the elastic case, in the sense that it propagates more slowly due to the change in slope of the stress-strain curve. The last segment, the unloading from 3 to 4 is elastic where the modulus is the secant modulus shown in Fig. 3. The result is that the response pulse for the damage case is wider than that for the elastic or the non-linear elastic cases.

DISCUSSION

We have developed a damage mechanics for compressive stress which has been verified using existing data for a wide variety of rocks (Ashby and Sammis, 1989). A simple one-dimensional application of this model provides a plausible explanation of the pulse broadening observed for underground explosions in granite. The scaling relation between the size of the preexisting flaws and the

stress required to increase damage offers an explanation of why such broadening is neither predicted by the rheological parameters measured on granite specimens in the laboratory nor observed in laboratory explosion simulations.

REFERENCES

Ashby, M. F. and S. D. Hallam (1986). The failure of brittle solids containing small cracks under compressive stress states, Acta metall., 34, 497-510.

Ashby, M. F. and C. G. Sammis (1989). The damage mechanics of brittle solids in compression, PAGEOPH, in press.

Atkinson, B. K. and P. G. Meredith (1987a). Experimental fracture mechanics data for rocks and minerals, in Fracture Mechanics of Rock, B. K. Atkinson editor, Academic Press, New York, pp. 477-525.

Brace, W. F., Paulding, B. W. and Scholz, C. (1966). Dilatancy in the fracture of crystalline rocks. J. Geophys. Res., 71, 3939-3953.

Cherry, J. T. and N. Rimer (1982). Verification of the effective stress and air void porosity constitutive model, S-Cubed Report VSC-TR-83-1.

Holcomb, D. J. and Costin, L. S. (1986). Damage in brittle materials: experimental methods, in Proceedings of the Tenth U.S. National Congress of Applied Mechanics, edited by Lamb, J. P., 107-113.

Janach, W. and Guex, L. H. (1980). In-plane propagation of shear microcracks in brittle rocks under triaxial compression, J. Geophys. Res., 85, 2543, 2553.

Mogi, K. (1966). Some precise measurements of fracture strength of rocks under uniform compressive stress, Rock. Mech. Eng. Geol., 4, 51-55.

Nagy, G. and A. Florence (1986). Spherical wave propagation in low porosity brittle rocks, SRI Report DNA-TR-86-000.

Nemat-Nasser, S. and H. Horii (1982). Compression induced nonplanar crack extension with application to splitting, exfoliation, and rockburst, J. Geophys. Res., 87, 6805.

Rimer, N., J. L. Stevens and S. M. Day (1987). Effect or pore-pressure, fractures, and dilatancy on ground motion in granite, S-Cubed Report SSS-R-87-8670.

Sammis, C. G. and M. F. Ashby (1986a). The failure of brittle porous solids under compressive stress states, Acta metall., 34, 511-526.

Schock, R. N. and Heard, H. C. (1974). Static mechanical properties and shock loading response of granite, J. Geophys. Res., 79, 1662-1666.

Scholz, C. H. (1982). Rock strength under confined shock conditions, S-Cubed Report SSS-R-83-5906.

Shimada, M. (1981). The method of compression test under high pressures in a cubic press and the strength of granite, Tectonophysics, 72, 343-357.

Zamyshlyayev, B. V., L. S. Yevterev and S. G. Krovosheyev (1980). Equations of rock state under explosion-induced loads, Doklady Akademii Nauk SSSR, 251, 323-326.

Appendix

THE DAMAGE MECHANICS OF BRITTLE SOLIDS IN COMPRESSION

M.F. Ashby* and C.G. Sammis+

*Cambridge University Engineering Department
Trumpington Street, Cambridge CB2 1PZ, England

+Department of Geological Sciences
University of Southern California
University Park, California 90089-0740, USA

in press
Pure and Applied Geophysics
1989

ABSTRACT

The development of microcrack damage in brittle solids in compression is analyzed, using a simple model. The model is developed from recent detailed analysis of the initialtion, propagation and linkage of microfractures from pre-existing cracks, voids, or other inhomogeneties. It describes the evolution of damage with strain and from it the stress-strain response, and criteria for failure, can be established. The results are used to construct failure surfaces in stress space which combine information about brittle failure with data describing the onset of plastic yielding. Such failure surfaces are constructed for a number of rocks and are compared with previously published experimental data.

1. INTRODUCTION

When a brittle solid is loaded to failure, it does so by the propagation of cracks. The cracks nucleate and propagate from inhomogeneities, by which we mean holes, inclusions, microcracks, surface scratches or other defects. The difference between compressive and tensile fracture is that in tension a single crack grows unstably (once started, it accelerates across the sample to cause failure) while in compression a population of small cracks extend stably, each growing longer as the stress is raised, until they interact in some cooperative way to give final failure (Figure 1). Because of this, the strength of a brittle solid in compression is usually greater, by a factor of ten or more, than that in tension.

Measurements of the crushing strength of stone, brick and of cement must have been of interest to civil engineers since pre-Roman times. Systematic measurements of compressive strength really began about the middle of the last century (for its history, see Jaeger and Cook, 1976) but without much attempt to understand what determined it, or why brittle materials had useful strength in compression but none to speak of in tension. Elucidation of the mechanics of brittle tensile fracture has its roots in the work of Griffith (1924), Irwin(1958) and others that followed (see Knott, 1973, for a review), which has led to the development of fracture mechanics as a branch of engineering design. The understanding of compressive brittle fracture is more recent, and still incomplete. A recent series of papers and reviews (Griggs and Handin, 1960; Paterson, 1978; Hallbauer et al., 1973; Tapponnier and Brace, 1976; Wawersik and Fairhurst, 1970; Wawersik and Brace, 1971; Nemat-Nasser and Horii, 1982; Newman, 1978; Ashby and Hallam, 1986; Sammis and Ashby, 1986) have established that an isolated crack in a large body grows stably until its length becomes comparable with the dimension of the body itself; and that when many cracks are present (as they always are in natural rocks, in brick, in concrete and most ceramics) the cracks grow stably until their length is comparable to their spacing when they interact, an instability develops, and the sample fails.

The problem can be complicated by time-dependent effects (Anderson and Grew, 1976; Martin, 1972; Waza et al., 1980; Sano et al., 1981, Costin and Holcomb, 1981; Atkinson and Meredith, 1987b), which have at least two origins. On the one hand crack growth can be limited by a chemical reaction, often with water. On the other, cracking in compression is associated with dilation; if the body is saturated with a fluid, then its flow into the dilating region can introduce a time-dependent aspect to fracture. In both cases, a static load which does not immediately cause failure may still do so if left in place for a sufficient length of time.

The understanding of compressive brittle fracture is still incomplete, but the mechanisms involved are much clearer than a decade ago. It seems an appropriate time to try to abstract from the new observations and modelling a simplified description of compression-cracking, basing it as far as possible on the physical understanding. The goal is to develop a damage mechanics of brittle solids, from which the stress-strain response and an operational definition of failure can be derived for a material with a given set of elastic properties and given defect population, under a given state of stress. Two attempts to achieve this can be found in the open literature; that of Costin (1983, 1985), and that of Sammis and Ashby (1986). Central to the problem is the relationship between stress and crack extension. Costin (1983, 1985) postulates a relationship of reasonable form, and develops from it expressions for the failure surface which (with some adjustable parameters) give a good description of the experimental data available at that time, but the model is not based on a physical model for crack growth. Sammis and Ashby (1986) and Ashby and Hallam (1986) use methods of fracture mechanics to develop a physical model for crack extension, which they use to plot stress-strain curves for brittle solids from which failure surfaces can be constructed, but the complexity of their model makes the process cumbersome. In the present paper we attempt to develop a simpler, model-based

mechanics of brittle compressive fracture, drawing heavily on the previous pieces of work.

2. CRACK INITIATION IN COMPRESSION

Most brittle solids contain inhomogeneities: small holes or cracks, particles which are poorly bonded, or phases which have different moduli or strengths from those of the matrix. Any one of these can act as nuclei for new cracks when the solid is loaded.

The range of possible nuclei is wide, but the spectrum of their characteristics is probably bracketed by two extremes: the spherical hole and the sharp inclined crack (Figure 2). Both have been studied experimentally and both have been modeled, the first by Sammis and Ashby (1986) and the second by Nemat-Nasser and Horii (1982) and Ashby and Hallam (1986). In both cases, the criterion for crack initiation, under axisymmetric loading has the form

$$\sigma_1 = c_1 \sigma_3 - \sigma_0$$

where c_1 and σ_0 are material properties, σ_1 is the axial stress, and $\sigma_2=\sigma_3$ the radial stress (both positive when tensile, negative when compressive).

In the later development of this paper we consider the growth of crack-damage from initial, inclined cracks as in Figure 2a. For this case (Nemat-Nasser and Horii, 1982; Ashby and Hallam, 1986) cracks initiate when

$$\sigma_1 = \frac{\left(1+\mu^2\right)^{1/2} + \mu}{\left(1+\mu^2\right)^{1/2} - \mu}\,\sigma_3 - \frac{\sqrt{3}}{\left(1+\mu^2\right)^{1/2} - \mu}\,\frac{K_{Ic}}{\sqrt{\pi a}} \qquad (1)$$

where μ is the coefficient of friction acting across the crack faces, K_{Ic} is the fracture toughness of the material through which the new crack propagates, and 2a is the length of the original inclined crack. Rocks, typically, show a coefficient of friction of about 0.6, in which case $C_1 = 3.1$ and $\sigma_0 = 3.1\, K_{Ic}/\sqrt{\pi a}$. Crack initiation from holes (Sammis and Ashby, 1986) gives similar values.

Crack initiation can be detected in several ways: by the start of acoustic emission, by the first non-linearity of the stress-strain curve, by the dilation of the sample, or by a sudden increase in internal friction. None give very accurate data, but they do allow a test of eqn. (1). Figure 3 shows data for crack initiation in Westerly granite obtained by the first three techniques (Holcomb and Costin, 1986; Brace et al., 1966) plotted on axes of σ_1 and σ_3 to allow comparison with eqn. (1). The linear relationship gives a good description of the data with a slope between 2.7 and 3.3 (corresponding to μ = 0.55 to 0.64) and an intercept of 70 - 79 MPa (corresponding to a crack length 2a close to 1 mm when K_{Ic} = 1 MPa $m^{1/2}$).

The theory gives an adequate description of the data. It is used to describe the initiation of damage in the diagrams shown later. In each case, experimental data are fitted to eqn (1) to give μ and a (using published data for K_{Ic}). Results of this analysis are summarized in Table 2. In the computations, it is convenient to normalize the equations by the quantity $K_{Ic}/\sqrt{\pi a}$, giving

$$S_1 = c_1 S_3 - S_0 \qquad (2)$$

with

$$S_1 = \sigma_1 \sqrt{\pi a}/K_{Ic} \qquad (3)$$

$$S_3 = \sigma_3 \sqrt{\pi a}/K_{Ic}$$

$$c_1 = \frac{\left(1+\mu^2\right)^{1/2} + \mu}{\left(1+\mu^2\right)^{1/2} - \mu}$$

$$S_0 = \frac{\sqrt{3}}{\left(1+\mu^2\right)^{1/2} - \mu}$$

3. CRACK GROWTH AND INTERACTION

Once initiated, the wing cracks (as we shall call the crack-like extensions of the original flaw) grow longer. During growth, the stress intensity K_I at the tip of each wing crack is equal to, or exceeds, the fracture toughness K_{Ic} of the solid. The condition for crack advance is simply

$$K_I \geq K_{Ic}$$

The difference between tension and compression, as already mentioned, is that growth in compression is stable: each increment of crack advance requires an increment of load, at least until the cracks start to interact strongly. We will assume that a steadily increasing load drives the cracks at a steady rate, though in reality the inhomogeneity of natural materials may cause them to extend in little jumps. The problem, then, is to calculate K_I at the tip of the wing cracks.

3.1 Crack Growth from Starter Flaws of a Single Size : The 2-Dimensional Case

Figure 4 shows an array of through-cracks, growing in a linear-elastic medium under a triaxial stress field σ_1 , σ_3 , positive when tensile, negative when compressive. Consider first the growth of a single, isolated crack from an initial inclined flaw; interaction comes later. The upper inset of Figure 4 isolates one crack: it is made up of an initial crack of length 2a lying at an angle ψ to the X_1 direction with two wings, each of length l which (we will assume) lie parallel to X_1. The stress intensity at the tips of the wings is obtained approximately, but adequately, in the following way, based on the work of Nemat-Nasser and Horii (1982), Ashby and Hallam (1986), Horii and Nemat-Nasser (1985, 1986), and Kemeny and Cook (1986).

The remote field σ_1, σ_3 creates a shear stress τ and a normal stress σ across faces of the initial crack. The crack slides (resisted by the coefficient of friction μ), wedging open the mouth of each wing crack by δ (Figure 4). The wedging can be thought of as caused by forces, F_3, parallel to X_3, acting at the midpoint of the crack. The stresses τ and σ are given by

$$\tau = \frac{\sigma_3 - \sigma_1}{2} \sin 2\psi \qquad (4a)$$

$$\sigma = -\frac{\sigma_3 + \sigma_1}{2} + \frac{\sigma_3 - \sigma_1}{2} \cos 2\psi \qquad (4b)$$

F_3 is simply the component of the sliding force acting parallel to X_3:

$$F_3 = (\tau + \mu\sigma)\ 2a \sin\psi \qquad (5a)$$

or

$$F_3 = -\left(A_1 \sigma_1 - A_3 \sigma_3\right) a \qquad (5b)$$

where A_1 and A_3 are constants which depend on ψ, to be determined in a moment.

The force F_3 acting at the mid point of a crack of length 2l creates a stress intensity tending to open the crack (Tada et al., 1985, page 5.1) of

$$(K_I)_1 = \frac{F_3}{\sqrt{\pi l}}$$

This result gives a good estimate of the stress intensity at the tip of a wing crack when l is large, but it breaks down (becoming infinite) when l is vanishingly small. The stress intensity at the tip of the initial inclined crack is not infinite, but can be calculated exactly as explained in the last section. We overcome this problem by introducing an "effective" crack length (l + βa) giving

$$(K_I)_1 = \frac{F_3}{\sqrt{\pi (l+\beta a)}} \qquad (6)$$

We then choose β so that $(K_I)_1$ becomes equal to that for the inclined crack when l is zero.

Before doing this, we note that there is another contribution to K_I at the tip of the wing crack. The remote confining stress σ_3 acts not just on the angled crack but on the wing cracks of length l. In so doing, it produces an additional contribution to the stress intensity, tending to close the crack when σ_3 is compressive (Tada et al., 1985, page 5.1):

$$(K_I)_3 = \sigma_3 \sqrt{\pi l} \qquad (7)$$

Summing the two contributions, with F_3 given by eqn (5b), gives:

$$K_I = \frac{F_3}{\sqrt{\pi (l+\beta a)}} + \sigma_3 \sqrt{\pi l} \qquad (8a)$$

$$= - \frac{A_1 \sigma_1 \sqrt{\pi a}}{\pi \sqrt{L+\beta}} + \sigma_3 \sqrt{\pi a} \left(\frac{A_3}{\pi \sqrt{L \div \beta}} + \sqrt{L} \right) \qquad (8b)$$

where L = l /a. The cracks extend until K_I becomes equal to K_{Ic}.

The constants are found by ensuring that this equation reduces to the exact result for crack initiation (L = 0) and matches the known results for very long cracks (L >> 1), given by Nemat-Nasser and Horii (1982) and Ashby and Hallam (1986), eqns. (3) and (6). This gives

$$A_1 = \frac{\pi \sqrt{\beta}}{\sqrt{3}} \left(\left(1 + \mu^2 \right)^{1/2} - \mu \right) \qquad (9)$$

$$A_3 = A_1 \left\{ \frac{\left(1 + \mu^2 \right)^{1/2} + \mu}{\left(1 + \mu^2 \right)^{1/2} - \mu} \right\}$$

$$\beta = 0.1$$

Equation (8b) with the values of A_1, A_3, and β (and with $K_I = K_{Ic}$) is plotted in Figure 5. It shows $\sigma_1 \sqrt{\pi a} / K_{Ic}$ plotted against L with the earlier numerical results of Nemat-Nasser and Horii (1982). Equation (8) is obviously a good approximation to the earlier calculations.

Now the interaction. The main part of Figure 4 shows an array of N_A cracks per unit area, all of which have extended to a length 2(l + α a.) The center-to-center spacing of the cracks is

$$S = \frac{1}{\sqrt{N_A}} \qquad (10)$$

so that an uncracked ligament of average length $S - 2(l + \alpha a)$ remains between the cracks in the X_1 direction. (Here α is simply a geometric constant, and must be distinguished from β; for cracks at 45° to X_1, $\alpha = 1/\sqrt{2}$). An opening force F_3 acts at the midpoint of each crack. Equilibrium requires that this opening force be balanced by a mean internal stress σ_3^i in the matrix, as shown in the right hand side of Figure 4. The average internal stress is given by

$$\sigma_3^i = \frac{F_3}{S - 2(l + \alpha a)} \tag{11}$$

This acts on the wing cracks, so that eqn (7) now becomes

$$(K_I)_3 = \left(\sigma_3 + \sigma_3^i\right)\sqrt{\pi l} \tag{12}$$

We now define the initial damage D_0 and the current damage D by:

$$D_0 = \pi(\alpha a)^2 N_A \tag{13a}$$

$$D = \pi(l + \alpha a)^2 N_A \tag{13b}$$

giving

$$\sigma_3^i = \frac{-(A_1\sigma_1 - A_3\sigma_3)(D_0/\pi)^{1/2}}{\alpha\left(1 - 2(D/\pi)^{1/2}\right)} \tag{14}$$

Equations (8a) and (8b) now become

$$K_I = \frac{F_3}{\left(\pi\left(\iota + \beta\, a\right)\right)^{1/2}} + \left(\sigma_3 + \overset{i}{\sigma_3}\right)\sqrt{\pi\, l} \qquad (15a)$$

$$= \frac{-A_1\,\sigma_1\sqrt{\pi\, a}}{\pi\sqrt{\alpha}\left(\left(\frac{D}{D_0}\right)^{1/2} - 1 + \frac{\beta}{\alpha}\right)^{1/2}} \left\{ \left(1 - \frac{A_3}{A_1}\lambda\right)\left[1 + \left(\frac{\pi\left(\frac{D_0}{\pi}\right)^{1/2}}{1 - 2\left(\frac{D}{\pi}\right)^{1/2}} \right) \cdot \right.\right.$$

$$\left.\left. \cdot \left(\left(\frac{D}{D_0}\right)^{1/2} - 1\right)\right] - \frac{\pi\,\alpha\,\lambda}{A_1}\left(\left(\frac{D}{D_0}\right)^{1/2} - 1\right)\right\} \qquad (15b)$$

Here the first term in the curly brackets describes the wedging plus the crack-crack interaction; and the second term describes the closing effect of the lateral confining stress. The cracks propagate until K_I falls to K_{Ic}. Using this, rearranging and aggregating the constants (with $\sqrt{2/\pi} \approx 1$) gives for proportional loading (with $\lambda = \sigma 3 / \sigma 1$ held constant) :

$$S_1 = \frac{-C_2\left(\left(\frac{D}{D_0}\right)^{1/2} - 1 + \frac{\beta}{\alpha}\right)^{1/2}}{\left(1 - C_1\lambda\right)\left\{ 1 + \frac{C_3 D_0^{1/2}}{\left(1 - D^{1/2}\right)}\left(\left(\frac{D}{D_0}\right)^{1/2} - 1\right)\right\} - C_4\lambda\left(\left(\frac{D}{D_0}\right)^{1/2} - 1\right)} \qquad (16)$$

and for loading at constant $\sigma 3$

$$S_1 = -\left(\frac{C_2\left(\left(\frac{D}{D_0}\right)^{1/2} - 1 + \frac{\beta}{\alpha}\right)^{1/2} - S_3\left[C_1\left(1 + \left(\frac{C_3 D_0^{1/2}}{1 - D^{1/2}}\right)\left(\left(\frac{D}{D_0}\right)^{1/2} - 1\right)\right) + C_4\left(\left(\frac{D}{D_0}\right)^{1/2} - 1\right)\right]}{1 + C_3 \frac{D_0^{1/2}}{\left(1 - D^{1/2}\right)}\left(\left(\frac{D}{D_0}\right)^{1/2} - 1\right)} \right) \qquad (17)$$

where S_1 and S_3 are defined by equation (3). The values of the constants are

$$C_1 = \frac{A_3}{A_1} = \frac{\left(1+\mu^2\right)^{1/2} + \mu}{\left(1+\mu^2\right)^{1/2} - \mu}$$

$$C_2 = \frac{\pi\sqrt{\alpha}}{A_1} = \frac{\sqrt{3\alpha/\beta}}{\left(1+\mu^2\right)^{1/2} - \mu} \qquad (18)$$

$$C_3 = \sqrt{\pi}$$

$$C_4 = \frac{\pi\alpha}{A_1} = \frac{\sqrt{3/\beta}}{\left(1+\mu^2\right)^{1/2} - \mu}$$

Figure 6 shows how the axial stress σ_1 varies with damage D for various confining pressures. The left hand figure shows proportional loading; the right hand figure , loading at constant σ_3. The peak stress, $(\sigma_1)_{max}$, rises and moves to the right as λ or σ_3 is increased. The shapes of the curves at constant λ differ from

those at constant σ_3, as expected, but the peaks are at the same stress. Figure 7 shows $(\sigma_1)_{max}$ plotted against σ_3 for both conditions: the points lie on the same line.

3.2 Crack Growth from Starter Flaws of a Single Size. The 3-dimensional Case

It is usually the case that flaws are completely contained within the material. The merit of the 2-dimensional calculations developed in section 3.2 is that it points to a way of tackling this more difficult 3-dimensional problem. We require the stress intensity at the periphery of a contained crack emanating from a starter flaw (which we take to be an inclined, penny-shaped crack) which we will equate, as before, to K_{Ic} . This we do by calculating the wedging force F_3 as in the 2-dimensional case. The wedging force creates an average internal stress σ_3^i . The stress intensity at the tip of a given wing crack is calculated from the wedging force and the total lateral stress $(\sigma_3 + \sigma_3^i)$, as shown in Figure 8. The significant difference in the results of this 3-D and the earlier 2-D calculations is that the dependence of S_1 and S_3 on damage D involves different powers.

The wedging force F_3, as before, is calculated from the shear and normal stresses (eqn 4) acting on the initial crack plane, times the crack area, resolved into the X_3 direction:

$$F_3 = (\tau + \mu\sigma)\pi a^2 \sin\psi$$

$$= -(A_1\sigma_1 - A_3\sigma_3)a^2 \qquad (19)$$

Unlike the 2-D case, there are no exact analytical solutions for limiting cases which allow A_1 and A_3 to be determined, so we make the assumption that they have the same values as before (equation 9) but make provision to adjust them later to match experimental data.

The stress intensity K_I has the same three contributions as before. The wedging force F_3 induces a stress intensity (Tada et al., 1985, page 24.2)

$$(K_I)_1 = \frac{F_3}{\left(\pi\,(l+\beta\,a)\right)^{3/2}} \qquad (20)$$

where β is introduced for the same reason as before: to give a limiting value of $(K_I)_1$ when $l = 0$. The contribution due to σ_3 and σ_3^i are (Tada et al., 1985, page 24.2).

$$(K_I)_3 = \frac{2}{\pi}\left(\sigma_3 + \sigma_3^i\right)\sqrt{\pi\,l} \qquad (21)$$

The internal stress for the 3-D case is

$$\sigma_3^i = \frac{F_3}{A - \pi\left(l+\alpha\,a\right)^2} \qquad (22)$$

where $\pi\left(l+\alpha\,a\right)^2$ is the total crack area projected normal to X_3 and A is the area per crack

$$A = \pi^{1/3}\left(\frac{3}{4\,N_V}\right)^{2/3} \qquad (23)$$

where N_V is the number of cracks per unit volume.

Damage is defined in a way which parallels that in 2-dimensions:

$$D_o = \frac{4}{3}\pi\,(\alpha\,a)^3\,N_v \qquad (24a)$$

$$D = \frac{4}{3}\pi\,(l+\alpha\,a)^3\,N_v \qquad (24b)$$

giving

$$\sigma_3^i = \frac{-(A_1\sigma_1 - A_3\sigma_3)D_0^{2/3}}{\pi\alpha^2(1-D^{2/3})} \qquad (25)$$

The stress intensity at the tip of the wing crack is

$$K_I = \frac{F_3}{(\pi(l+\beta a))^{3/2}} + \frac{2}{\pi}(\sigma_3 + \sigma_3^i)\sqrt{\pi l} \qquad (26)$$

$$= \frac{-A_1\sigma_1\sqrt{\pi a}}{\pi^2\alpha^{3/2}((D/D_0)^{1/3} - 1 + \beta/\alpha)^{3/2}}\left\{\left(1 - \frac{A_3}{A_1}\lambda\right)\left[1 + 2((D/D_0)^{1/3} - 1)^2\left(\frac{D_0^{2/3}}{1-D^{2/3}}\right)\right]\right.$$

$$\left. - \frac{2\lambda}{A_1}\alpha^2\pi^2((D/D_0)^{1/3} - 1)^2\right\}$$

As before the cracks propagate until K_I falls to K_{Ic}. Rearranging and aggregating the constants the gives, for proportional loading:

$$S_1 = \frac{-C_2\left(\left(\frac{D}{D_0}\right)^{1/3} - 1 + \frac{\beta}{\alpha}\right)^{3/2}}{(1-C_1\lambda)\left\{1 + \frac{C_3 D_0^{2/3}}{(1-D^{2/3})}\left(\left(\frac{D}{D_0}\right)^{1/3} - 1\right)^2\right\} - C_4\lambda\left(\left(\frac{D}{D_0}\right)^{1/3} - 1\right)^2} \qquad (27)$$

and for loading at constant σ_3

$$S_1 = -\left(\frac{C_2\left(\left(\frac{D}{D_0}\right)^{1/3} - 1 + \frac{\beta}{\alpha}\right)^{3/2} - S_3\left[C_1\left(1 + \left(\frac{C_3 D_0^{2/3}}{1 - D^{2/3}}\right)\left(\left(\frac{D}{D_0}\right)^{1/3} - 1\right)^2\right) + C_4\left(\left(\frac{D}{D_0}\right)^{1/3} - 1\right)^2\right]}{1 + C_3 \frac{D_0^{2/3}}{\left(1 - D^{2/3}\right)}\left(\left(\frac{D}{D_0}\right)^{1/3} - 1\right)^2} \right) \qquad (28)$$

where S_1 and S_3 are defined by equations (3). The values of the constants are,

$$C_1 = \frac{A_3}{A_1} = \frac{\left(1+\mu^2\right)^{1/2} + \mu}{\left(1+\mu^2\right)^{1/2} - \mu}$$

$$C_2 = \frac{\pi^2 \alpha^{3/2}}{A_1} = \pi \alpha \sqrt{\frac{3\alpha}{\beta}}\left(\left(1+\mu^2\right)^{1/2} - \mu\right) \qquad (29)$$

$$C_3 = 2$$

$$C_4 = \frac{2\alpha^2 \pi^2}{A_1} = 2\alpha^2 \sqrt{\frac{3}{\beta}}\left(\left(1+\mu^2\right)^{1/2} - \mu\right)$$

The equations and constants have a form very like those of the 2-dimensional model. Two significant differences should be noted. First, the extra dimension causes the powers of D which appear in the equation to differ (not surprisingly) from those of the 2-D model. Second, the constants C_1 to C_4 are not known with the same precision as those of the 2-D model because accurately-known limiting cases are not available to calibrate them. We shall assume

(reasonably) that the dependence on the coefficient, μ, is properly included, but that the constant β may require further adjustment to give a good match with experiment.

Figures 9 and 10 illustrate some features of the results. The axial stress at first rises as damage grows (Figure 9), passing through a peak which shifts to higher values of damage as the confining pressure increases. The damage surface, shown in Figure 10, is almost a cone meaning that, to a first approximation, the failure envelope is described by

$$\sigma_1 = C\sigma_3 - \sigma_C$$

where C is a constant and σ_C is the unconfined compressive strength. The value of the model is that it gives a physical interpretation to C and σ_C, and relates them to the initial damage, the coefficient of friction, and the crack size.

4. ANALYSIS OF DATA

The strength of many different rocks have been determined under triaxial loading conditions ($|\sigma_1| > |\sigma_2| = |\sigma_3|$, where all three principal stresses are compressive) . For a few, the initiation of microcracking has also been determined. We now apply the damage mechanics model developed above to nine different rock types for which the most complete data sets exist : granite, aplite, dunite, eclogite, gabbro, sandstone, limestone, marble and rock salt. These rocks represent a wide range of composition and initial damage. Granite, aplite, dunite and eclogite are low porosity, crystalline, igneous rocks in which the initial damage is mostly in the form of low aspect cracks. Limestone and sandstone are porous sedimentary rocks in which the initial damage is mostly in the form of high aspect pores. Marble is a metamorphic rocks with initial damage of a form intermediate between the previous two extremes. These rocks also span a wide range of yield strength. The igneous rocks have yield strengths in excess of 2 GPa

while the calcareous rocks (limestone and marble) yield at stresses below 1 GPa. Rock salt is at the low extreme with a yield strength below 100 MPa.

The damage mechanics model formulated above has three constants: μ, α, and β. They are not strictly adjustable because the theory makes predictions for their values. However because of approximations in the derivation, and the uncertainties in the aspect ratio of the starter flaws, we have treated β as adjustable, choosing the value 0.45 to give the best fit to the data.

For those materials where crack initiation data are available, the crack length 2a and the coefficient of friction μ are determined from the initiation surface (see Table 2)

$$\sigma_1 = C_1 \sigma_3 + \sigma_0$$

where C_1 and σ_0 are given by equation (1). K_{Ic} is also required. Although K_{Ic} may be estimated for most rocks (Atkinson and Meredith, 1987a), the starter flaw size is not known in most cases and must be treated as an adjustable parameter. The derivation of the fundamental equations (27) and (28) from equation (26) gives $C_3 = 2$, and this gives a good description of the materials we have examined.

Each material will now be discussed in turn. The triaxial data for damage initiation and failure are presented on plots of σ_1 vs σ_3 . The theoretical fracture initiation surface (eqn. 1), surfaces of constant damage, and the failure surface (calculated from the maximum of eqn. (28) for each value of σ_3) are plotted on these graphs for comparison with the data.

As the confining pressure is increased, brittle fracture is made increasingly difficult. A critical pressure may be reached at which true plasticity replaces crack extension. This transition can be illustrated by plotting a yield (or creep) surface, defined by:

$$\sigma_y^2 = \frac{1}{2}\left[(\sigma_1 - \sigma_2)^2 + (\sigma_2 - \sigma_3)^2 + (\sigma_3 - \sigma_1)^2\right] \qquad (30)$$

The yield surface is plotted as a pair of heavy broken lines on each figure The yield strength, σ_y, can be derived from hardness, H, data since $\sigma_y = H/3$. The material properties and constants used to generate the theoretical initiation and failure curves are tabulated for each solid.

4.1 Granite

Westerly granite is a fine-grained (0.75 mm.), low porosity (0.9%), isotropic, two-mica calc-alkaline granite which has become a standard material in rock mechanics testing (see Scholz, 1986, for a b.'ef history). Mineralogical modal analyses are given by Birch (1960) and Wawersik and Brace (1971).

Figure 11a shows theoretical surfaces for initiation, constant damage, and failure at low values of the confining stress. The fracture initiation data from Brace et al. (1966) were determined from the onset of non-linear behavior of the volume strain. Only data taken at the highest loading rate are plotted here in order to minimize effects of subcritical crack growth (which we do not model). The three initiation points from Holcomb and Costin (1986) were determined from the onset of acoustic emission (AE) in a previously unstressed sample. Also shown is a surface of constant damage mapped by Holcomb and Costin (1986) using the AE Kaiser effect as a probe. The triaxial failure data are from Brace et al. (1966) and Mogi (1966).

Figure 11b shows the failure surface extended out to large values of the confining stress where it intersects the yield surface. Data at low and intermediate confining pressures are from the same sources as in Figure 11a. Those at high confining pressures are from Schock and Heard (1974) for Westerly granite and from Shimada (1981) for Man-nari granite (grain size 1-3 mm, apparent porosity: 0.7%). It is evident that the failure surface has considerable

curvature and deviates from our theoretical model at high confining pressures. Although Janach and Guex (1980) have modeled this curvature in terms of the formation of shear bubbles at the grain boundaries, Figure 11b supports the possibility that the curvature is due to a gradual transition to ductile behavior. Analogous curvature is evident in subsequent figures for limestone, marble, and NaCl which are known to exhibit ductile behavior at moderate confining pressure, although the curvature in these rocks occurs over a more limited pressure range. The broader transition in granite may reflect its multimineralic composition for which the individual minerals have different brittle - ductile transition pressures. Note that the two granites show different transitional behavior at intermediate pressures, but that both approach the same ductile limit. Schock and Heard's observation that the stress- strain curve is linear to failure may be due to the convergence of the initiation and failure surfaces at very high confining pressures in Figure 11b. The sudden release of energy and shear localization at failure do not preclude stress concentration by ductile processes in the weaker minerals.

4.2 Aplite

Brace et al. (1966) studied a quartz-oligoclase aplite (63% oligoclase, 27% quartz, and 10% biotite) which they described as fine-grained and flinty, apparently isotropic, and of high strength. The feldspar is highly altered. The grain size of the ground mass is about 40 μm and of the phenocrysts, about 100 μm. The small grain size and high strength are consistent with the small flaw size required by the model (see Figure 12). The relatively high initial damage is consistent with the flinty texture. A high density of small flaws may explain why flinty materials can be reliably fashioned into tools by flaking off small bits in a controllable manner.

4.3 Dunite

Dunite is an almost pure olivine rock. Shimada et al. (1983) measured the compressive strength of Horoman dunite (grain size 0.1-0.9 mm) at confining pressures up to 450 MPa using a conventional triaxial testing apparatus and to 3 GPa using a cubic press. Acoustic emissions showed a change in failure mode at confining pressures between 0.44 and 0.77 GPa. Below these pressures, AE activity increased rapidly between the onset of dilatancy and failure (the typical pattern for brittle failure). Above the transition pressure, and increase in AE activity was not observed to precede failure; rather, the level of AE remained nearly constant up to failure. Shimada et al. (1983) correlate this change in AE behavior with the extreme curvature in the failure envelope. As is evident in Figure 13, our model suggest that this change in behavior is associated with the transition to plastic deformation.

4.4 Eclogite

Eclogite is an ultramafic pyroxene-garnet rock. The Akaishi eclogite measured by Shimada et al. (1983) was composed of 0.1-0.3 mm pyroxene grains and 0.8-2.3 mm garnet grains. It had a density of 3.642 gm/cm^3 and a porosity of 0.4%. Conventional triaxial tests covered a range of confining pressures from 0 to 450 MPa while tests in an opposed anvil cubic press extended the confining pressure to 3 GPa. As discussed above for dunite, the AE patterns indicate a change in failure mechanism at confining pressures between 1.02 and 1.99 GPa. The data and theoretical surfaces are given in Figure 14.

4.5 Gabbro

In addition to dunite and eclogite discussed above, Shimada et al. (1983) also studied Murotomisaki gabbro, a hypersthene-bearing-olivine-augite gabbro. The grain size of the olivine component is 1-2 mm, pyroxene is about 0.7 mm, and the plagioclase is about 0.7-3 mm. The bulk density is 2.985 gm/cm^3 and the reported porosity is 0.4%. The pattern of AE indicated a change in failure mechanism at

confining pressures between 0.51 and 0.76 GPa. The data and theoretical surfaces are given in Figure 15.

4.6 Sandstone

The sandstone data in Figure 16 were obtained in triaxial compression by Gowd and Rummel (1980). The rock is described as a medium grain-sized Bunsandstone from SW-Germany with subangular to round quartz grains bedded within a clayey matrix.. Its initial porosity was 15% with an initial permeability of 50 microdarcy. The damage initiation data were defined by the onset of dilatancy. At confining pressures above about 30 MPa, the stress-strain curves are nonlinear at lower values of the axial stress than the observed onset of dilatancy. This probably reflects the suppression of dilatancy by pore collapse, a phenomenon which the authors propose to explain the total lack of observed dilatancy at the highest confining pressures. Such effects are beyond the scope of our model.

A transition from brittle failure to apparent ductile shear deformation takes place at a pressure of about 100 MPa. However, the observed pressure dependence of the flow stress for confining pressures in excess of 100 MPa argues against true ductile flow and for a cataclastic mode of deformation probably involving pore collapse. Dilatancy at failure is a constant for confining pressures between 0 and 40 MPa. From 40 to 100 MPa, dilatancy at failure decreases to zero. Above 100 MPa, brittle failure does not occur.

4.7 Limestone

Solenhofen limestone is a fine grained (0.01 mm) mechanically isotropic limestone from Bavaria. It has a connected porosity of 5.3% and a total porosity in the range 6 - 9% (Rutter, 1972). The strength data in Figure 17 are from Heard (1960) and include both triaxial compression and tension. The fracture initiation

points were picked as the onset of nonlinearity in his published stress-strain curves and are only approximate.

4.8 Marble

The only marble for which fracture initiation data is available is described by Brace et al. (1966) as a medium grained almost pure calcite marble of unknown origin. They report it to be apparently isotropic, very ductile even at low confining pressures, and having a grain size of about 0.2 mm.

The unusually low fracture initiation stress (Figure 18) requires either large starter flaws (~ 6 mm) or a low fracture toughness. Since Atkinson and Meredith (1987a) report K_{Ic} as low as 0.19 MPa $m^{1/2}$ for calcite, we have fit the initiation data using this value which then implies a starter flaw size of 0.4 mm, which is comparable to the grain size.

In a microscopic study of nucleation in marble, Olsson and Peng (1976) found that microcracks often nucleate where slip bands intersect grain boundaries. Although such slip-bands are physically analogous to angle cracks, there may be a significantly larger number of such nuclei since every favorably aligned grain is a potential source of nuclei. This may explain the large values of initial damage D_0 required to fit the marble data.

The data set which we fit is for Carrara marble which is the fine grained (about 0.1 mm) isotropic marble used by Michaelangelo for the Pieta and other well-known works. Its total porosity is about 1.1% (Edmond and Paterson, 1972). The triaxial data in Figure 18 are from Von Karman (1911) and Edmond and Paterson (1972). Brittle vs ductile behavior was deduced from the shape of the stress-strain curve and from the volume changes associated with the deformation.

4.9 Rock Salt

Rock salt exhibits a room-temperature brittle-to-ductile transition at the lowest confining pressure of any rock in this study. Hunsche (1981) tested three types of natural salt at low confining pressure under both the common triaxial loading and the less common true multiaxial loading at strain rates of about 10^{-6} s^{-1}. Handin (1953) collected conventional triaxial data to higher confining pressures at a strain rate of about 10^{-4} s^{-1}. These data are shown in Figure 19.

5. CONCLUSIONS

1. An approximate physical model for damage evolution in brittle solids under compressive stress states has been developed. The model is based on the growth of wing cracks from a population of small, inclined, starter cracks; and the interaction between them. The important variables of the problem are: the size, 2a, of the initial inclined cracks, and the initial damage

$$D = \frac{4}{3}\pi a^3 N_V$$

The state of the material is measured by the current value of the damage

$$D = \frac{4}{3}\pi (l + \alpha a)^3 N_V$$

where l is the length of the wing cracks.

A number of simplifying assumptions are made in the current model. In particular it is assumed that the population of initial cracks all have the same size. One consequence of this is that the initiation surface (that is , the combination of stresses corresponding to the first extension of the cracks, and thus the first increment of new damage) is linear, described by:

$$\sigma_1 = C_1 \sigma_3 - \sigma_0$$

Similarly, damage itself is a state variable so that surfaces of constant damage in stress space are also linear. The surfaces corresponding to final macroscopic fracture is not one of constant damage (as often assumed) . The terminal damage itself depends on the stress state, but it, too, is well approximated by a linear relationship:

$$\sigma_1 = C_2 \sigma_3 - \sigma_c$$

where σ_c is the simple compressive strength.

The model has been fitted to data for ber of rocks. The process gives physical insight into the damage accumulation and failure of these materials in compression. In particular, the fitting process leads to a value for the coefficient of friction across the crack faces; the size of the initial flaws; and the initial damage D_0 . The failure process depends principally on these variables. Curvature of the failure surface is shown to depend, at least partly, on an interaction between the brittle failure mechanism, and plastic flow. Rocks which show clearly established plasticity at high pressures (marbles, and rock salt, for example) show a brittle regime at low pressures, a transitional regime at intermediate pressures (both depending strongly on pressure), and a regime of plasticity at high pressures which is independent of pressure itself. It is noteworthy that silicate rocks such as granite, gabbro, dunite and aplite show a similar behavior, with the transition to plasticity dominating failure at confining pressures of general order E/30. This transition, at first sight a surprising one, is nonetheless to be expected at such stress levels which are roughly the theoretical shear strength of the minerals within the rock.

Several other noteworthy conclusions emerge. One is that, in rocks which are almost fully dense, the initial flaw size is roughly equal to the grain size of the rock itself. But the initial damage level, D_0 , varies widely. In low porosity crystalline silicates such as granite, this level is low (typically 3%); but in

intrinsically-plastic materials like calcite and rock salt, the initial damage level is high (of order 15%) perhaps because the flaws from which wing cracks grow are slip bands within suitably oriented grains rather than cracks.

3. Data for rocks which are almost fully dense are well fitted by the model. We find, too, that porous rocks (limestone and sandstone, both with roughly 15% porosity) are also well fitted. This suggests that an analogous theoretical development may be possible for porosity induced cracking too.

ACKNOWLEDGEMENT

This work was supported by the United States Airforce DARPA contract #F19628-86-K-0003 .

REFERENCES

Anderson, O.L. and P. Grew, (1976) Stress corrosion theory of crack propagation with applications to geophysics, Rev. Geophys. Space Phys., 15, 77-104.

Ashby, M.F. and S. D. Hallam, (1986), The failure of brittle solids containing small cracks under compressive stress states, Acta metall., 34, 497-510.

Atkinson, B.K. and P.G. Meredith, (1987a), Experimental fracture mechanics data for rocks and minerals, in Fracture Mechanics of Rock, B.K. Atkinson editor, Academic Press, New York, pp 477-525.

Atkinson, B.K. and P.G. Meredith, (1987b), in Fracture Mechanics of Rock, B.K. Atkinson editor, Academic Press, New York, pp 477-525.

Birch, F.,(1960), The velocity of compressional waves in rocks to 10 kilobars, part 1, J. Geophys. Res., 65, 1083-1102.

Brace, W.F., Paulding, B.W., and Scholz, C., (1966), Dilatancy in the fracture of crystalline rocks, J. Geophys. Res., 71, 3939-3953.

Costin, L.S., (1983), A microcrack model for the deformation and failure of brittle rock, J. Geophys. Res., 88, 9485-9492.

Costin, L.S., (1985), Damage mechanics in the post-failure regime, Mechanics of Materials, 4, 149-160.

Costin, L.S. and D.J. Holcomb, (1981), Time-dependent failure of rock under cyclic loading, Tectonophysics, 79, 279-296.

Edmond, J.M., and Paterson, M.S., (1972). Volume changes during the deformation of rocks at high pressures, Int. J. Rock Mech. Min Sci., 9, 161-

Gowd, T.N., and F. Rummel, (1980), Effect of confining pressure on the fracture behavior of a porous rock, Int. J. Rock Mech. Min. Sci. and Geomech. Abstr., 17, 225-229.

Griffith, A.A.,(1924), Theory of rupture , Proc. First International Congress Applied Mechanics, Delft, pp. 55-63.

Griggs, D.T., and J. Handin, (1960), Observations on fracture and a hypothesis of earthquakes. in Rock Mechanics, edited by D.T. Griggs and J. Handin, Geol. Soc. Am., Memoir 79, 347-364.

Hallbauer, D.K., H. Wagner, and N.G.W. Cook, (1973), Some observations concerning the microscopic and mechanical behaviour of quartzite specimens in stiff, triaxial compression tests, Int. J. Rock Mech. Min. Sci., 10, 713-726.

Handin, H., (1953). An application of high pressure in geophysics: experimental rock deformation, Trans. Am Soc. Mech. Engrs., 75, 315-324.

Heard, H.C. (1960). Transition from brittle fracture to ductile flow in Solenhofen limestone as a function of temperature, confining pressure, and interstitial fluid pressure, in Rock Deformation, eds. Griggs, D., and Handin J., Geol. Soc. Am. Memoir, 79, pp193-

Holcomb, D.J., and Costin, L.S., (1986). Damage in brittle materials: experimental methods, in Proceedings of the Tenth U.S. National Congress of Applied Mechanics, edited by Lamb, J.P., 107-113.

Horii, H. and S. Nemat-Nasser, (1985), Compression-Induced Microcrack Growth in Brittle Solids: Axial Splitting and Shear Failure, J. Geophys. Res., 90. 3105-3125.

Horii, H. and S. Nemat-Nasser, (1986), Brittle failure in compression: splitting, faulting and brittle-ductile transition, Phil. Trans. Roy. Soc. A, 319, 337-374.

Hunsche, U., (1984), Fracture experiments on cubic rock salt samples, in Mechanical Behaviour of Salt edited by Hardy, H.R. Jr. and Langer, M., Trans Tech. Publications, Clausthal, Germany, 169-179.

Irwin, G.R., (1958), Fracture, Handbuch der Physik, Vol 6, 551-590, Springer, Berlin.

Jaeger, J.C., and N.G.W. Cook (1976), Fundamentals of Rock Mechanics, 2nd Ed., Chapman and Hall, London.

Janach,W., and Guex, L.H., (1980), In-plane propagation of shear microcracks in brittle rocks under triaxial compression, J. Geophys. Res., 85, 2543-2553.

Kemeny, J., and N.G.W. Cook, (1986), Effective moduli, nonlinear deformation, and strength of a cracked elastic solid, Int. J. Rock Mech. Min. Sci., 23, 107-118.

Knott, J.F.,(1973), Fundamentals of Fracture Mechanics, Butterworths,London.

Martin, R.J., Time-dependent crack growth in quartz and its application to the creep of rocks, J. Geophys. Res., 77, 1406-1419, 1972.

Mogi, K., (1966), Some precise measurements of fracture strength of rocks under uniform compressive stress, Rock Mech. Eng. Geol., 4, 41-55.

Nemat-Nasser, S. and H. Horii, (1982), Compression induced nonplanar crack extension with application to splitting, exfoliation, and rockburst, J. Geophys. Res., 87, 6805.

Newman, (1978)

Olsson, W.A., and S.S. Peng, (1976), Microcrack nucleation in marble, Int. J. Rock Mech. Min. Sci. and Geomech. Abstr., 13, 53-59.

Paterson, M.S., (1978), Experimental Rock Deformation - The Brittle Field, Springer-Verlag, New York.

Rutter, (1972)

Sammis, C.G. and M.F. Ashby, (1986), The failure of brittle porous solids under compressive stress states, Acta metall., 34, 511-526.

Sano, O., I. Ito, and M. Terada, (1981), Influence of strain rate on dilatancy and strength of Oshima granite under uniaxial compression, J. Geophys. Res., 86, 9299-9311.

Schock, R.N., and Heard, H.C., (1974), Static mechanical properties and shock loading response of granite, J. Geophys. Res., 79, 1662-1666.

Scholz, C.H., (1986). A short geophysical history of Westerly granite, preface to Earthquake Source Mechanics, edited by Das, S., Boatwright, J., and Scholz, C.H., Am. Geophys. Union Monograph 37, p ix.

Shimada, M., (1981). The method of compression test under high pressures in a cubic press and the strength of granite, Tectonophysics, 72, 343-357.

Shimada, M., A. Cho and H. Yukutake, (1983), Fracture strength of dry silicate rocks at high confining pressures and activity of acoustic emission, Tectonophysics, 96 , 159-172.

Tada, H., P.C. Paris, and G.R. Irwin, (1985), The Stress Analysis of Cracks Handbook, Del Res., St. Louis, Mo.

Topponnier, P., and W.F. Brace, (1976), Development of stress-induced microcracks in Westerly granite, Int. J. Rock Mech. Min. Sci., 13, 103-112.

Von Karman, T. (1911). Festigkeitswversuche unter allseitgim druck, Z. Ver. Dt. Ing., 55, 1749-1757.

Wawersik, W.R., and C. Fairhurst, (1970), A study of brittle rock failure in laboratory compression experiments, Int. J. Rock Mech. Min. Sci., 7, 561-575.

Wawersik, W.R., and W.F. Brace, (1971), Post-failure behavior of a granite and a diabase, Rock Mech., 3, 61-85.

Waza, T., K. Kurita, and H. Mizutani, (1980), The effect of water on the subcritical crack growth in silicate rocks, Tectonophysics, 67, 25-34

TABLE 1. MATERIAL PROPERTIES OF THE ROCKS AND FITTED MODEL PARAMETERS (Bracketted data are estimates).

MATERIAL(*)	K (GPa) (j)	E (GPa) (j)	Sy (MPa) (k)	Kic (MPam$^{1/2}$) (l)	2a (mm) (n)	Mu (n)	Do (n)	C3 (n)
ECLOGITE (a)	94	130	4000	(1.0)	0.6	0.6	0.08	2.0
DUNITE (b)	130	150	3500	(1.0)	1.0	0.6	0.04	2.0
APLITE (c)	58	-	2300	(1.0)	0.2	0.60	0.08	2.0
GABBRO (d)	60	92	2200	(1.0)	0.8	0.55	0.12	2.0
GRANITE (e)	58	70	2200	1.0	1.0	0.64	0.01	2.0
SANDSTONE (f)	130	130	1000	0.7	2.0	0.60	0.15	2.0
LIMESTONE (g)	70	77	700	0.6	0.05	0.55	0.15	2.0
MARBLE (h)	70	70	350	0.64	0.35	0.6	0.12	2.0
ROCKSALT (i)	37	37	65	0.23	0.5	0.55	0.20	2.0

(a) Eclogite; Shimada et al (1983).
(b) Dunite; Shimada et al (1983).
(c) Aplite; Brace et al (1966).
(d) Gabbro; Shimada et al (1983).
(e) Westerly Granite; Brace et al (1966), Mogi (1966) and Holcomb and Costin (1986).
(f) Medium-grained Buntsandstone; Gowd and Rummel (1980).
(g) Solenhofen Limestone; Heard (1960).
(h) Carrara Marble; Von Karman (1911) and Edmond and Paterson (1972).
(i) Rocksalt; Handin (1953) and Hunsche (1981).
(j) Bulk modulus K and Young's modulus E from Birch (1966).
(k) Derived from data plotted in figures 11 to 24.
(l) Atkinson and Meredith (1987). The lowest published value was chosen in each case.
(n) Obtained by fitting the data of Figs 11 to 24 to the equations of the text.
(*) We assume α = 0.7 and β = 0.45 for all materials.

FIGURE CAPTIONS

Figure 1. Compressive failure of a brittle solid containing a distribution of flaws.

Figure 2. Cracks can initiate at inclined flaws and at holes. In both cases there are two contributions to K_I, the opening stress intensity at the tip of the growing wing cracks. One is caused by the stress concentrations at the flaw; the other is due to the closing effect of σ_3.

Figure 3. Data for crack initiation in Westerly granite. Crack initiation data for several other rocks are analyzed in section 4. In all cases the data are well fitted by equation (1) with a coefficient of friction between 0.55 and 0.65.

Figure 4. A population of growing cracks. We first analyze the growth of an isolated crack (shown above) and then include the crack-crack interaction (illustrated on the right).

Figure 5. A comparison of the approximate equation (8b) with the numerical calculations of Nemat-Nasser and Horii (1982). The approximation is adequate for the present purposes.

Figure 6. The dependence of axial stress on damage as predicted by equations (16) and (17). The peak stress is marked. We take this as the failure stress.

Figure 7. The peak value of σ_1 plotted against σ_3 to show the failure surface. In the present formulation, damage is a state variable.

Figure 8. Wing cracks growing from an initial, constrained, penny-shaped flaw. The geometry is more complicated than in the 2-dimensional case but the same method can be used to give an approximate solution for K_I at the tips of the wing cracks.

Figure 9. The dependence of axial stress on damage as predicted by equations (27) and (28). The peak stress is marked. We take this as the failure stress.

Figure 10. The peak value of σ_1 plotted against σ_3 to show the failure surface. In this formulation, damage is a state variable.

Figure 11. Comparison between experimental and theoretical failure surfaces for granite. Data and theory for microfracture initiation and surfaces of constant damage are also compared. The yield surface (eqn. 30) is also plotted as the heavy broken lines. Part (a) is limited to low and intermediate confining stress; part (b) extends to the largest measured confining stress.

Figure 12. Comparison between experimental and theoretical failure surfaces for aplite. The heavy solid line is the theoretical failure surface. The light solid line is the surface for the initiation of microfracturing while the light broken lines are surfaces of

constant damage. The heavy broken line is the yield surface (eqn. 30). Part (a) is limited to low and intermediate confining stress; part (b) extends to the largest measured confining stress.

Figure 13. Comparison between experimental and theoretical failure surfaces for dunite. The heavy solid line is the theoretical failure surface. The light solid line is the surface for the initiation of microfracturing while the light broken lines are surfaces of constant damage. The heavy broken line is the yield surface (eqn. 30).

Figure 14. Comparison between experimental and theoretical failure surfaces for eclogite. The heavy solid line is the theoretical failure surface. The light solid line is the surface for the initiation of microfracturing while the light broken lines are surfaces of constant damage. The heavy broken line is the yield surface (eqn. 30).

Figure 15. Comparison between experimental and theoretical failure surfaces for gabbro. The heavy solid line is the theoretical failure surface. The light solid line is the surface for the initiation of microfracturing while the light broken lines are surfaces of constant damage. The heavy broken line is the yield surface (eqn. 30).

Figure 16. Comparison between experimental and theoretical failure surfaces for sandstone. The heavy solid line is the theoretical failure surface. The light solid line is the surface for the initiation of microfracturing while the light broken lines are surfaces of constant damage. The heavy broken line is the yield surface (eqn. 30).

Figure 17. Comparison between experimental and theoretical failure surfaces for limestone. The heavy solid line is the theoretical failure surface. The light solid line is the surface for the initiation of microfracturing while the light broken lines are surfaces of constant damage. The heavy broken line is the yield surface (eqn. 30).

Figure 18. Comparison between experimental and theoretical failure surfaces for marble. The heavy solid line is the theoretical failure surface. The light solid line is the surface for the initiation of microfracturing while the light broken lines are surfaces of constant damage. The heavy broken line is the yield surface (eqn. 30). Parts (a) and (b) are limited to low and intermediate confining stress; part (c) extends to the largest measured confining stress.

Figure 19. Comparison between experimental and theoretical failure surfaces for rock salt. The heavy solid line is the theoretical failure surface. The light solid line is the surface for the initiation of microfracturing while the light broken lines are surfaces of constant damage. The heavy broken line is the yield surface (eqn. 30). Part (a) is limited to low and intermediate confining stress; part (b) extends to the largest measured confining stress.

Figure 20. Comparison between experimental and theoretical failure surfaces for marble at low and intermediate confining stress. The heavy solid line is the theoretical failure surface. The light solid line is the surface for the initiation of microfracturing while the light broken lines are surfaces of constant damage. The heavy broken line is the yield surface (eqn. 30).

Figure 21. Comparison between experimental and theoretical failure surfaces for marble at low and intermediate confining stress. The heavy solid line is the theoretical failure surface. The light solid line is the surface for the initiation of microfracturing while the light broken lines are surfaces of constant damage. The heavy broken line is the yield surface (eqn. 30).

Figure 22. Comparison between experimental and theoretical failure surfaces for marble extended to the highest measured confining stress. The heavy solid line is the theoretical failure surface. The light solid line is the surface for the initiation of microfracturing while the light broken lines are surfaces of constant damage. The heavy broken line is the yield surface (eqn. 30).

Figure 23. Comparison between experimental and theoretical failure surfaces for rock salt at low and intermediate confining stress. The heavy solid line is the theoretical failure surface. The light solid line is the surface for the initiation of microfracturing while the light broken lines are surfaces of constant damage. The heavy broken line is the yield surface (eqn. 30).

Figure 24. Comparison between experimental and theoretical failure surfaces for rock salt extended to the largest confining stress. The heavy solid line is the theoretical failure surface. The light solid line is the surface for the initiation of microfracturing while the light broken lines are surfaces of constant damage. The heavy broken line is the yield surface (eqn. 30).

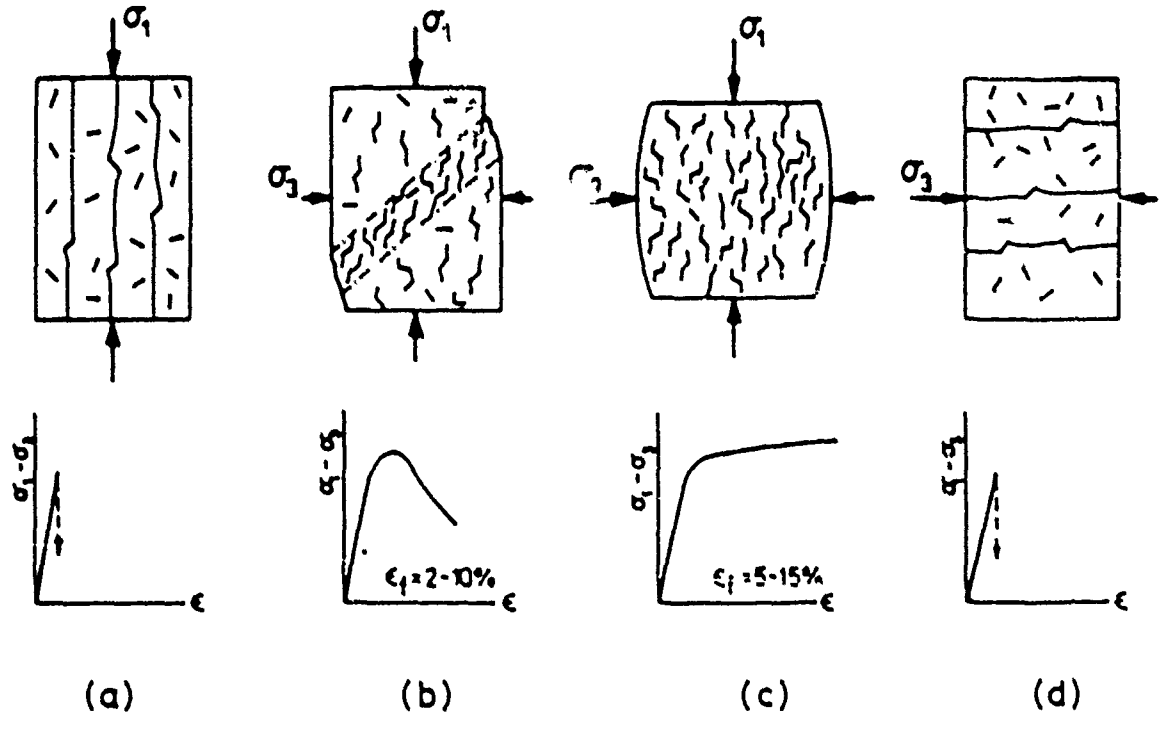

Figure 1. Compressive failure of a brittle solid containing a distribution of flaws.

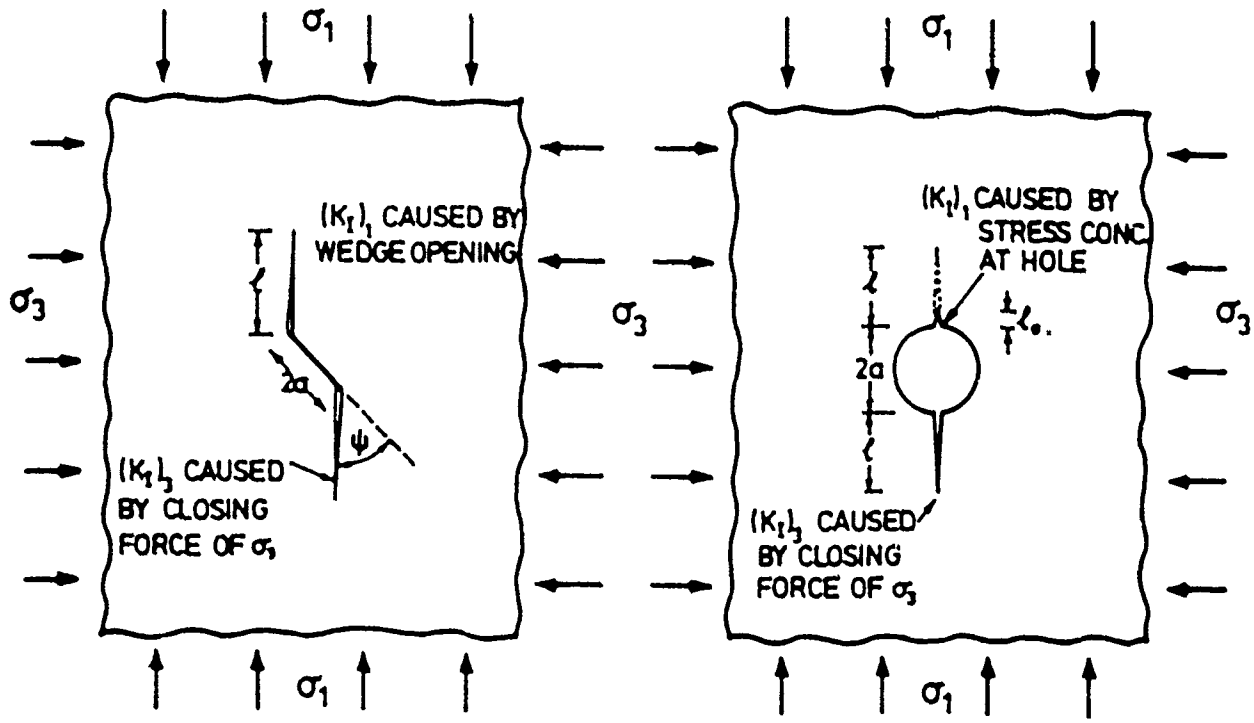

Figure 2. Cracks can initiate at inclined flaws and at holes. In both cases there are two contributions to K_I, the opening stress intensity at the tip of the growing wing cracks. One is caused by the stress concentrations at the flaw; the other is due to the closing effect of σ_3.

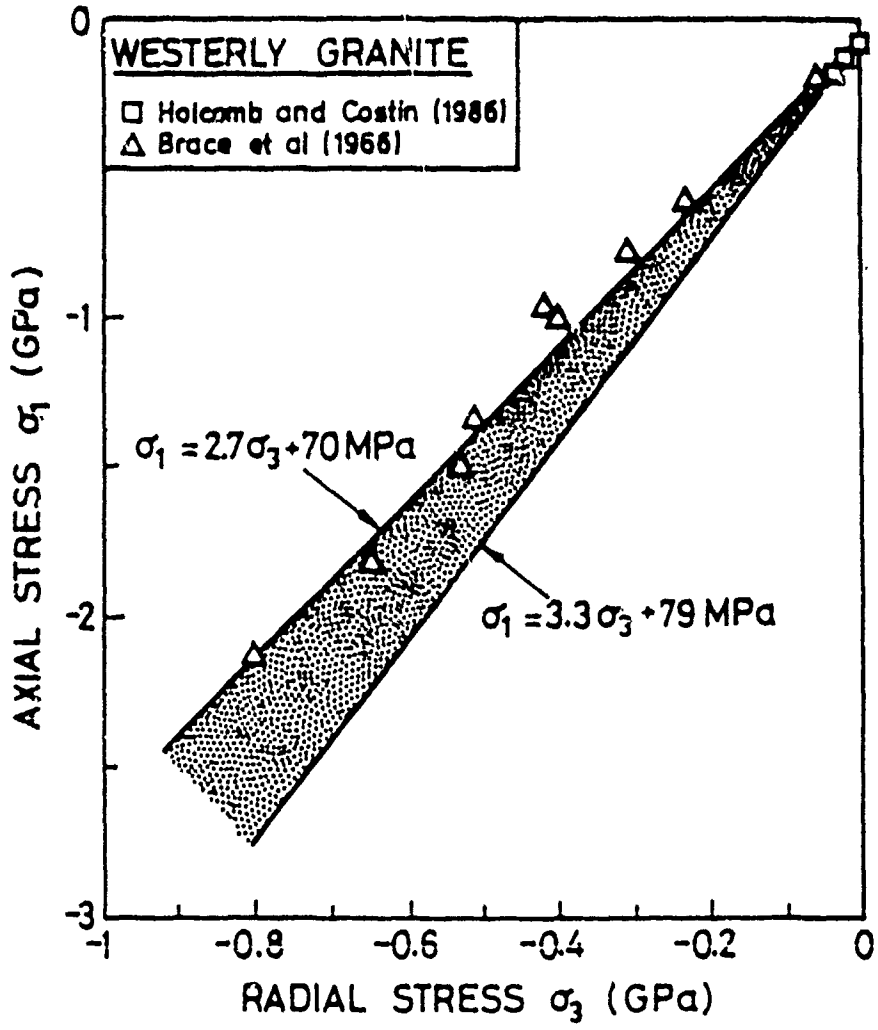

Figure 3. Data for crack initiation in Westerly granite. Crack initiation data for several other rocks are analyzed in section 4. In all cases the data are well fitted by equation (1) with a coefficient of friction between 0.55 and 0.65.

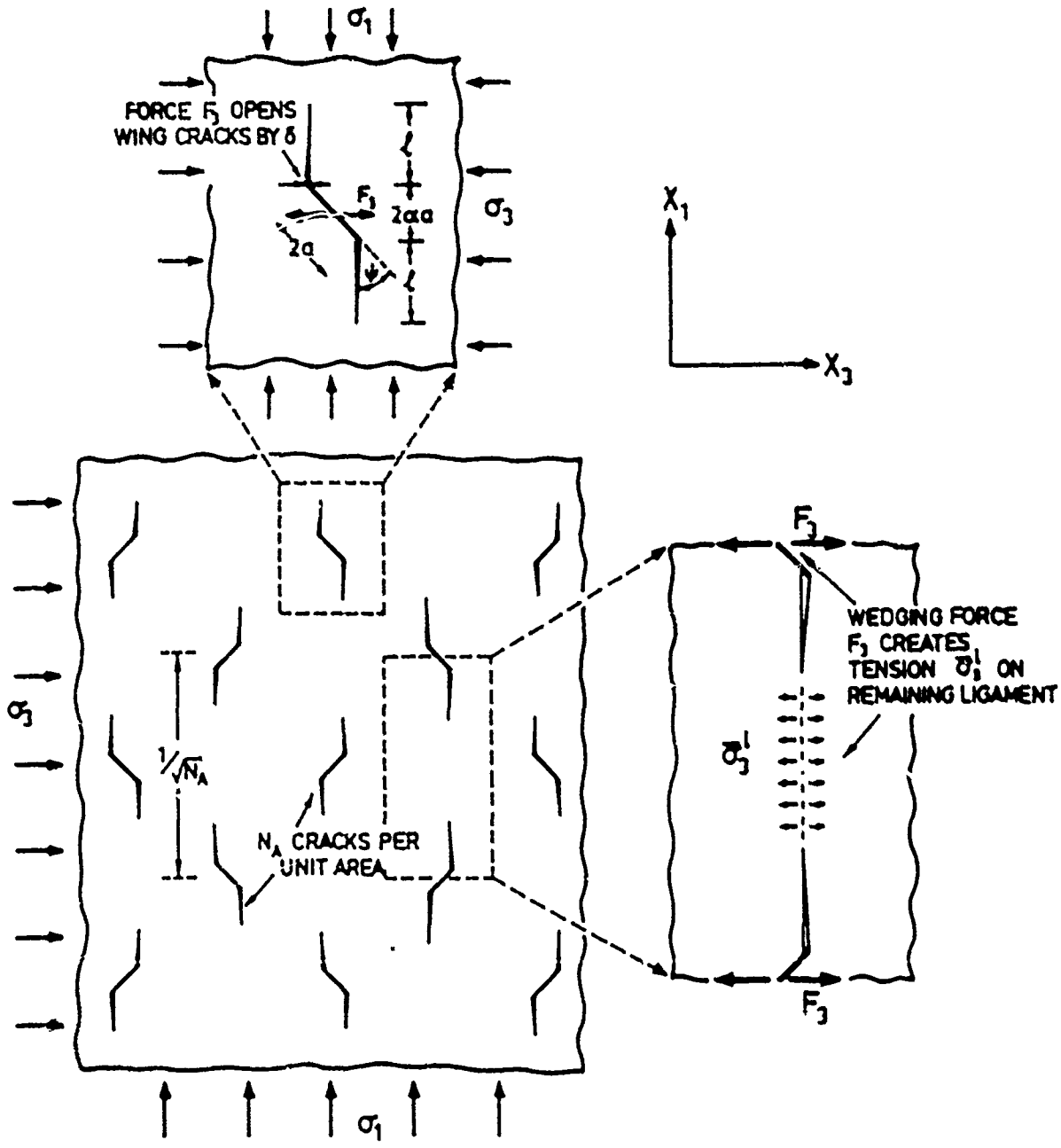

Figure 4. A population of growing cracks. We first analyze the growth of an isolated crack (shown above) and then include the crack-crack interaction (illustrated on the right).

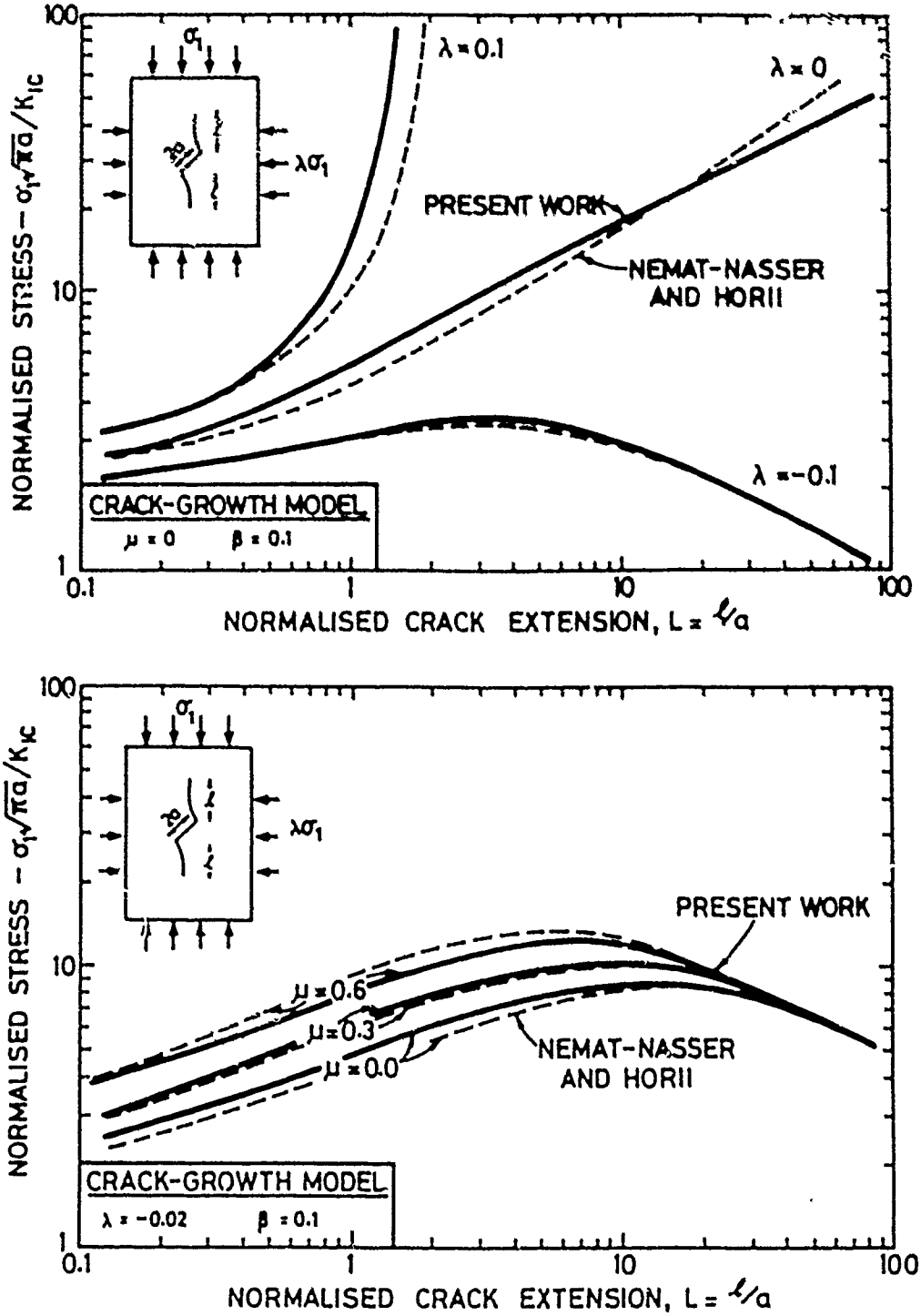

Figure 5. A comparison of the approximate equation (8b) with the numerical calculations of Nemat-Nasser and Horii (1982). The approximation is adequate for the present purposes.

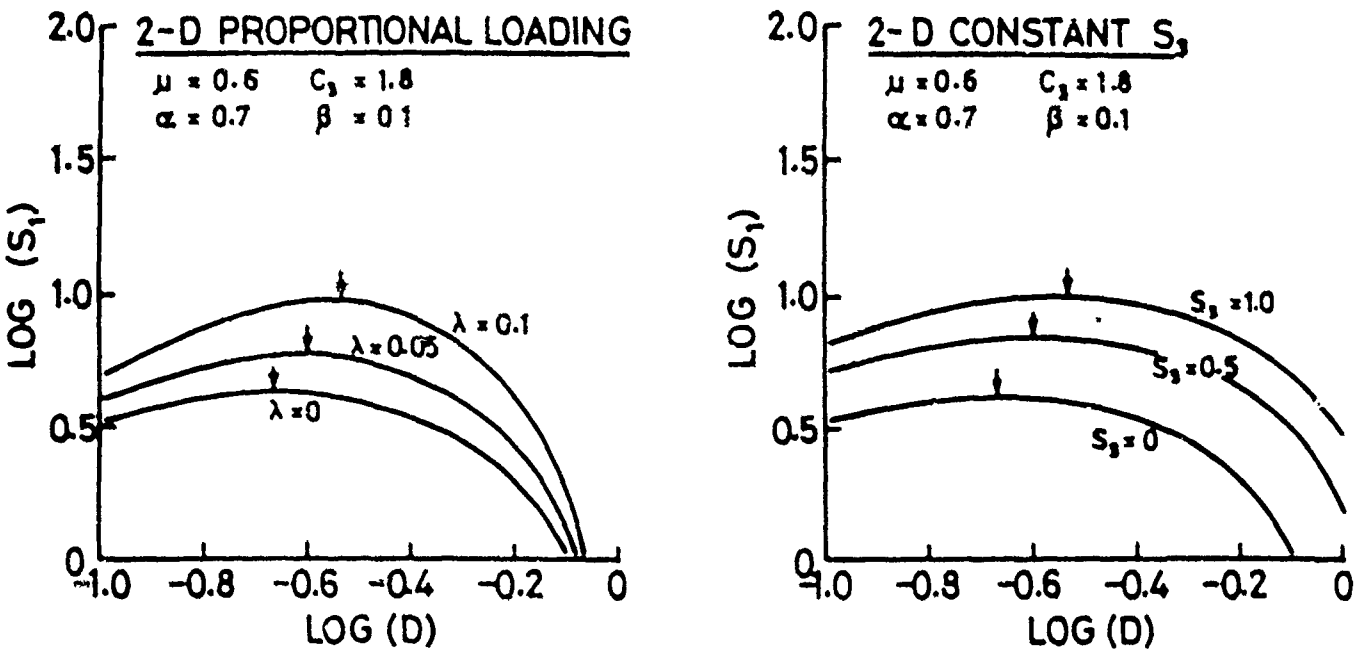

Figure 6. The dependence of axial stress on damage as predicted by equations (16) and (17). The peak stress is marked. We take this as the failure stress.

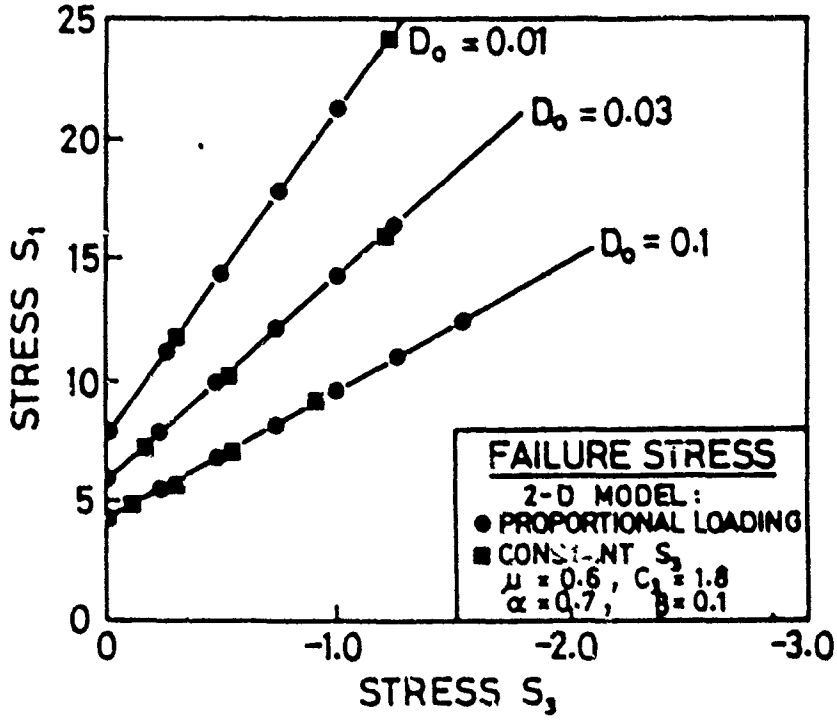

Figure 7. The peak value of σ_1 plotted against σ_3 to show the failure surface. In the present formulation, damage is a state variable.

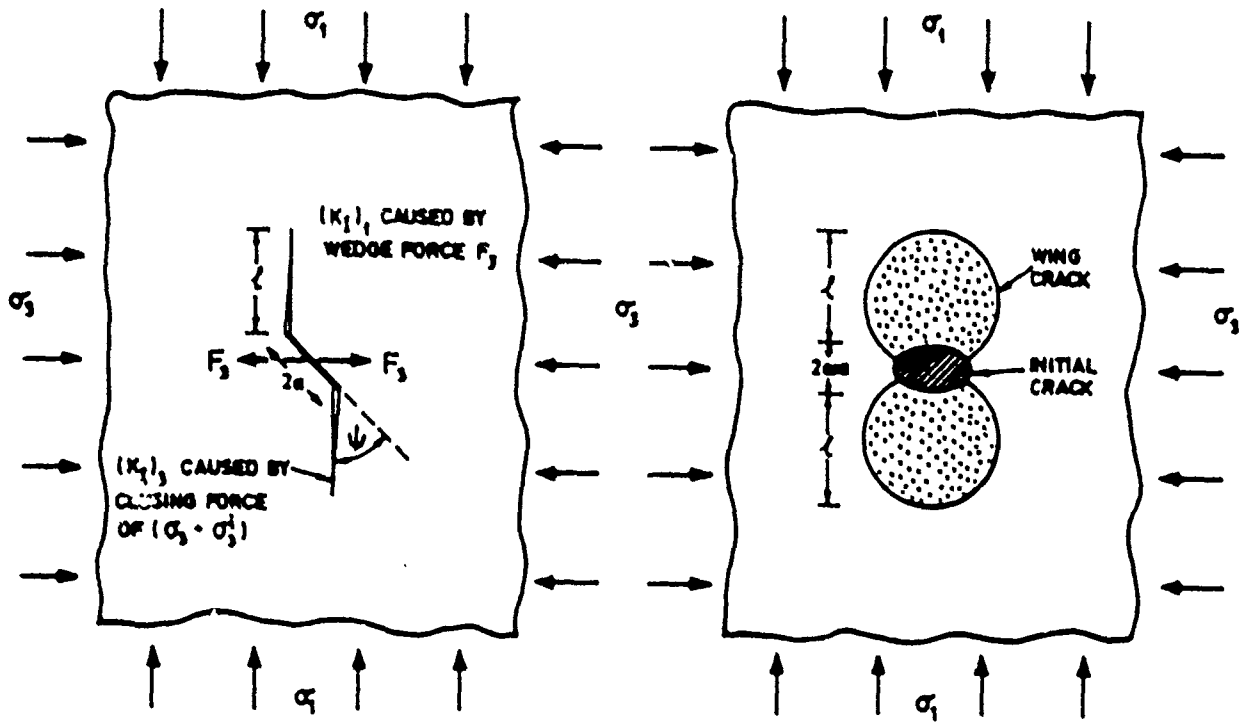

Figure 8. Wing cracks growing from an initial, constrained, penny-shaped flaw. The geometry is more complicated than in the 2-dimensional case but the same method can be used to give an approximate solution for K_I at the tips of the wing cracks.

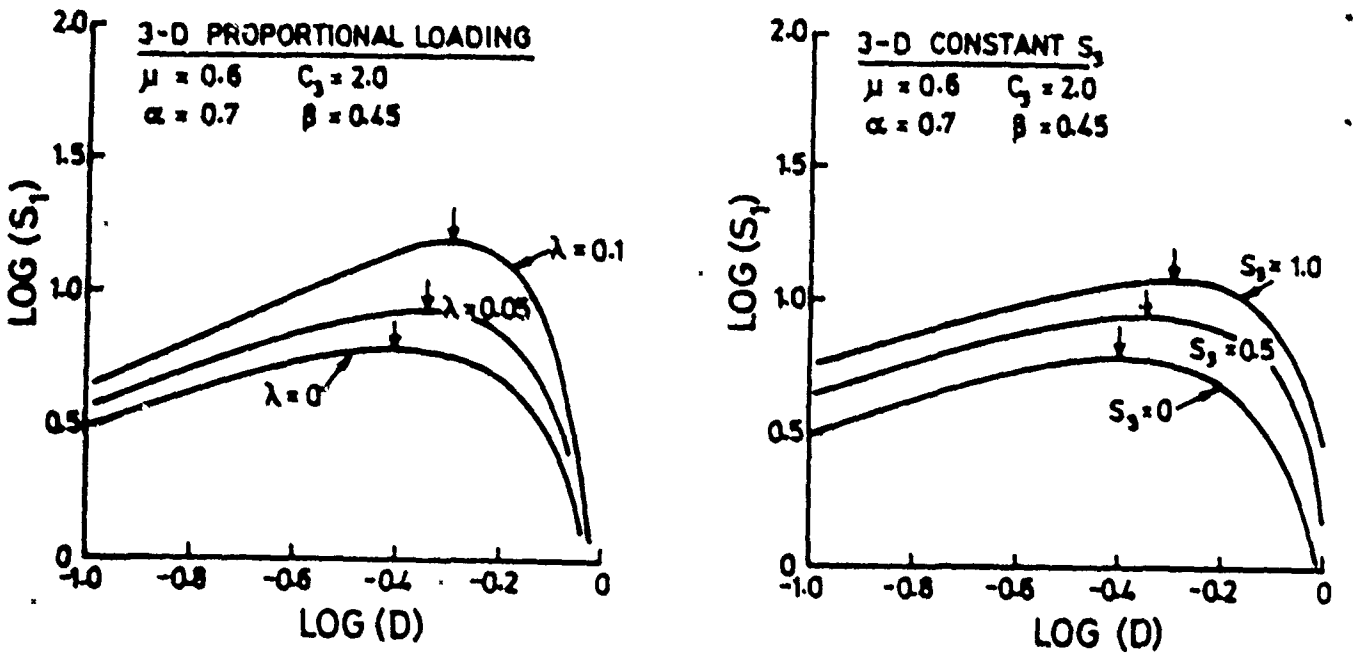

Figure 9. The dependence of axial stress on damage as predicted by equations (27) and (28). The peak stress is marked. We take this as the failure stress.

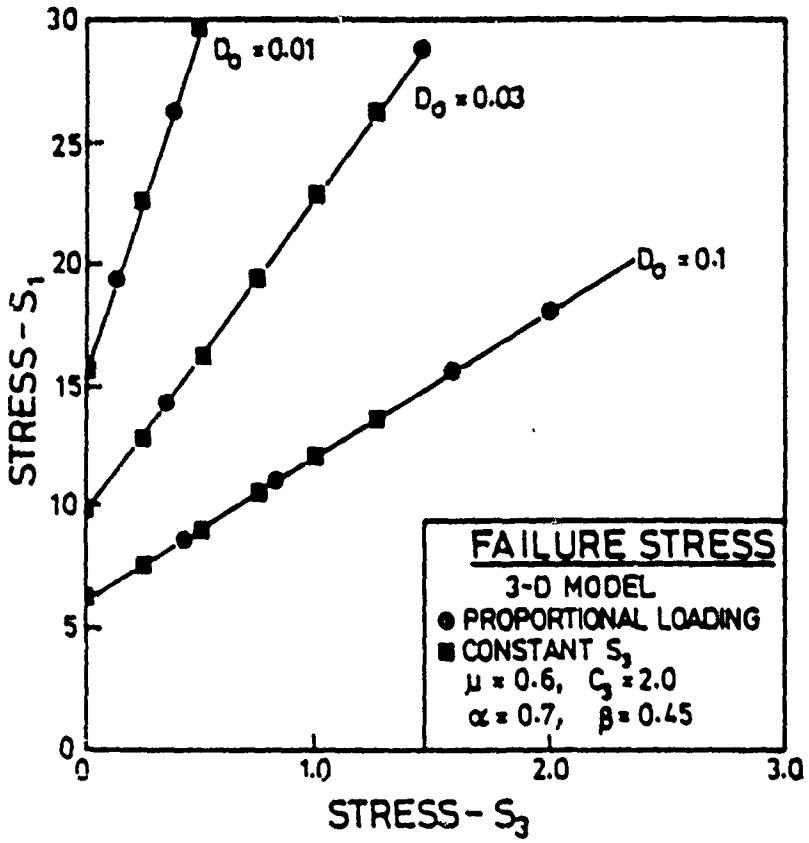

Figure 10. The peak value of σ_1 plotted against σ_3 to show the failure surface. In this formulation, damage is a state variable.

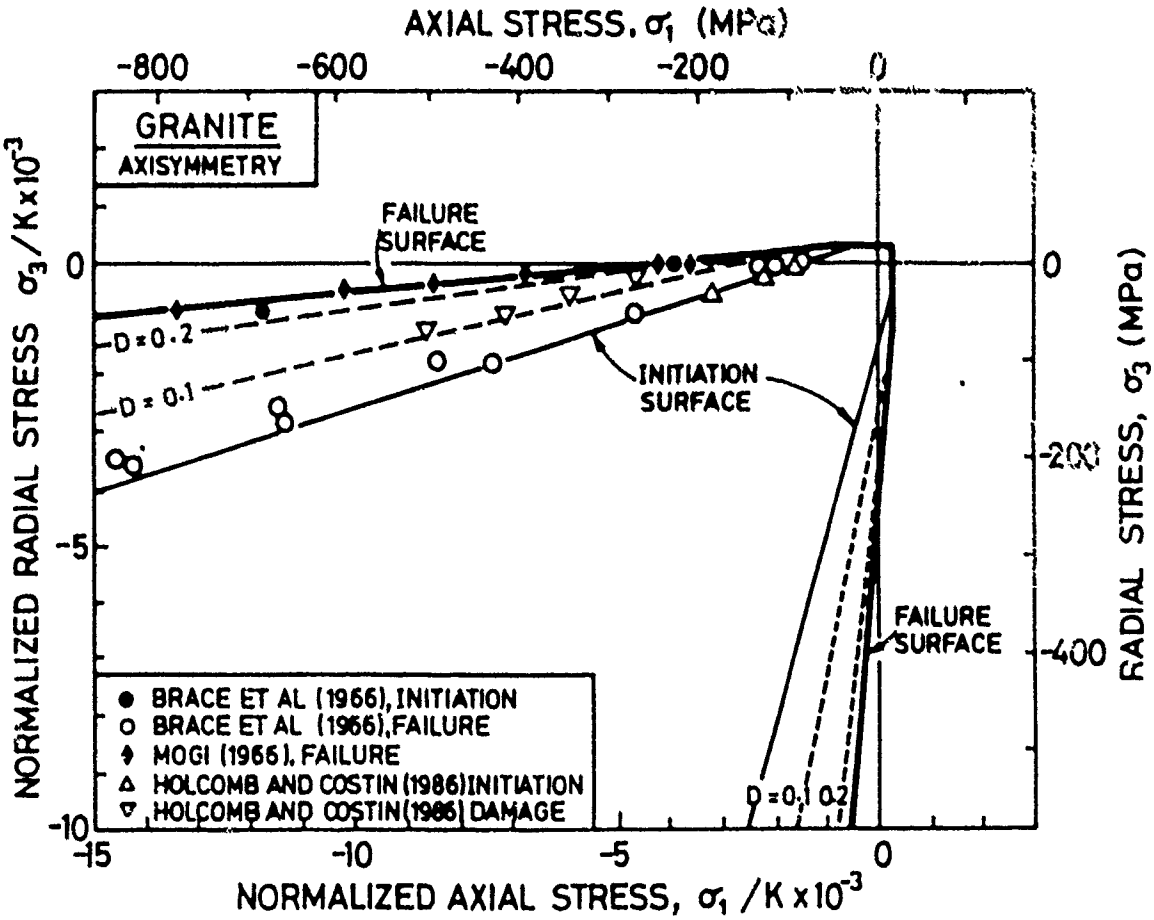

Figure 11. Comparison between experimental and theoretical failure surfaces for granite at low and intermediate confining stress. Data and theory for microfracture initiation and surfaces of constant damage are also compared. The yield surface (eqn. 30) is also plotted as the heavy broken lines.

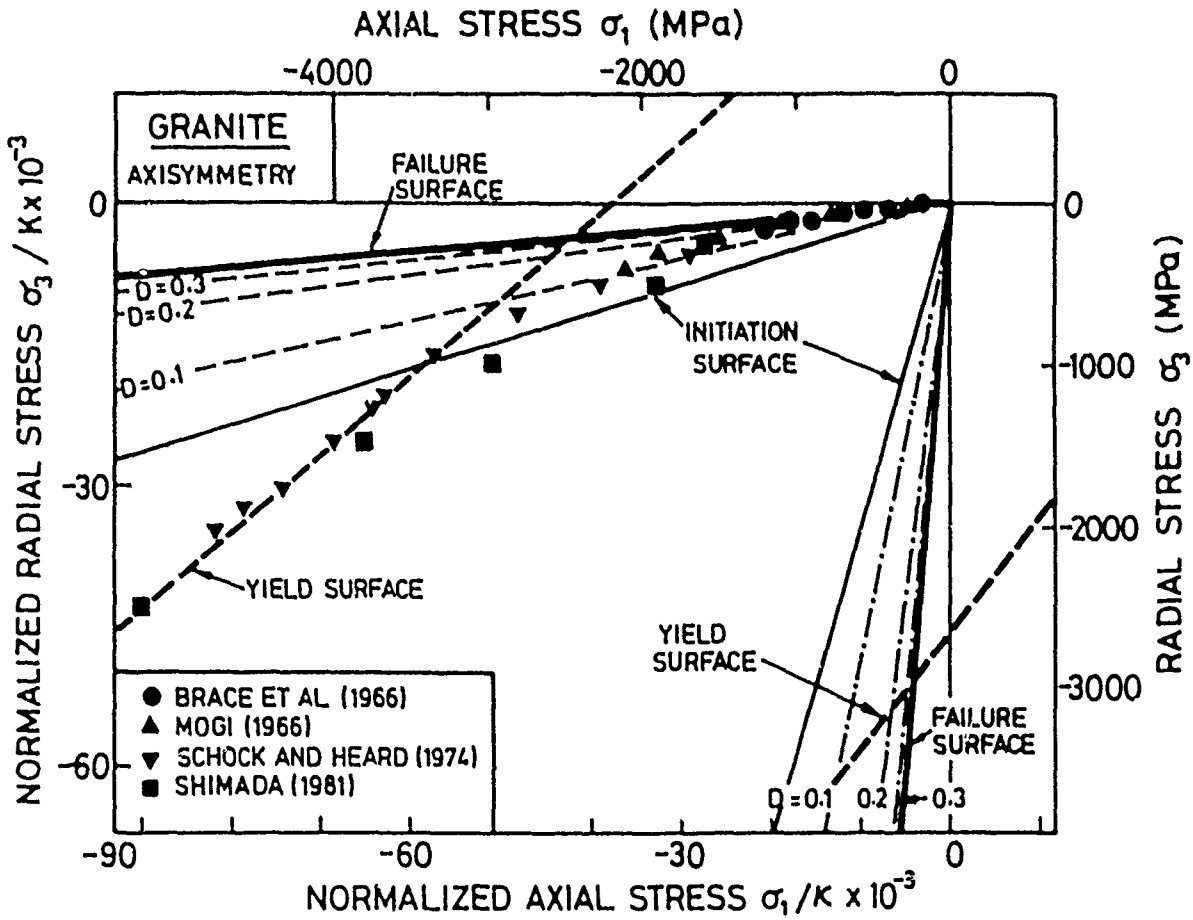

Figure 12. Comparison between experimental and theoretical failure surfaces for granite extended to the largest measured confining stress. Data and theory for microfracture initiation and surfaces of constant damage are also compared. The yield surface (eqn. 30) is also plotted as the heavy broken lines.

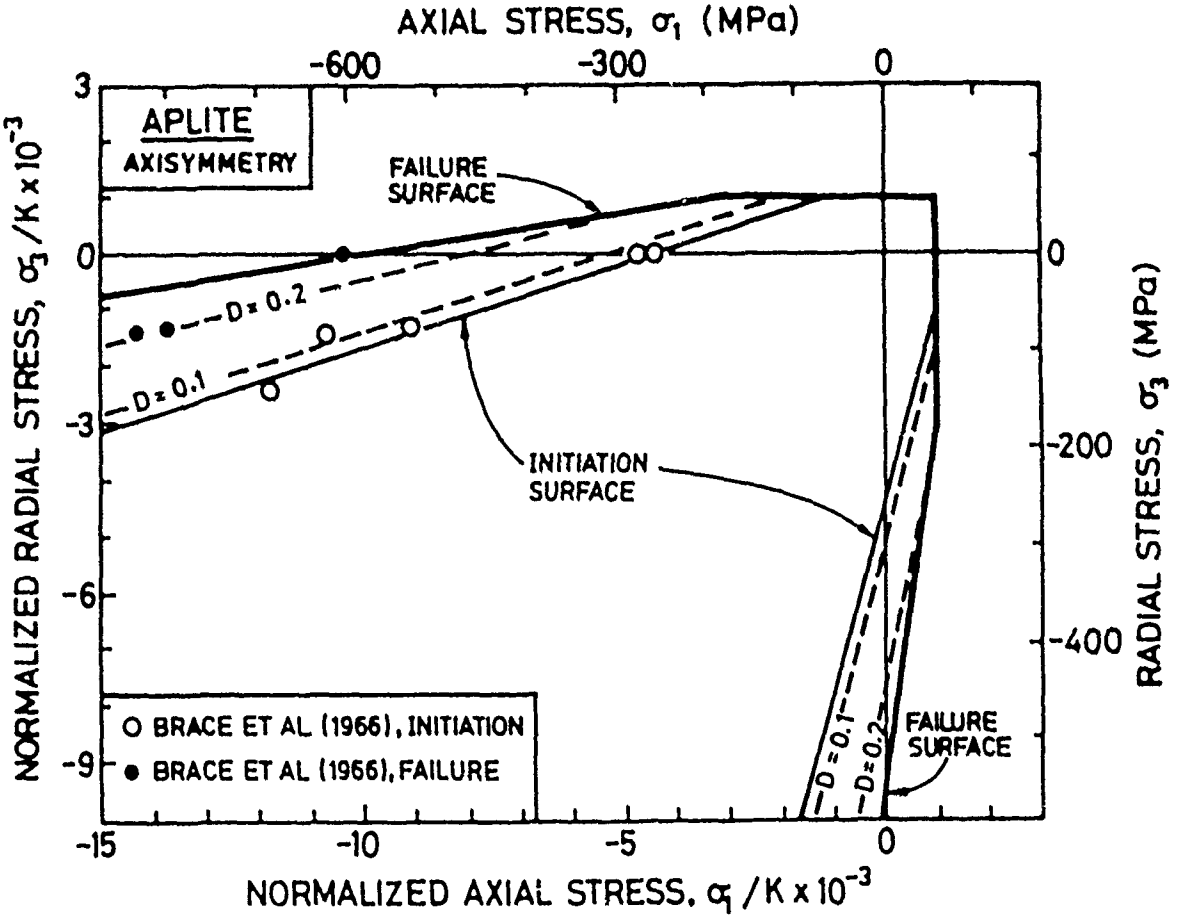

Figure 13. Comparison between experimental and theoretical failure surfaces for aplite at low and intermediate confining stress. The heavy solid line is the theoretical failure surface. The light solid line is the surface for the initiation of microfracturing while the light broken lines are surfaces of constant damage. The heavy broken line is the yield surface (eqn. 30).

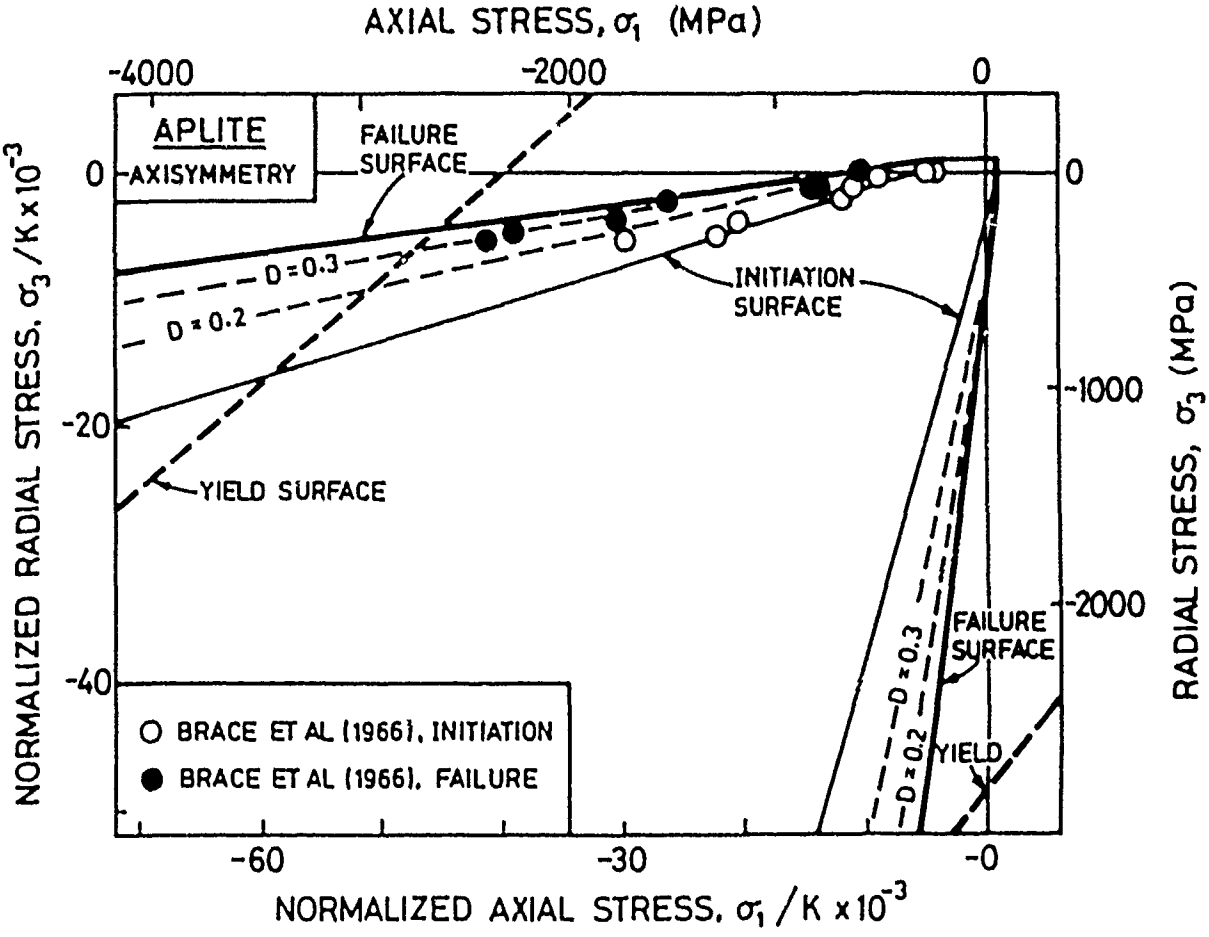

Figure 14. Comparison between experimental and theoretical failure surfaces for aplite extended to the largest measured confining stress. The heavy solid line is the theoretical failure surface. The light solid line is the surface for the initiation of microfracturing while the light broken lines are surfaces of constant damage. The heavy broken line is the yield surface (eqn. 30).

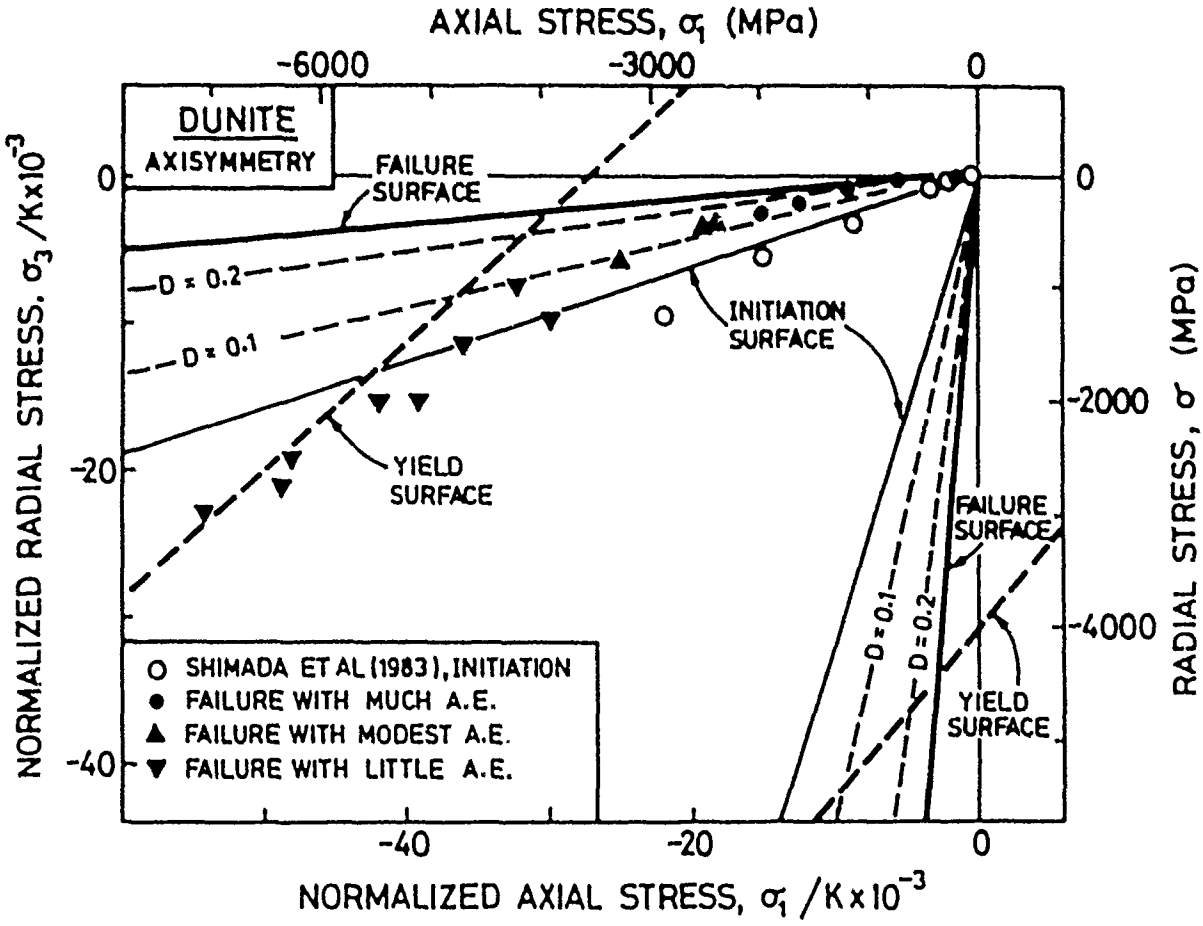

Figure 15. Comparison between experimental and theoretical failure surfaces for dunite. The heavy solid line is the theoretical failure surface. The light solid line is the surface for the initiation of microfracturing while the light broken lines are surfaces of constant damage. The heavy broken line is the yield surface (eqn. 30).

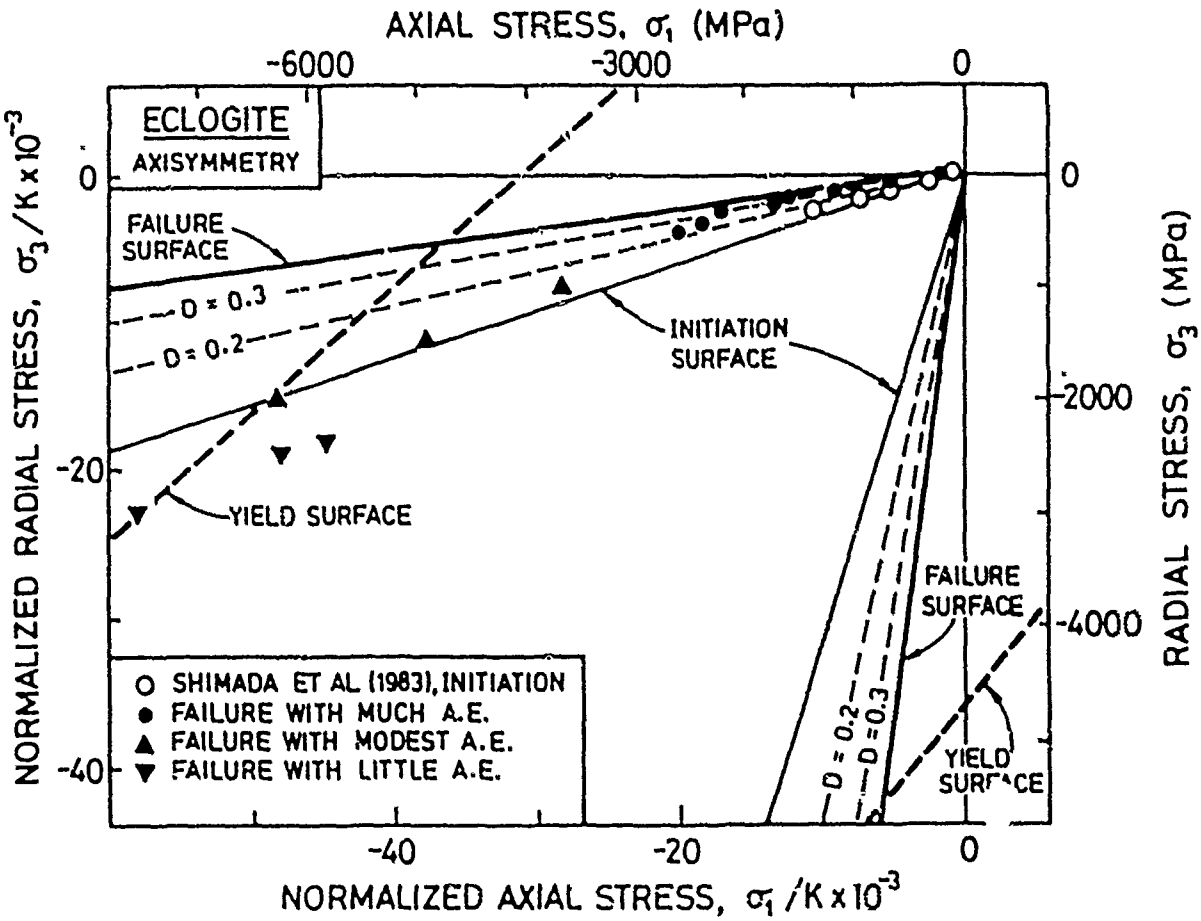

Figure 16. Comparison between experimental and theoretical failure surfaces for eclogite. The heavy solid line is the theoretical failure surface. The light solid line is the surface for the initiation of microfracturing while the light broken lines are surfaces of constant damage. The heavy broken line is the yield surface (eqn. 30).

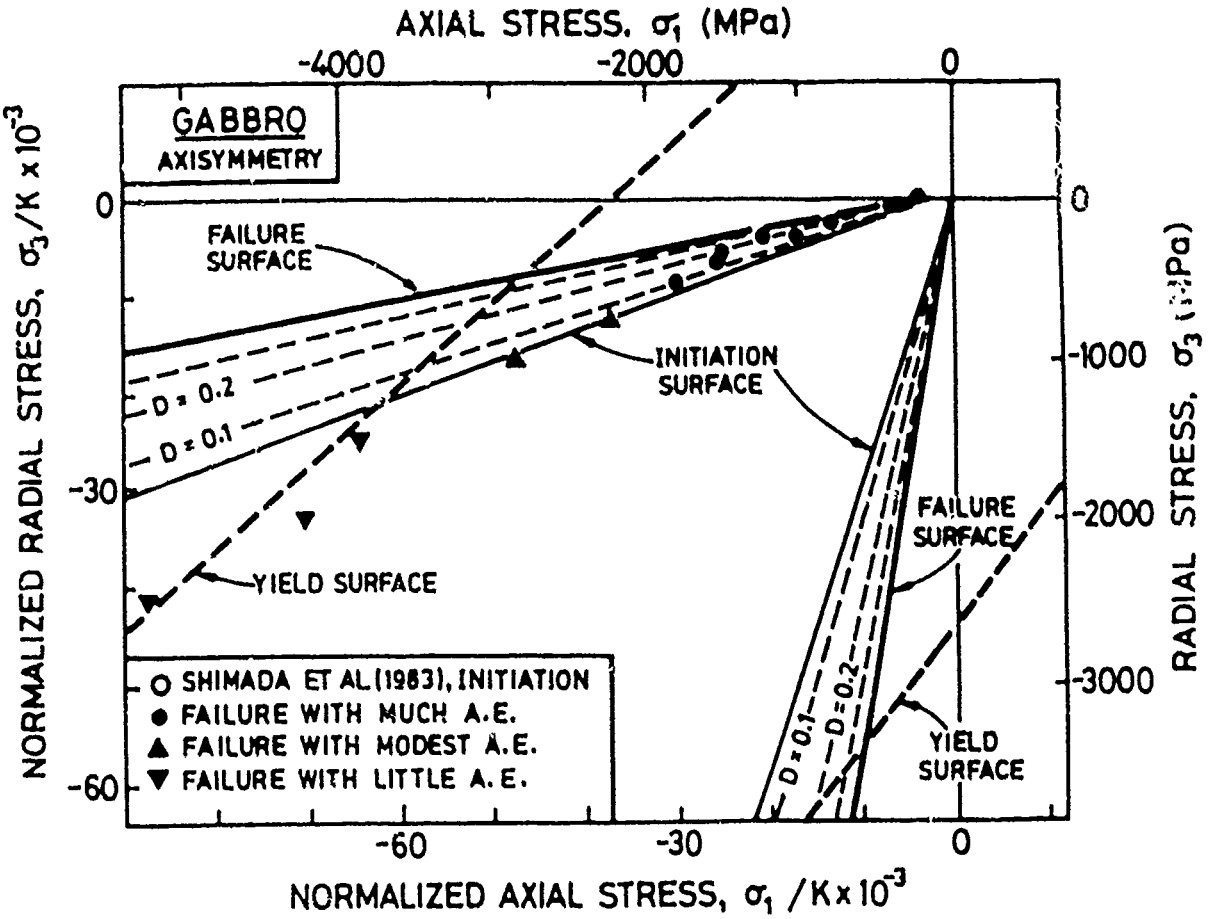

Figure 17. Comparison between experimental and theoretical failure surfaces for gabbro. The heavy solid line is the theoretical failure surface. The light solid line is the surface for the initiation of microfracturing while the light broken lines are surfaces of constant damage. The heavy broken line is the yield surface (eqn. 30).

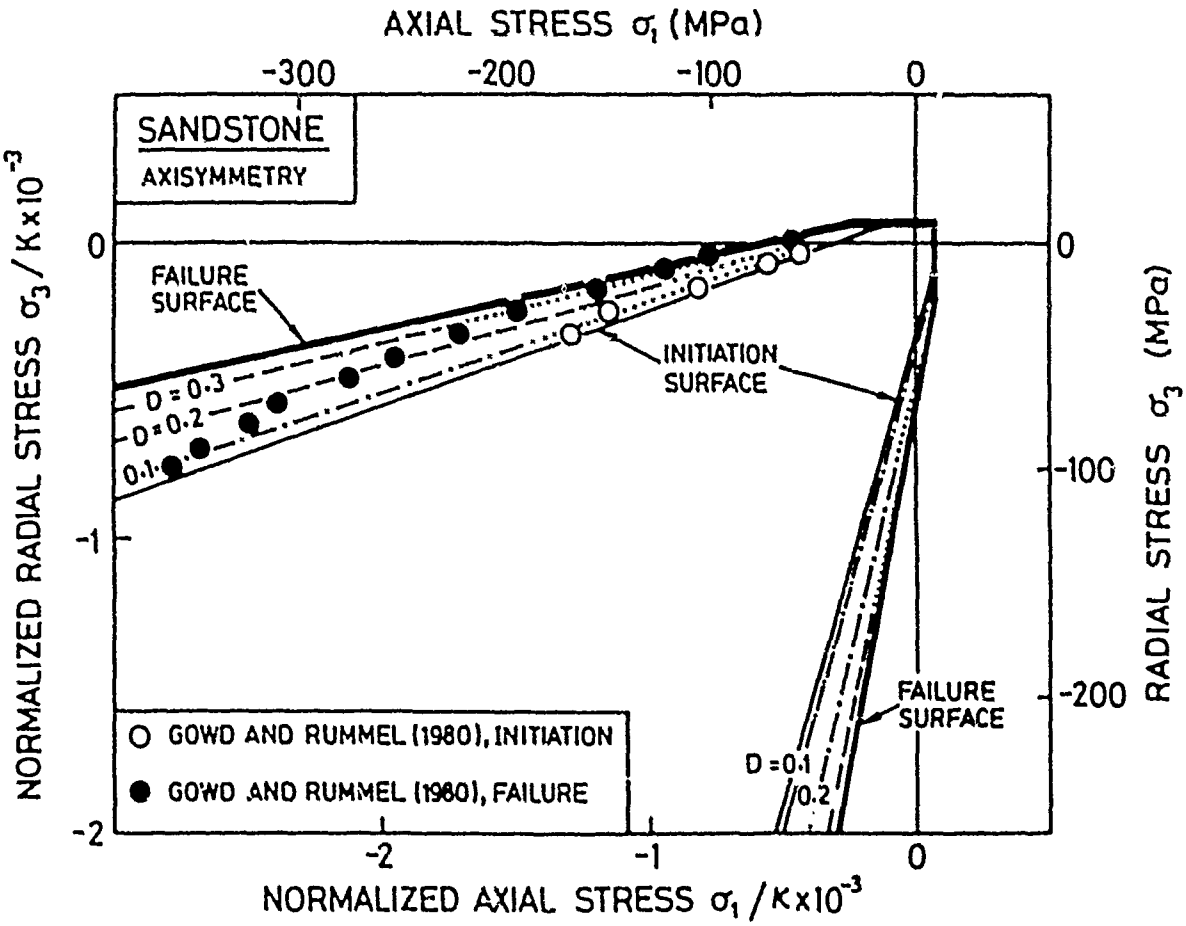

Figure 18. Comparison between experimental and theoretical failure surfaces for sandstone. The heavy solid line is the theoretical failure surface. The light solid line is the surface for the initiation of microfracturing while the light broken lines are surfaces of constant damage. The heavy broken line is the yield surface (eqn. 30).

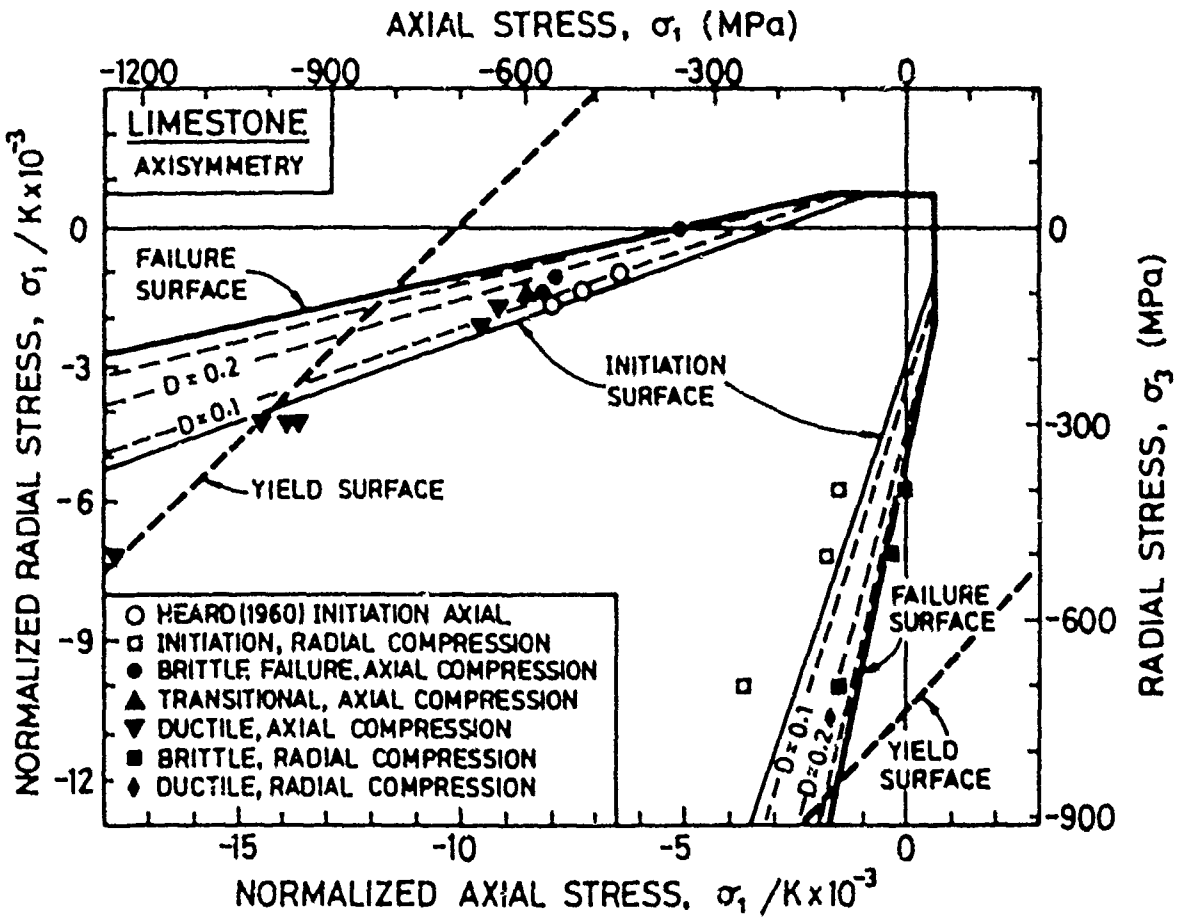

Figure 19. Comparison between experimental and theoretical failure surfaces for limestone. The heavy solid line is the theoretical failure surface. The light solid line is the surface for the initiation of microfracturing while the light broken lines are surfaces of constant damage. The heavy broken line is the yield surface (eqn. 30).

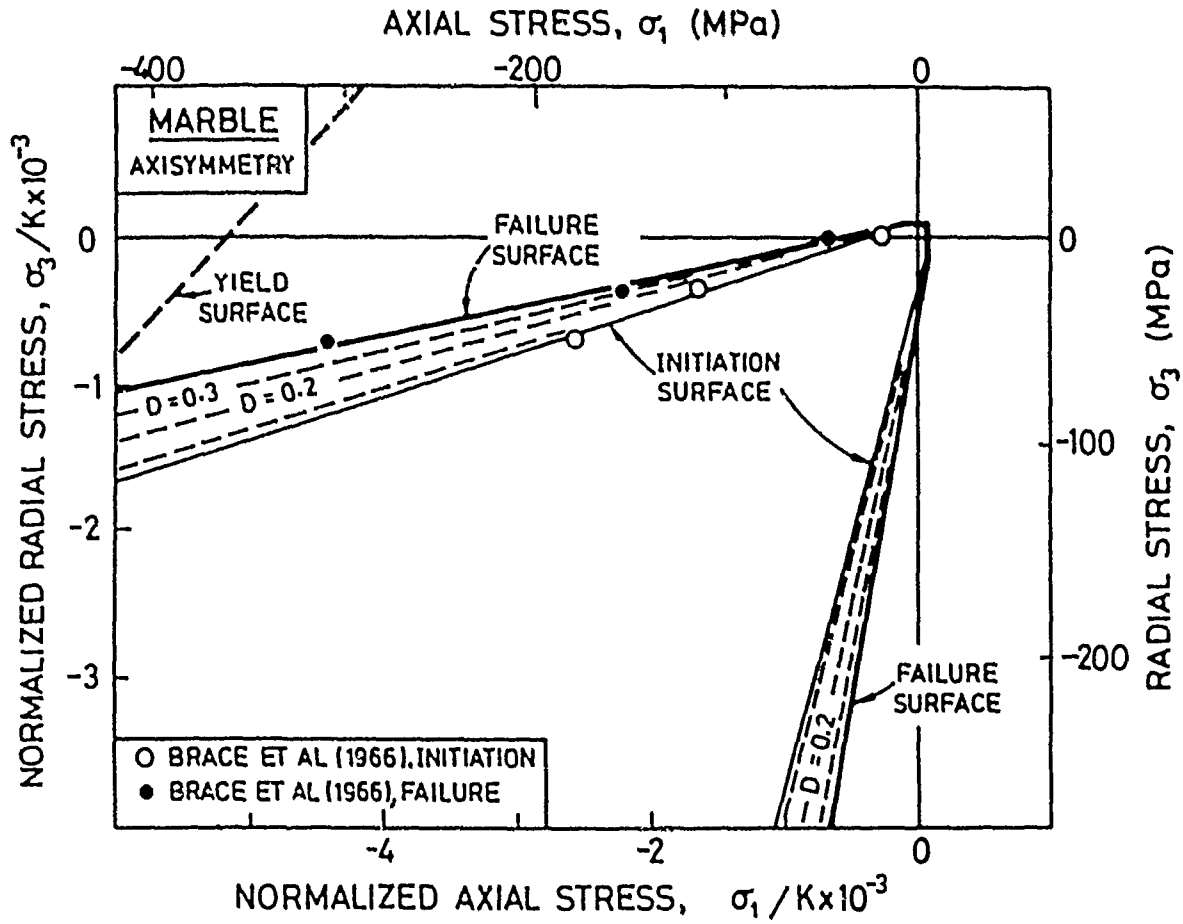

Figure 20. Comparison between experimental and theoretical failure surfaces for marble at low and intermediate confining stress. The heavy solid line is the theoretical failure surface. The light solid line is the surface for the initiation of microfracturing while the light broken lines are surfaces of constant damage. The heavy broken line is the yield surface (eqn. 30).

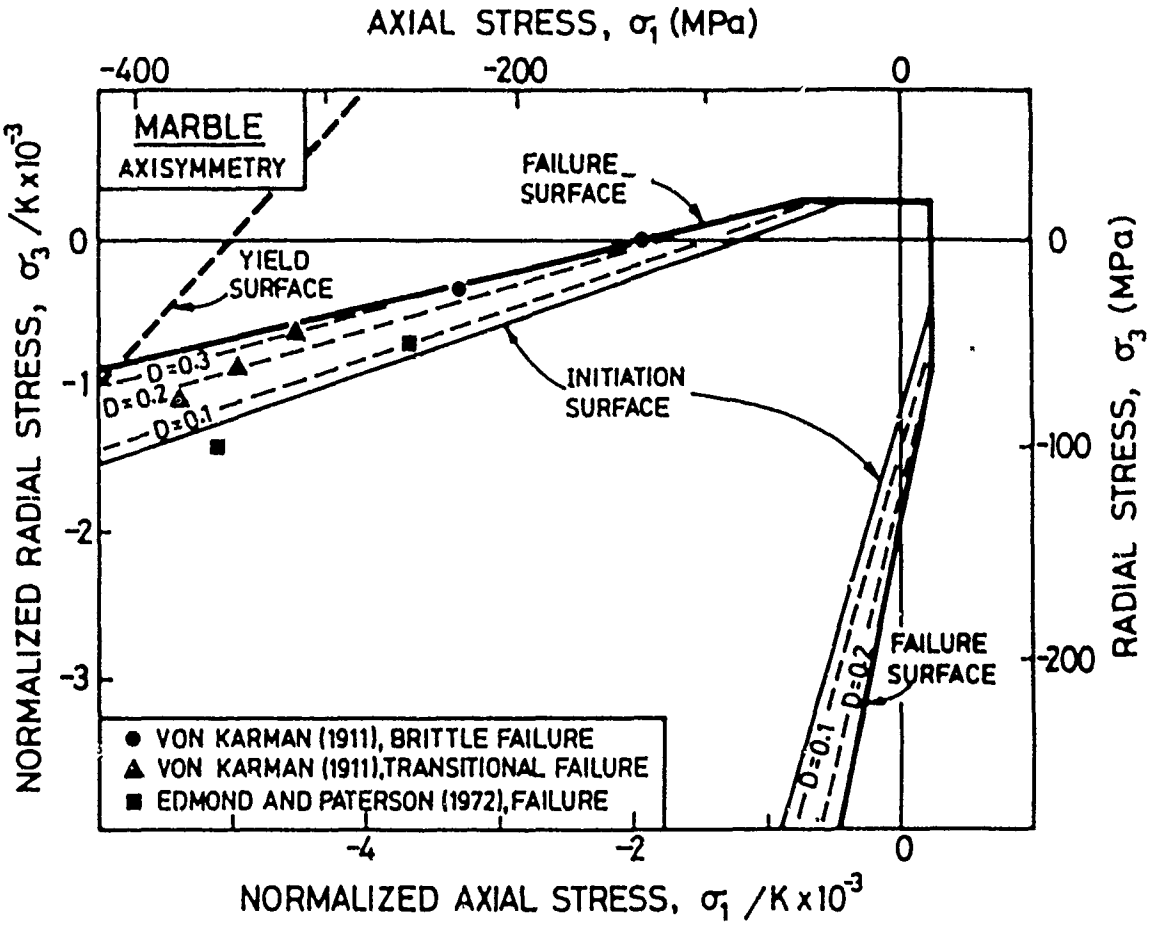

Figure 21. Comparison between experimental and theoretical failure surfaces for marble at low and intermediate confining stress. The heavy solid line is the theoretical failure surface. The light solid line is the surface for the initiation of microfracturing while the light broken lines are surfaces of constant damage. The heavy broken line is the yield surface (eqn. 30).

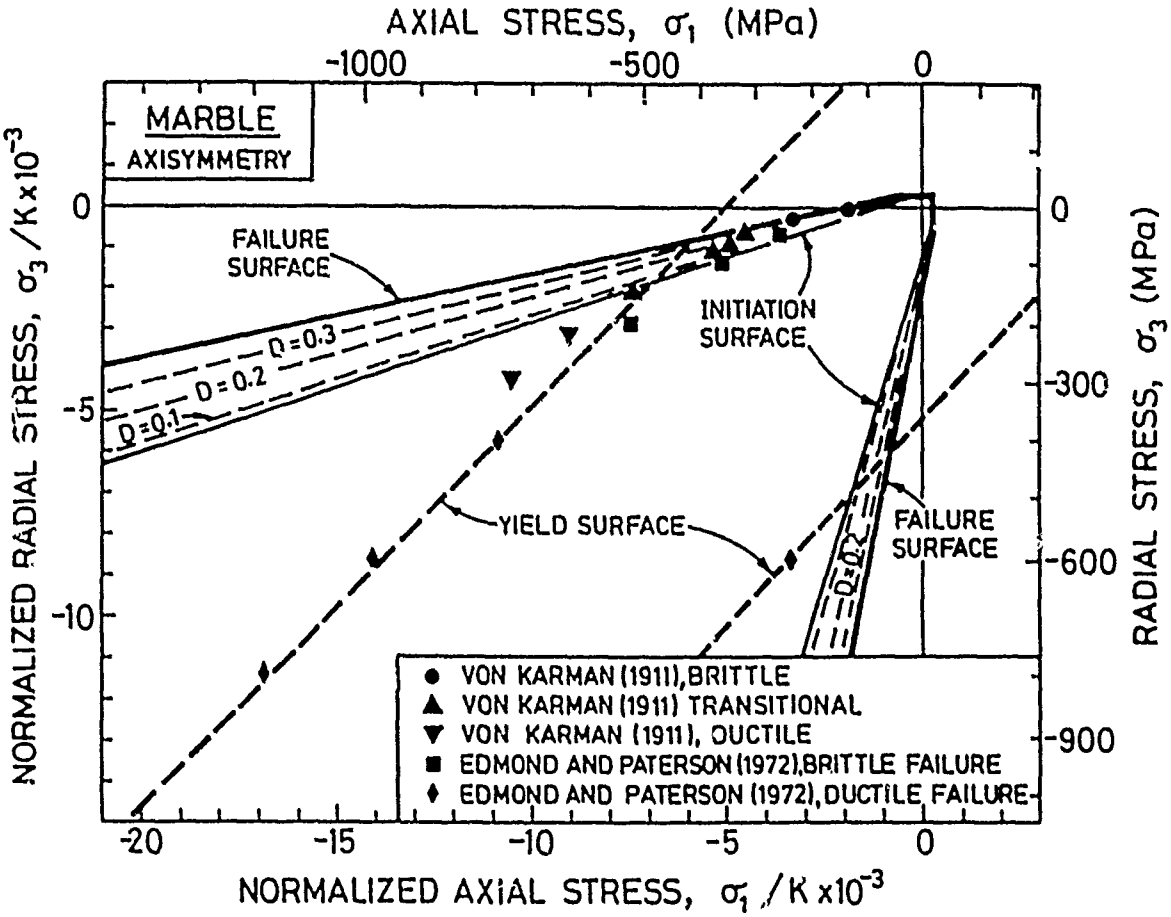

Figure 22. Comparison between experimental and theoretical failure surfaces for marble extended to the highest measured confining stress. The heavy solid line is the theoretical failure surface. The light solid line is the surface for the initiation of microfracturing while the light broken lines are surfaces of constant damage. The heavy broken line is the yield surface (eqn. 30).

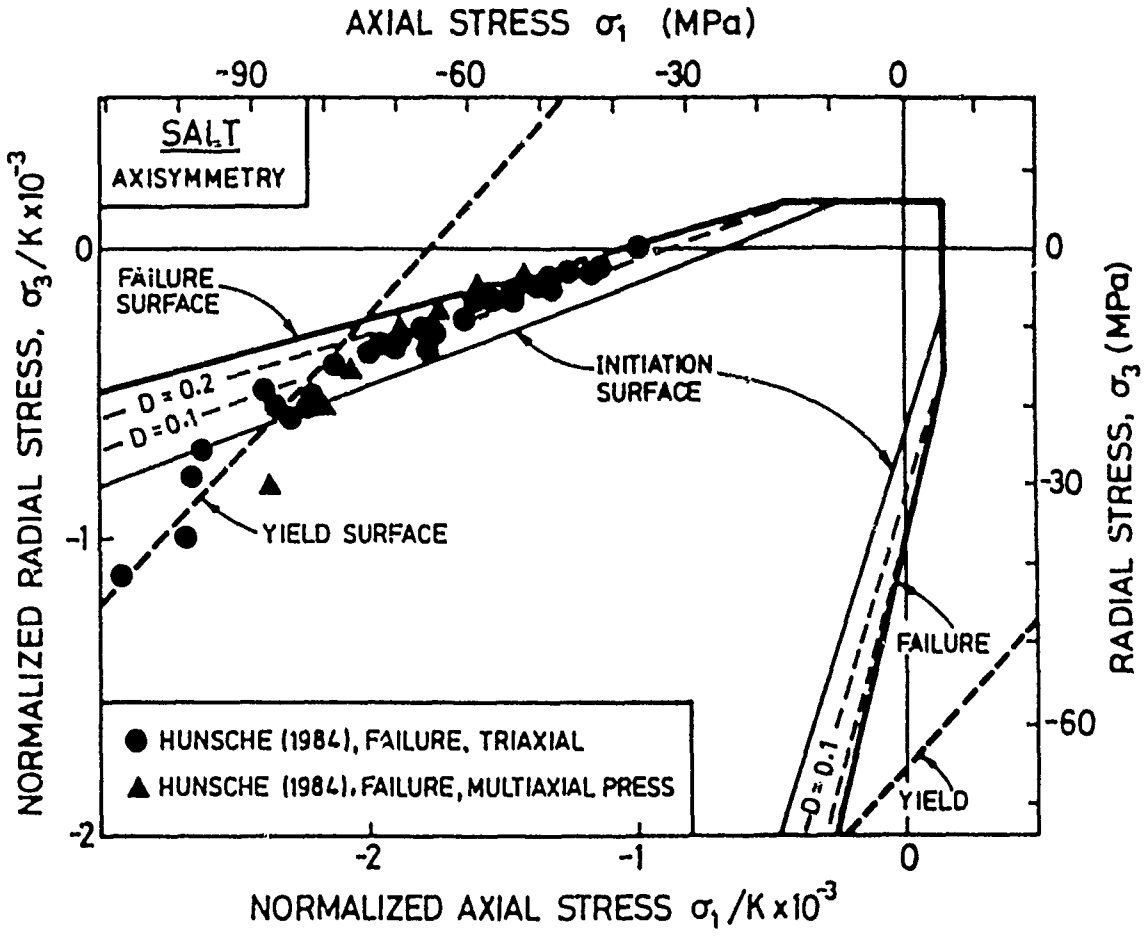

Figure 23. Comparison between experimental and theoretical failure surfaces for rock salt at low and intermediate confining stress. The heavy solid line is the theoretical failure surface. The light solid line is the surface for the initiation of microfracturing while the light broken lines are surfaces of constant damage. The heavy broken line is the yield surface (eqn. 30).

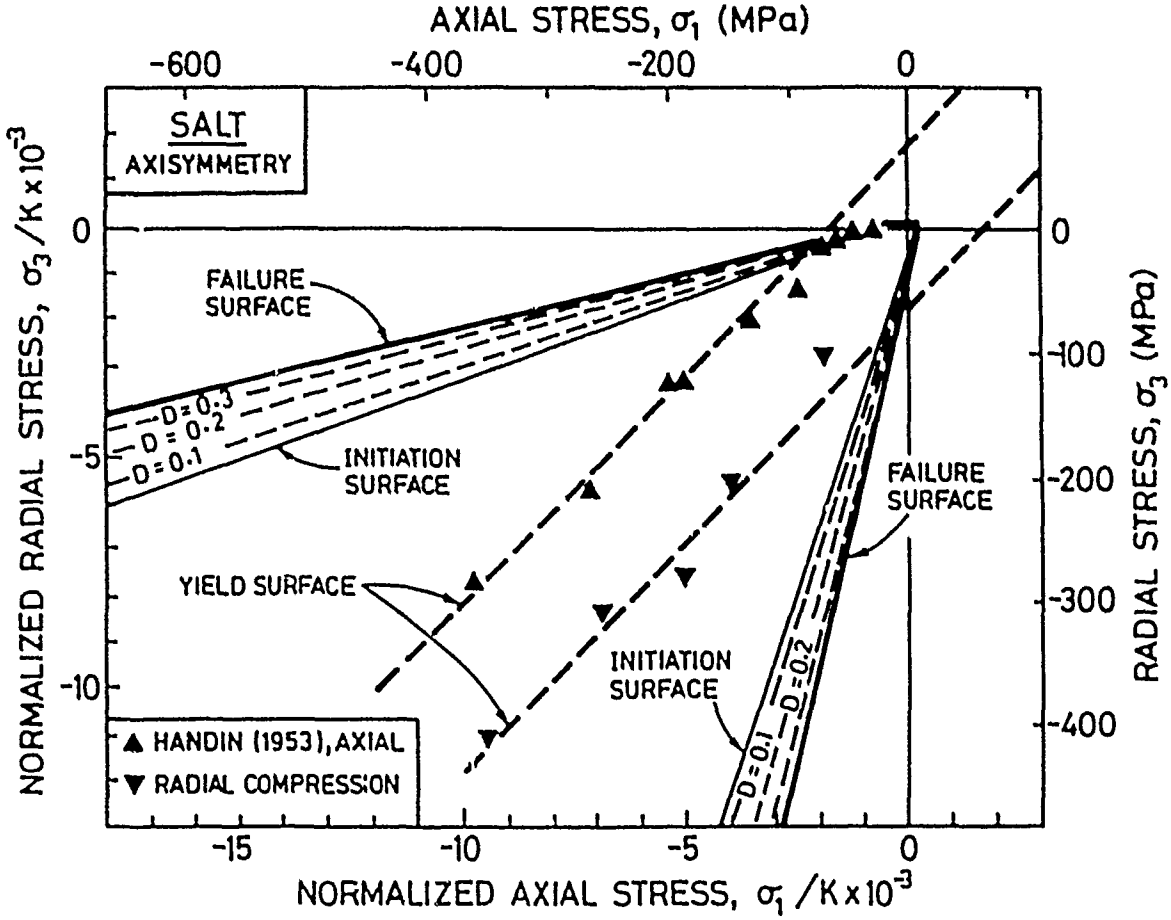

Figure 24. Comparison between experimental and theoretical failure surfaces for rock salt extended to the largest confining stress. The heavy solid line is the theoretical failure surface. The light solid line is the surface for the initiation of microfracturing while the light broken lines are surfaces of constant damage. The heavy broken line is the yield surface (eqn. 30).

CONTRACTORS (United States)

Professor Keiiti Aki
Center for Earth Sciences
University of Southern California
University Park
Los Angeles, CA 90089-0741

Professor Thomas Ahrens
Seismological Lab, 252-21
Div. of Geological and Planetary
Sciences
California Institute of Technology
Pasadena, CA 91125

Professor Charles B. Archambeau
Cooperative Institute for Resch
in Environmental Sciences
University of Colorado
Boulder, CO 80309

Dr. Thomas C. Bache Jr.
Science Applications Int'l Corp.
10210 Campus Point Drive
San Diego, CA 92121 (2 copies)

Dr. Muawia Barazangi
Institute for the Study of
of the Continent
Cornell University
Ithaca, NY 14853

Dr. Douglas R. Baumgardt
Signal Analysis & Systems Div.
ENSCO, Inc.
5400 Port Royal Road
Springfield, VA 22151-2388

Dr. Jonathan Berger
Institute of Geophysics and
Planetary Physics
Scripps Institution of Oceanography
A-025
University of California, San Diego
La Jolla, CA 92093

Dr. S. Bratt
Science Applications Int'l Corp.
10210 Campus Point Drive
San Diego, CA 92121

Dr. Lawrence J. Burdick
Woodward-Clyde Consultants
P.O. Box 93245
Pasadena, CA 91109-3245 (2 copies)

Professor Robert W. Clayton
Seismological Laboratory/Div. of
Geological & Planetary Sciences
California Institute of Technology
Pasadena, CA 91125

Dr Karl Coyner
New England Research, Inc.
76 Olcott Drive
White River Junction, VT 05001

Dr. Vernon F. Cormier
Department of Geology & Geophysics
U-45, Room 207
The University of Conneticut
Storrs, Connecticut 06268

Dr. Steven Day
Dept. of Geological Sciences
San Diego State U.
San Diego, CA 92182

Dr. Zoltan A. Der
ENSCO, Inc.
5400 Port Royal Road
Springfield, VA 22151-2388

Professor John Ferguson
Center for Lithospheric Studies
The University of Texas at Dallas
P.O. Box 830688
Richardson, TX 75083-0688

Professor Stanley Flatte'
Applied Sciences Building
University of California,
Santa Cruz, CA 95064

Dr. Alexander Florence
SRI International
333 Ravenswood Avenue
Menlo Park, CA 94025-3493

Professor Steven Grand
University of Texas at Austin
Dept of Geological Sciences
Austin, TX 78713-7909

Dr. Henry L. Gray
Associate Dean of Dedman College
Department of Statistical Sciences
Southern Methodist University
Dallas, TX 75275

Professor Roy Greenfield
Geosciences Department
403 Deike Building
The Pennsylvania State University
University Park, PA 16802

Professor David G. Harkrider
Seismological Laboratory
Div of Geological & Planetary Sciences
California Institute of Technology
Pasadena, CA 91125

Professor Donald V. Helmberger
Seismological Laboratory
Div of Geological & Planetary Sciences
California Institute of Technology
Pasadena, CA 91125

Professor Eugene Herrin
Institute for the Study of Earth
and Man/Geophysical Laboratory
Southern Methodist University
Dallas, TX 75275

Professor Robert B. Herrmann
Department of Earth & Atmospheric
Sciences
Saint Louis University
Saint Louis, MO 63156

Professor Bryan Isacks
Cornell University
Dept of Geological Sciences
SNEE Hall
Ithaca, NY 14850

Professor Lane R. Johnson
Seismographic Station
University of California
Berkeley, CA 94720

Professor Thomas H. Jordan
Department of Earth, Atmospheric
and Planetary Sciences
Mass Institute of Technology
Cambridge, MA 02139

Dr. Alan Kafka
Department of Geology &
Geophysics
Boston College
Chestnut Hill, MA 02167

Professor Leon Knopoff
University of California
Institute of Geophysics
& Planetary Physics
Los Angeles, CA 90024

Professor Charles A. Langston
Geosciences Department
403 Deike Building
The Pennsylvania State University
University Park, PA 16802

Professor Thorne Lay
Department of Geological Sciences
1006 C.C. Little Building
University of Michigan
Ann Arbor, MI 48109-1063

Dr. Randolph Martin III
New England Research, Inc.
76 Olcott Drive
White River Junction, VT 05001

Dr. Gary McCartor
Mission Research Corp.
735 State Street
P.O. Drawer 719
Santa Barbara, CA 93102 (2 copies)

Professor Thomas V. McEvilly
Seismographic Station
University of California
Berkeley, CA 94720

Dr. Keith L. McLaughlin
S-CUBED,
A Division of Maxwell Laboratory
P.O. Box 1620
La Jolla, CA 92038-1620

Professor William Menke
Lamont-Doherty Geological Observatory
of Columbia University
Palisades, NY 10964

Professor Brian J. Mitchell
Department of Earth & Atmospheric
Sciences
Saint Louis University
Saint Louis, MO 63156

Mr. Jack Murphy
S-CUBED
A Division of Maxwell Laboratory
11800 Sunrise Valley Drive
Suite 1212
Reston, VA 22091 (2 copies)

Professor J. A. Orcutt
IGPP, A-205
Scripps Institute of Oceanography
Univ. of California, San Diego
La Jolla, CA 92093

Professor Keith Priestley
University of Nevada
Mackay School of Mines
Reno, NV 89557

Professor Paul G. Richards
Lamont-Doherty Geological
Observatory of Columbia Univ.
Palisades, NY 10964

Wilmer Rivers
Teledyne Geotech
314 Montgomery Street
Alexandria, VA 22314

Dr. Alan S. Ryall, Jr.
Center of Seismic Studies
1300 North 17th Street
Suite 1450
Arlington, VA 22209-2308 (4 copies)

Professor Charles G. Sammis
Center for Earth Sciences
University of Southern California
University Park
Los Angeles, CA 90089-0741

Professor Christopher H. Scholz
Geological Sciences
Lamont-Doherty Geological Observatory
Palisades, NY 10964

Dr. Jeffrey L. Stevens
S-CUBED,
A Division of Maxwell Laboratory
P.O. Box 1620
La Jolla, CA 92038-1620

Professor Brian Stump
Institute for the Study of Earth & Man
Geophysical Laboratory
Southern Methodist University
Dallas, TX 75275

Professor Ta-liang Teng
Center for Earth Sciences
University of Southern California
University Park
Los Angeles, CA 90089-0741

Dr. Clifford Thurber
State University of New York at
Stony Brooks
Dept of Earth and Space Sciences
Stony Brook, NY 11794-2100

Professor M. Nafi Toksoz
Earth Resources Lab
Dept of Earth, Atmospheric and
Planetary Sciences
Massachusetts Institute of Technology
42 Carleton Street
Cambridge, MA 02142

Professor Terry C. Wallace
Department of Geosciences
Building #77
University of Arizona
Tucson, AZ 85721

Weidlinger Associates
ATTN: Dr. Gregory Wojcik
4410 El Camino Real, Suite 110
Los Altos, CA 94022

Professor Francis T. Wu
Department of Geological Sciences
State University of New York
at Binghamton
Vestal, NY 13901

OTHERS (United States)

Dr. Monem Abdel-Gawad
Rockwell International Science Center
1049 Camino Dos Rios
Thousand Oaks, CA 91360

Professor Shelton S. Alexander
Geosciences Department
403 Deike Building
The Pennsylvania State University
University Park, PA 16802

Dr. Ralph Archuleta
Department of Geological Sciences
Univ. of California at Santa Barbara
Santa Barbara, CA

J. Barker
Department of Geological Sciences
State University of New York at Binghamton
Vestal, NY 13901

Mr. William J. Best
907 Westwood Drive
Vienna, VA 22180

Dr. N. Biswas
Geophysical Institute
University of Alaska
Fairbanks, AK 99701

Dr. G. A. Bollinger
Department of Geological Sciences
Virginia Polytechnical Institute
21044 Derring Hall
Blacksburg, VA 24061

Mr. Roy Burger
1221 Serry Rd.
Schenectady, NY 12309

Dr. Robert Burridge
Schlumberger-Doll Resch Ctr.
Old Quarry Road
Ridgefield, CT 06877

Science Horizons, Inc.
ATTN: Dr. Theodore Cherry
710 Encinitas Blvd., Suite 101
Encinitas, CA 92024 (2 copies)

Professor Jon F. Claerbout
Professor Amos Nur
Dept. of Geophysics
Stanford University
Stanford, CA 94305 (2 copies)

Dr. Anton W. Dainty
Earth Resources Lab
Massachusetts Institute of Technology
42 Carleton Street
Cambridge, MA 02142

Professor Adam Dziewonski
Hoffman Laboratory
Harvard University
20 Oxford St.
Cambridge, MA 02138

Professor John Ebel
Dept of Geology and Geophysics
Boston College
Chestnut Hill, MA 02167

Dr. Donald Forsyth
Dept of Geological Sciences
Brown University
Providence, RI 02912

Dr. Anthony Gangi
Texas A&M University
Department of Geophysics
College Station, TX 77843

Dr. Freeman Gilbert
Institute of Geophysics & Planetary Physics
University of California, San Diego
P.O. Box 109
La Jolla, CA 92037

Mr. Edward Giller
Pacific Sierra Research Corp.
1401 Wilson Boulevard
Arlington, VA 22209

Dr. Jeffrey W. Given
Sierra Geophysics
11255 Kirkland Way
Kirkland, WA 98033

Rong Song Jih
Teledyne Geotech
314 Montgomery Street
Alexandria, Virginia 22314

Professor F.K. Lamb
University of Illinois at
Urbana-Champaign
Department of Physics
1110 West Green Street
Urbana, IL 61801

Dr. Arthur Lerner-Lam
Lamont-Doherty Geological Observatory
of Columbia University
Palisades, NY 10964

Dr. L. Timothy Long
School of Geophysical Sciences
Georgia Institute of Technology
Atlanta, GA 30332

Dr. Peter Malin
University of California at
Santa Barbara
Institute for Central Studies
Santa Barbara, CA 93106

Dr. George R. Mellman
Sierra Geophysics
11255 Kirkland Way
Kirkland, WA 98033

Dr. Bernard Minster
IGPP, A-205
Scripps Institute of Oceanography
Univ. of California, San Diego
La Jolla, CA 92093

Professor John Nabelek
College of Oceanography
Oregon State University
Corvallis, OR 97331

Dr. Geza Nagy
U. California, San Diego
Dept of Ames, M.S. B-010
La Jolla, CA 92093

Dr. Jack Oliver
Department of Geology
Cornell University
Ithaca, NY 14850

Dr. Robert Phinney/Dr. F. A. Dahlen
Dept of Geological
Geological Science University
Princeton University
Princeton, NJ 08540

RADIX System, Inc.
Attn: Dr. Jay Pulli
2 Taft Court, Suite 203
Rockville, Maryland 20850

Dr. Norton Rimer
S-CUBED
A Division of Maxwell Laboratory
P.O. 1620
La Jolla, CA 92038-1620

Professor Larry J. Ruff
Department of Geological Sciences
1006 C.C. Little Building
University of Michigan
Ann Arbor, MI 48109-1063

Dr. Richard Sailor
TASC Inc.
55 Walkers Brook Drive
Reading, MA 01867

Thomas J. Sereno, Jr.
Science Application Int'l Corp.
10210 Campus Point Drive
San Diego, CA 92121

Dr. David G. Simpson
Lamont-Doherty Geological Observ.
of Columbia University
Palisades, NY 10964

Dr. Bob Smith
Department of Geophysics
University of Utah
1400 East 2nd South
Salt Lake City, UT 84112

Dr. S. W. Smith
Geophysics Program
University of Washington
Seattle, WA 98195

Dr. Stewart Smith
IRIS Inc.
1616 N. Fort Myer Drive
Suite 1440
Arlington, VA 22209

Rondout Associates
ATTN: Dr. George Sutton,
Dr. Jerry Carter, Dr. Paul Pomeroy
P.O. Box 224
Stone Ridge, NY 12484 (4 copies)

Dr. L. Sykes
Lamont Doherty Geological Observ.
Columbia University
Palisades, NY 10964

Dr. Pradeep Talwani
Department of Geological Sciences
University of South Carolina
Columbia, SC 29208

Dr. R. B. Tittmann
Rockwell International Science Center
1049 Camino Dos Rios
P.O. Box 1085
Thousand Oaks, CA 91360

Professor John H. Woodhouse
Hoffman Laboratory
Harvard University
20 Oxford St.
Cambridge, MA 02138

Dr. Gregory B. Young
ENSCO, Inc.
5400 Port Royal Road
Springfield, VA 22151-2388

Dr. Gregory van der Vink
IRIS
Suite 1440
1616 North Fort Myer Drive
Arlington, VA 22209

FOREIGN (OTHERS)

Dr. Peter Basham
Earth Physics Branch
Geological Survey of Canada
1 Observatory Crescent
Ottawa, Ontario
CANADA K1A 0Y3

Professor Ari Ben-Menahem
Dept of Applied Mathematics
Weizman Institute of Science
Rehovot
ISRAEL 951729

Dr. Eduard Berg
Institute of Geophysics
University of Hawaii
Honolulu, HI 96822

Dr. Michel Bouchon - Universite
Scientifique et Medicale de Grenob
Lab de Geophysique - Interne et
Tectonophysique - I.R.I.G.M-B.P.
38402 St. Martin D'Heres
Cedex FRANCE

Dr. Hilmar Bungum/NTNF/NORSAR
P.O. Box 51
Norwegian Council of Science,
Industry and Research, NORSAR
N-2007 Kjeller, NORWAY

Dr. Michel Campillo
I.R.I.G.M.-B.P. 68
38402 St. Martin D'Heres
Cedex, FRANCE

Dr. Kin-Yip Chun
Geophysics Division
Physics Department
University of Toronto
Ontario, CANADA M5S 1A7

Dr. Alan Douglas
Ministry of Defense
Blacknest, Brimpton,
Reading RG7-4RS
UNITED KINGDOM

Dr. Manfred Henger
Fed. Inst. For Geosciences & Nat'l Res.
Postfach 510153
D-3000 Hannover 51
FEDERAL REPUBLIC OF GERMANY

Ms. Eva Johannisson
Senior Research Officer
National Defense Research Inst.
P.O. Box 27322
S-102 54 Stockholm
SWEDEN

Tormod Kvaerna
NTNF/NORSAR
P.O. Box 51
N-2007 Kjeller, NORWAY

Mr. Peter Marshall, Procurement
Executive, Ministry of Defense
Blacknest, Brimpton,
Reading FG7-4RS
UNITED KINGDOM (3 copies)

Dr. Robert North
Geophysics Division
Geological Survey of Canada
1 Observatory crescent
Ottawa, Ontario
CANADA, K1A 0Y3

Dr. Frode Ringdal
NTNF/NORSAR
P.O. Box 51
N-2007 Kjeller, NORWAY

Dr. Jorg Schlittenhardt
Federal Inst. for Geosciences & Nat'l Res.
Postfach 510153
D-3000 Hannover 51
FEDERAL REPUBLIC OF GERMANY

University of Hawaii
Institute of Geophysics
ATTN: Dr. Daniel Walker
Honolulu, HI 96822

FOREIGN CONTRACTORS

Dr. Ramon Cabre, S.J.
Observatorio San Calixto
Casilla 5939
La Paz Bolivia

Professor Peter Harjes
Institute for Geophysik
Rhur University/Bochum
P.O. Box 102148, 4630 Bochum 1
FEDERAL REPUBLIC OF GERMANY

Dr. E. Husebye
NTNF/NORSAR
P.O. Box 51
N-2007 Kjeller, NORWAY

Professor Brian L.N. Kennett
Research School of Earth Sciences
Institute of Advanced Studies
G.P.O. Box 4
Canberra 2601
AUSTRALIA

Dr. B. Massinon
Societe Radiomana
27, Rue Claude Bernard
7,005, Paris, FRANCE (2 copies)

Dr. Pierre Mechler
Societe Radiomana
27, Rue Claude Bernard
75005, Paris, FRANCE

Dr. Svein Mykkeltveit
NTNF/NORSAR
P.O. Box 51
N-2007 Kjeller, NORWAY (3 copies)

GOVERNMENT

Dr. Ralph Alewine III
DARPA/NMRO
1400 Wilson Boulevard
Arlington, VA 22209-2308

Dr. Robert Blandford
DARPA/NMRO
1400 Wilson Boulevard
Arlington, VA 22209-2308

Sandia National Laboratory
ATTN: Dr. H. B. Durham
Albuquerque, NM 87185

Dr. Jack Evernden
USGS-Earthquake Studies
345 Middlefield Road
Menlo Park, CA 94025

U.S. Geological Survey
ATTN: Dr. T. Hanks
Nat'l Earthquake Resch Center
345 Middlefield Road
Menlo Park, CA 94025

Dr. James Hannon
Lawrence Livermore Nat'l Lab.
P.O. Box 808
Livermore, CA 94550

Paul Johnson
ESS-4, Mail Stop J979
Los Alamos National Laboratory
Los Alamos, NM 87545

Ms. Ann Kerr
DARPA/NMRO
1400 Wilson Boulevard
Arlington, VA 22209-2308

Dr. Max Koontz
US Dept of Energy/DP 5
Forrestal Building
1000 Independence Ave.
Washington, D.C. 20585

Dr. W. H. K. Lee
USGS
Office of Earthquakes, Volcanoes,
& Engineering
Branch of Seismology
345 Middlefield Rd
Menlo Park, CA 94025

Dr. William Leith
U.S. Geological Survey
Mail Stop 928
Reston, VA 22092

Dr. Richard Lewis
Dir. Earthquake Engineering and
Geophysics
U.S. Army Corps of Engineers
Box 631
Vicksburg, MS 39180

Dr. Robert Massol
Box 25046, Mail Stop 967
Denver Federal Center
Denver, Colorado 80225

Richard Morrow
ACDA/VI
Room 5741
320 21st Street N.W.
Washington, D.C. 20451

Dr. Keith K. Nakanishi
Lawrence Livermore National Laboratory
P.O. Box 808, L-205
Livermore, CA 94550 (2 copies)

Dr. Carl Newton
Los Alamos National Lab.
P.O. Box 1663
Mail Stop C335, Group ESS-3
Los Alamos, NM 87545

Dr. Kenneth H. Olsen
Los Alamos Scientific Lab.
P.O. Box 1663
Mail Stop C335, Group ESS-3
Los Alamos, NM 87545

Howard J. Patton
Lawrence Livermore National
Laboratory
P.O. Box 808, L-205
Livermore, CA 94550

Mr. Chris Paine
Office of Senator Kennedy
SR 315
United States Senate
Washington, D.C. 20510

AFOSR/NP
ATTN: Colonel Jerry J. Perrizo
Bldg 410
Bolling AFB, Wash D.C. 20332-6448

HQ AFTAC/TT
Attn: Dr. Frank F. Pilotte
Patrick AFB, Florida 32925-6001

Mr. Jack Rachlin
USGS - Geology, Rm 3 C136
Mail Stop 928 National Center
Reston, VA 22092

Robert Reinke
AFWL/NTESG
Kirtland AFB, NM 87117-6008

Dr. Byron Ristvet
HQ DNA, Nevada Operations Office
Attn: NVCG
P.O. Box 98539
Las Vegas, NV 89193

HQ AFTAC/TGR
Attn: Dr. George H. Rothe
Patrick AFB, Florida 32925-6001

Donald L. Springer
Lawrence Livermore National Laboratory
P.O. Box 808, L-205
Livermore, CA 94550

Dr. Lawrence Turnbull
OSWR/NED
Central Intelligence Agency
CIA, Room 5G48
Washington, D.C. 20505

Dr. Thomas Weaver
Los Alamos National Laboratory
P.O. Box 1663
MS C 335
Los Alamos, NM 87545

GL/SULL
Research Library
Hanscom AFB, MA 01731-5000 (2 copies)

Secretary of the Air Force (SAFRD)
Washington, DC 20330
Office of the Secretary Defense
DDR & E
Washington, DC 20330

HQ DNA
ATTN: Technical Library
Washington, DC 20305

DARPA/RMO/RETRIEVAL
1400 Wilson Blvd.
Arlington, VA 22209

DARPA/RMO/Security Office
1400 Wilson Blvd.
Arlington, VA 22209

GL/XO
Hanscom AFB, MA 01731-5000

GL/LW
Hanscom AFB, MA 01731-5000

DARPA/PM
1400 Wilson Boulevard
Arlington, VA 22209

Defense Technical
Information Center
Cameron Station
Alexandria, VA 22314
(5 copies)

Defense Intelligence Agency
Directorate for Scientific &
Technical Intelligence
Washington, D.C. 20301

Defense Nuclear Agency/SPSS
ATTN: Dr. Michael Shore
6801 Telegraph Road
Alexandria, VA 22310

AFTAC/CA (STINFO)
Patrick AFB, FL 32925-6001

TACTEC
Battelle Memorial Institute
505 King Avenue
Columbus, OH 43201 (Final report only)

Mr. Alfred Lieberman
ACDA/VI-OA'State Department Building
Room 5726
320 - 21St Street, NW
Washington, D.C. 20451